Title

Lab-Under-The-Skin: A Microneedle Platform for Electrochemical Wearable Sensing

Author

Tehrani, Farshad Eden

Publication Date

2021

Peer reviewed|Thesis/dissertation

UNIVERSITY OF CALIFORNIA SAN DIEGO

Lab-Under-The-Skin:
A Microneedle Platform for Electrochemical Wearable Sensing

A dissertation submitted in partial satisfaction of the requirements for the degree

Doctor of Philosophy

in

Nanoengineering

by

Farshad Tehrani

Committee in charge:

Professor Joseph Wang, Chair
Professor Sheng Xu, Co-Chair
Professor Jesse Jokerst
Professor Patrick Mercier
Professor Susan Tapert

2021

The Dissertation of Farshad Tehrani is approved, and it is acceptable in quality and form for publication on microfilm and electronically.

University of California San Diego

2021

DEDICATION

To my lovely family.

TABLE OF CONTENTS

LIST OF FIGURES

ACKNOWLEDGMENTS

I would like to deeply thank my advisor professor Joseph Wang for his exceptional support, guidance, and trust throughout the course of my PhD. Prof. Wang's dedication to my professional development consistently shifted my perception of what's possible in the realm of science and engineering and opened unprecedented accomplishments that may not have been possible otherwise. Also, I'd like to thank my committee members, Prof. Patrick Mercier, Prof. Susan Tapert, Prof. Sheng Xu, and Prof. Jesse Jokerst for their guidance throughout this journey. Particularly, I appreciate Prof. Patrick Mercier and his research team, especially Brian Wuerstle for their undivided support in developing electronics systems required for the success of our microneedle-based wearable sensors platform. Additionally, I've been privileged to receive exceptional support, knowledge, and dedicated teamwork from Dr. Hazhir Teymourian, which made the success of our joint projects a joyful journey. Finally, I'd like to express my deepest gratitude to my loving family. My success throughout the PhD program truly stems from their love, care, and support that I've been privileged to receive.

I'd like to acknowledge the direct/indirect teamwork, support, and contributors of the coauthors of my thesis; Hazhir Teymourian, Jonathan Kavner, Brian Wuerstle, Allison Furmidge, Reza Aghavali, Abbas Barfidokht, Nickey Huang, Fangyu Zhang, Lu Yin, Rupesh Mishra, Yao Wu, Kuldeep Mahato, Zhengxing Li, Zhanhong Li, Paul Warren, Chochanon Moonla, John Mack, Netzahualcóyotl Arroyo-Currás, Patrick P. Mercier, K. Yugender Goud, Mona A. Mohamed, Ravi Patel, Christopher Brown, and Zina Patel.

In the thesis, **Chapter 1** is based, in part, on the material as it appears in Advanced Healthcare Materials, 2021, by Hazhir Teymourian, Farshad Tehrani, Kuldeep Mahato, in

Advanced Healthcare Materials. The dissertation author was the primary co-investigator and co-author of this paper.

Chapter 2, in part, and has been submitted for publication of the material, as it may appears in Nature, 2021, by Farshad Tehrani, Hazhir Teymourian, Brian Wuerstle, Jonathan Kavner, Ravi Patel, Allison Furmidge, Reza Aghavali, Christopher Brown, Fangyu Zhang, Kuldeep Mahato, Zhengxing Li, Abbas Barfidokht, Lu Yin, Paul Warren, Nickey Huang, Zina Patel, Patrick P. Mercier, Joseph Wang. The dissertation author was the primary investigator and author of this paper.

Chapter 3 is based, in part, on the material as it may appear in Analytical chemistry, 2022, by Abbas Barfidokht, Farshad Tehrani, and Joseph Wang. The dissertation author was the primary co-investigator and co-author of this paper.

Chapter 4 is based, in part, on the material as it appears in Journal of the American Chemical Society, 2019, by Rupesh K. Mishra, K. Yugender Goud, Zhanhong Li, Chochanon Moonla, Mona A. Mohamed, Farshad Tehrani, Hazhir Teymourian, and Joseph Wang. The dissertation author was the co-investigator and coauthor of this paper.

Chapter 5 is based, in part, on the material as it may appear in Proceedings of the National Academy of Sciences of the United States of America, 2022, by Yao Wu, Farshad Tehrani, Hazhir Teymourian, John Mack, Jonathan Kavner, Nickey Huang, Allison Furmidge, Joseph Wang, and Netzahualcóyotl Arroyo-Currás. The dissertation author was the primary co-investigator and coauthor of this paper.

VITA

2010 B.S. in Materials Engineering, Azad University, Najaf Abad, Iran

2015 M.S. in Materials Engineering, California State University of Northridge, USA

2021 Ph.D. in Nanoengineering, University of California San Diego, USA

PUBLICATIONS

- **Farshad Tehrani,** Hazhir Teymourian, Brian Wuerstle, Jonathan Kavner, Ravi Patel, Allison Furmidge, Reza Aghavali, Christopher Brown, Fangyu Zhang, Kuldeep Mahato, Zhengxing Li, Abbas Barfidokht, Lu Yin, Paul Warren, Nickey Huang, Zina Patel, Patrick P. Mercier, Joseph Wang, **"**A Non-Intrusive Lab-Under-the-Skin: Continuous Monitoring of Multiple Interstitial Fluid Biomarkers via a Fully Integrated Wearable Microneedle Platform" Nature, in review, 2021

- Eleonora M. Aiello, Jordan E. Pinsker, Eva Vargas, Hazhir Teymourian, **Farshad Tehrani,** Mei Mei Church, Lori M. Laffel, Francis J. Doyle III, Mary-Elizabeth Patti, Joseph Wang, Eyal Dassau, 'Clinical Evaluation of a Novel Insulin Immunosensor', Journal of Diabetes Science and Technology, in review, 2021

- Eva Vargas, Eleonora M. Aiello, Jordan E. Pinsker, Hazhir Teymourian, **Farshad Tehrani**, Mei Mei Church, Lori M. Laffel, MPH4; Francis J. Doyle, Mary-Elizabeth Patti, Eyal Dassau, Joseph Wang, 'Clinical Evaluation of a Novel Insulin Immunosensor', Journal of Diabetes Science and Technology, in review. 2021

- Hazhir Teymourian, **Farshad Tehrani,** Kuldeep Mahato, Tatiana Podhajny, Jong-Min Moon, Yugender Goud Kotagiri, Juliane R. Sempionatto, Katherine Longardner, Irene Litvan, and Joseph Wang, "Closing the loop for Parkinson disease patients: where are we?" in review 'Nature Reviews Neurology, In Review, 2021

- Yao Wu, **Farshad Tehrani**, Hazhir Teymourian, John Mack, Jonathan Kavner, Nickey Huang, Allison Furmidge, Joseph Wang, and Netzahualcóyotl Arroyo-Currás, "Wearable Microneedle Aptamer-Based Sensors for Continuous, Real-Time Molecular Monitoring in the Body", in preparation for submission to Proceedings of the National Academy of Sciences of the United States of America, 2022

- Fangyu Zhang, Zhengxing Li, Lu Yin, Qiangzhe Zhang, Nelly Askarinam, Rodolfo Mundaca-Uribe, **Farshad Tehrani,** Emil Karshalev, Weiwei Gao, Liangfang Zhang*, and Joseph Wang, "ACE2 Receptor-Modified Algae-Based Microrobot for Removal of SARS-CoV-2 in Wastewater", J. Am. Chem. Soc. 2021, 143, 31, 12194–12201

- Kelilah L. Wolkowicz, Eleonora M. Aiello, Eva Vargas, Hazhir Teymourian, **Farshad Tehrani**, Joseph Wang, Jordan E. Pinsker, Francis J. Doyle III, Mary-Elizabeth Patti, Lori M. Laffel, Eyal Dassau, "A review of biomarkers in the context of type 1 diabetes: Biological sensing for enhanced glucose control" Bioengineering and Translational Medicine, 2021

- Hazhir Teymourian, **Farshad Tehrani,** Kuldeep Mahato, "Lab under the Skin: Microneedle Based Wearable Devices", Advanced Healthcare Mat. 2021

- Lu Yin, Kyeong Nam Kim, Jian Lv**, Farshad Tehrani,** Muyang Lin, Zuzeng Lin, Jong-Min Moon, Jessica Ma, Jialu Yu, Sheng Xu & Joseph Wang, "A self-sustainable wearable multi-modular E-textile bioenergy microgrid system, Nature Communication. 2021

- Kelilah L. Wolkowicz, Eva Vargas, Hazhir Teymourian, **Farshad Tehrani**, Jordan E. Pinsker, Mei Mei Church, Molly Piper, Francis J. Doyle I, Mary-Elizabeth Patti, Lori M. Laffel, Joseph Wang And Eyal Dassau, "Towards Point-of-Care Devices: First Evaluation of an Insulin Immunosensor for Type 1 Diabetes" Diabetes, 2020

- Rupesh K. Mishra, K. Yugender Goud, Zhanhong Li, Chochanon Moonla, Mona A. Mohamed, **Farshad Tehrani,** Hazhir Teymourian, and Joseph Wang, "Continuous opioid monitoring along with nerve agents on a wearable microneedle sensor array" Journal of the American Chemical Society, 2020

- Fernando Soto, Daniel Kupor, Miguel Angel Lopez-Ramirez. Fanan Wei, Emil Karshalev, Songsong Tang, **Farshad Tehrani,** Joseph Wang, "Onion-like Multifunctional Microtrap Vehicles for Attraction–Trapping–Destruction of Biological Threats" Angewandte Chemie International Edition, 2020

- Eva Vargas, Eloy Povedanoa, Sadagopan Krishnana, Hazhir Teymourian, **Farshad Tehrani,** Susana Campuzano, Eyal Dassau, Joseph Wang, "Simultaneous cortisol/insulin microchip detection using dual enzyme tagging" Biosensors & bioelectronics, 2020

- Hazhir Teymourian, Chochanon Moonla, **Farshad Tehrani**, Eva Vargas, Reza Aghavali, Abbas Barfidokht, Tanin Tangkuaram, Patrick P. Mercier, Eyal Dassau, and Joseph Wang, "Microneedle-based detection of ketone bodies along with glucose and lactate: Toward real-time continuous interstitial fluid monitoring of diabetic ketosis and ketoacidosis" Analytical chemistry, 2019

- Laís C. Brazaca, José R. Moreto, Aída Martín, **Farshad Tehrani**, Joseph Wang, and Valtencir Zucolotto, "Colorimetric paper-based immunosensor for simultaneous determination of fetuin B and clusterin toward early Alzheimer's diagnosis" ACS Nano 2019

- Eva Vargas, Hazhir Teymourian, **Farshad Tehrani**, Ece Eksin, Esther Sánchez-Tirado, Paul Warren, Arzum Erdem, Eyal Dassau, Prof. Joseph Wang, "Enzymatic/Immunoassay Dual-Biomarker Sensing Chip: Towards Decentralized Insulin/Glucose Detection" Angewandte,

2019

- Jian Lv, Itthipon Jeerapan, **Farshad Tehrani,** Lu Yin, Cristian Abraham Silva-Lopez, Ji-Hyun Jang, Davina Joshuia, Rushabh Shah, Yuyan Liang, Lingye Xie, Fernando Soto, Chuanrui Chen, Emil Karshalev, Chuncai Kong, Zhimao Yang, Joseph Wang, "Sweat-based wearable energy harvesting-storage hybrid textile devices" Energy & Environmental Sciences, 2019

- **Farshad Tehrani,** Mara Beltrán-Gastélum, Karan Sheth, Aleksandar Karajic, Lu Yin, Rajan Kumar, Fernando Soto, Jayoung Kim, Joshua Wang, Shemaiah Barton, Michelle Mueller, Joseph Wang, "Laser-Induced Graphene Composites for Printed, Stretchable, and Wearable Electronics" Advanced Healthcare Materials, 2019

- GeeteRupeshsh Kumar Mishra, Abbas Barfidokht, **Farshad Tehrani**, Rupesh Kumar Mishra, "Food safety analysis using electrochemical biosensors" Food 2018

- **Farshad Tehrani**, Behzad Bavarian, "Facile and scalable disposable sensor based on laser engraved graphene for electrochemical detection of glucose*"* Nature, SR, 2016

- **Farshad Tehrani,** Lisa Reiner, Behzad Bavarian, "*Rapid prototyping of a high sensitivity graphene-based glucose sensor"* PLOS ONE, 2015

FIELDS OF STUDY

Major Field: Biomedical Electronic Devices

Studies in Nanoengineering

Professor Joseph Wang

ABSTRACT OF THE DISSERTATION

Lab-Under-The-Skin: A Microneedle-Based Wearable Sensor

by

Farshad Tehrani

Doctor of Philosophy in Nanoengineering

University of California San Diego, 2021

Professor Joseph Wang, Chair
Professor Sheng Xu, Co-Chair

Lab-Under-The-Skin based on a microneedle platform opens a new realm of possibilities that can shape the future of healthcare worldwide. From continuous monitoring to multiplexed measurements of numerous biochemical biomarkers, real-time measurements, remote monitoring/care, and actionable feedback to the wearer are parts of the possibilities to be realized in this realm. A microneedle-based wearable sensing platform is the closest system to realizing such a possibility in a pragmatically viable fashion. The pain-free, blood-free, minimally invasive

microneedle tips gently access the revitalizing interstitial fluid (ISF) to initiate electrochemical transduction of the biochemical molecule of interest. Almost identically, ISF mimics the composition of the gold-standard blood, both chemically and temporally. ISF is considered the most reliable and clinically valid biosensing medium, especially in comparison to sweat, saliva, tear, urine, and stimulated ISF, and has a highly matured commercial and research track record.

The present thesis first, introduces the historical development of microneedle-based biosensors. Next, for the first time, it unravels the engineering and scientific fundamentals that make the idea of the "Lab-Under-The-Skin" a practical reality. The writing then elaborates on additional biochemical biomarkers of interest and their sensing mechanism when used in a microneedle-based form factor. Lastly, the thesis portrays the future of the microneedle-based wearable sensing field with an example from the cutting-edge electrochemical aptamer-based microneedle biosensing.

Chapter 1. The History of Microneedles

Lab under the Skin: The History of Microneedle-Based Wearable Sensors

1. Introduction

The staggering rate of technological advances over the past few decades has had a tremendous impact on every facet of our lives. Among all areas influenced by modern digital technology, the healthcare sector is one of the most important. Technological innovations have brought about numerous benefits to the healthcare arena, aiming to continuously improve the quality of life for the patients through more efficient patient care, improved public health, and reduced medical costs.

Biomedical diagnosis, a key component of healthcare, has witnessed considerable efforts toward moving from invasive blood-centered diagnostics, mainly implemented in hospital settings, to personalized, decentralized, and remote diagnostics. In this regard, wearable sensing platforms have become the center of attention not only for remote patient monitoring but for other potential applications, from wellness and nutrition monitoring to tracking safety and security. While initial efforts in the wearable sensing field focused on monitoring vital signs and physical metrics, recent attempts have mainly directed at realizing wearable chemical sensors capable of tracking the body's physiological state at the molecular level. Such next generation minimally, or non-invasive wearable devices can continuously measure the dynamically changing levels of clinically informative biomarkers in peripheral biofluids, such as sweat, saliva, tears, and interstitial fluid (ISF). Among these fluids, ISF has shown the greatest promise to replace the current gold standard blood-based clinical diagnostics. Over the past two decades, efforts have led to significant progress

in the area of ISF glucose sensing, with the latest generation of commercial, needle-based continuous glucose monitoring (CGM) devices offering accurate, calibration-free, and real-time glucose measurements in subcutaneous fat tissue for up to two weeks. Such CGM devices have gained wide acceptance in diabetes care, and as the new standard of care, they have started to replace the self-monitoring blood glucose (SMBG) strips.[1]

ISF is formed by transcapillary filtration of blood and surrounds the cells and tissues of the body. ISF is responsible for transporting nutrients and waste products between blood capillaries and cells, signaling molecules between cells, and antigens and cytokines to lymph nodes for immune regulation.[2,3] Compared to other biofluids, ISF has the closest composition to the blood, with biomarker concentrations and temporal profiles similar to those in blood.[4] ISF also offers numerous advantages over blood as it does not clot due to the impartial availability of coagulating factors, and thus it can be used for continuous monitoring of biomarkers.[5] Besides, ISF can be sampled in a minimally or non-invasive manner and provides a simpler biological sample for analysis as it has lower concentrations of high-abundance, blood-based proteins such as albumin and globulins.[6,7] Owing to the contact with the surrounding cells, ISF can also provide local information on tissues' status without the need for biopsies.[8] Many recent metabolomic, proteomic, and transcriptomic studies have shown that ISF contains many biomarkers that are unique or even at higher concentrations than those in blood.[5–10] Such advantages have motivated researchers to exploit ISF analysis as a reliable proxy to the current blood-based clinical practices toward reliable on body monitoring.

Despite all the benefits, the difficulty in accessing the ISF biofluid has highly restricted its widespread sensing applications. While several strategies have been developed for ISF sampling, such as suction blister,[8,11] microdialysis,[12,13] laser microporation of skin,[14] reverse iontophoresis

(RI)[15] and microneedle arrays,[16–18] only the latter two techniques have shown promise for continuous monitoring purposes. RI relies on applying an electric field to induce an electroosmotic flow across the skin. This method was utilized in the first non-invasive FDA-approved wearable CGM device in 2000, the GlucoWatch (Cygnus Inc., CA). GlucoWatch was subsequently retracted from the market, mainly because of skin irritations due to the relatively high iontophoretic electrical current. Although recent efforts have aimed to improve the RI technique toward continuous non-invasive biomarker monitoring,[15,19] it still suffers from major limitations, including ISF dilution, considerable lag time due to the additional time required to apply the current, narrow scope of detectable analytes, and contamination by the sweat on the skin surface.[4,20]

On the other hand, microneedle arrays have emerged as promising tools to directly access the ISF for real-time biomarker monitoring. Such sharp microscopic structures are barely visible and can easily puncture the stratum corneum (the outermost layer of the skin) and sit in the viable epidermis to enable the real-time analyte measurements.[3] By virtue of their dimensions, microneedles access the ISF at less than 1 mm depth (much shallower compared to the 5-11 mm depth of conventional CGMs placing in subcutaneous fat tissue)[21] and do not reach the nerve endings and capillary bed in the underlying dermis. Inspired by the success of current CGM devices, microneedle-based sensors represent the next major milestone in wearable sensors. Microneedles can thus provide a blood-free, pain-free, and minimally-invasive effective means for accessing the ISF biomarkers. A distinct advantage of microneedle devices is their ability to accommodate multiple independent sensors on a single miniaturized array, to provide timely multiplexed molecular information.

Over the past few years, increasing attention has been given to microneedle-based diagnostic devices, from both research and commercialization perspectives, as reflected by the subject of several recent review papers.[3,22–32] These previous papers have emphasized various aspects of the usage of microneedle sensors including the skin anatomy, fabrication methods, and covered different sensing formats. In the current paper, we distinctly limit our discussion to microneedles capable of on-the-tip sensing as these offer the greatest potential for integration with miniaturized wearable devices towards comprehensive monitoring of the wearer's health status. We start our discussion with a short coverage of the historical evolution of microneedles, followed by a brief discussion of the fabrication techniques commonly used for microneedle sensors, and highlights of various (bio)recognition approaches and electrochemical transduction techniques for realizing microneedle-based chemical sensing. These sections are followed by a detailed discussion on the single and multi-analyte microneedle sensing devices based on the use of microneedle arrays. The final section deals with a future roadmap and the challenges of translating microneedle sensing platforms from the bench to the body.

2. Historical Evolution of Microneedle-Based Sensors

Microneedle technology has witnessed enormous progress over the past few decades. **Figure 1** shows the historical journey of microneedles from the birth of the idea in the 1970s to the current state-of-the-art prototypes, highlighting the significant breakthroughs in microneedles development, with a focus on diagnostic applications. The first description of the concept dates back to 1976,[33] when Gerstel and Place suggested a drug delivery device based on an array of needle-like projections with 5-100 μm length which can penetrate the stratum corneum to produce some desired pharmacological or physiological effects (**Figure 1a**). It took more than two decades till the advances in microfabrication techniques allowed the researchers to realize the first example

of a microneedle-based drug delivery device. In a pioneering report by Henry *et al*. in 1998, the reactive ion etching microfabrication technique was used to fabricate an array of 150 μm long microneedles. The in-vitro study of this microneedle array on a human skin-mimicking platform indicated an enhanced transdermal permeability of calcein as a model drug (**Figure 1b**).[34] Ever since, the field of microneedle-based transdermal drug delivery has experienced a rapid expansion for administering a wide variety of drugs, vaccines, or even genes.[35–43] Several of these microneedle delivery devices have been FDA-approved or are currently in the clinical evaluation stage.

The first microneedle-based sensing approach appeared in 2000,[44] relying on a single in-plane silicon microneedle integrated with microcuvette to analyze glucose content in the withdrawn 200 μL of blood sample. Such principle of on-the-chip sensing was followed shortly after by similar studies involving ISF extraction rather than blood.[45,46] In a notable example by Mukerjee *et al*. (**Figure 1c**),[46] a hollow silicon microneedle array was applied to the skin to transfer ISF from the microneedle bores to an integrated colorimetric glucose sensor on the opposite side through the microfluidic channels. While offering innovative fabrication protocols with fine control on needle's geometry, shape, and size, the concept could hardly be adapted for real-time measurements of biomarkers due to its challenges, such as the limited volume of the extracted ISF, clogging issue, and the considerable lag time between biomarkers' profiles in blood and the sampled fluid.

In 2010, a novel microneedle sensing concept was introduced by Corrie *et al*. based on the functionalized solid microneedles to capture circulating biomarkers in-vivo followed by post-analysis with an analytical instrument (**Figure 1d**).[47] This method has been improved over time, mainly in terms of the time needed to capture the protein biomarkers,[48–51] and expanded recently

to capture other markers of clinical interest such as cell-free DNA.[52,53] Microneedles made of swellable hydrogels have also been adopted by several groups for extracting ISF towards off-body metabolic analysis.[54,55] However, the necessity to perform the analysis outside the body largely impedes applying such methods for continuous monitoring of biomarkers.

The most practical microneedle-enabled sensing format was illustrated in 2011 by two reports from Wang's group, based on assembling the sensing component on the tip of microneedles.[56,57] Such on-the-tip sensing was initially demonstrated using carbon paste-packed polymeric hollow microneedles to detect hydrogen peroxide and lactate as model analytes, the latter in connection to a lactate oxidase (LOx) enzyme[57] (**Figure 1e**). The second report described a bicomponent platform based on the integration of hollow microneedles and Pt-modified solid microneedles to enable enzymatic detection of glutamate and glucose using their respective oxidase enzymes.[56] Such a format allows direct contact of the sensors-embedded microneedle array with the dermal ISF, and can enable in-situ, continuous acquisition of clinical data without any sample treatment or extraction. These pioneering reports have sparked the expansion of the concept over the past decade toward fabricating several sensing prototypes for a wide variety of biomarkers. The first example of multiplexed microneedle sensors was illustrated in 2012 by Miller *et al*. for simultaneous electrochemical detection of multiple analytes including pH, lactate, and glucose (**Figure 1f**).[58] This was followed in 2014 by a microneedle-based self-powered glucose sensor, relying on the correlation of power output of the biofuel cell system and the glucose 'fuel' concentration (**Figure 1g**).[59]

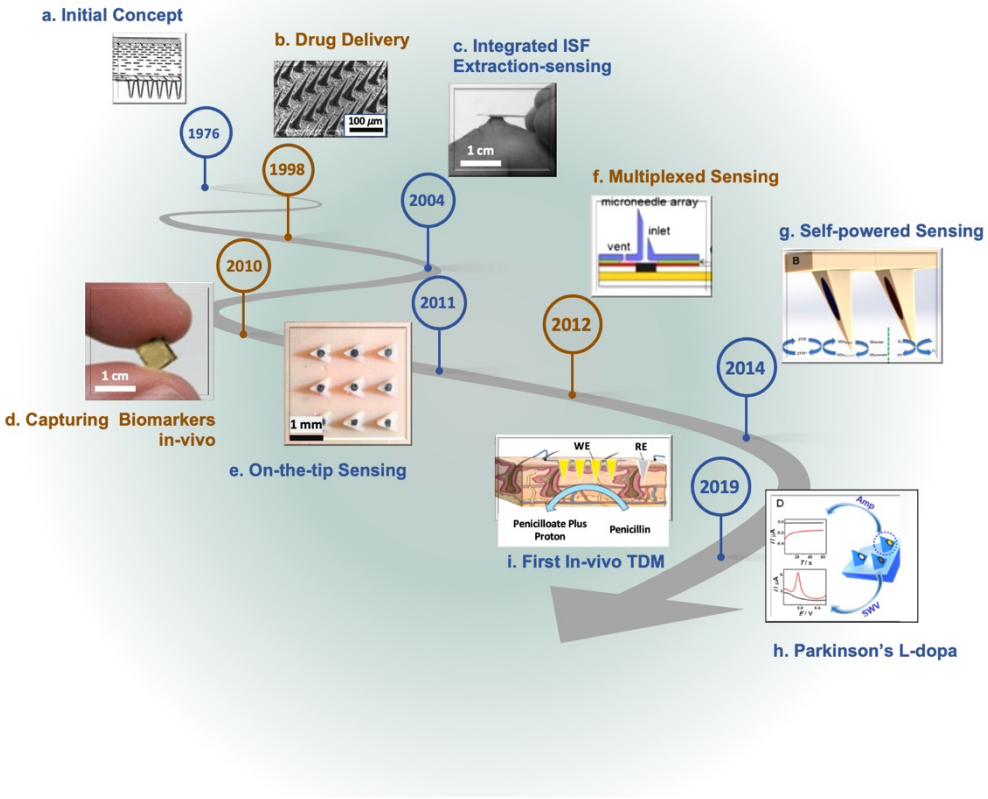

Figure 1. 1. Major accomplishments in the history of microneedle devices, with the focus primarily on sensing applications: **a**) The first description of a micro-projection-based drug delivery device. Reproduced with permission. [33] Copyright 1976, US Patent US3964482A. **b**) First microneedle drug delivery device developed by reactive ion etching fabrication technique. Reproduced with permission. [34] Copyright 1998, Elsevier. **c**) Hollow silicon microneedle array for interstitial fluid (ISF) extraction and on-chip sensing for glucose analyte. Reproduced with permission. [46] Copyright 2004, Elsevier. d) First functionalized microneedle for capturing the circulating biomarker in in-vivo settings. Reproduced with permission. [47] Copyright 2010, Royal Society of Chemistry. **e**) First microneedle sensor using on-the-tip sensing format based on carbon paste-packed hollow microneedles. Reproduced with permission. [57] Copyright 2011, John Wiley and Sons. **f**) First multiplexed microneedle sensor. Reproduced with permission. [58] Copyright 2012, Elsevier. **g**) The first microneedle-based self-powered sensor. Reproduced with permission. [59] Copyright 2014, Elsevier. **h**) Microneedle-based therapeutic drug monitoring (TDM) of levodopa (L-dopa). Reproduced with permission. [17] Copyright 2019, American Chemical Society. **i**) The first in-human evaluation report on TDM. Reproduced with permission. [18] Copyright 2019, American Chemical Society.

There has also been a growing interest to expand the range of detectable analytes beyond common metabolites, such as glucose or lactate present at high millimolar (mM) concentrations. In this regard, the use of microneedles for therapeutic drug monitoring (TDM) has received increasing recent attention.[60] Some of the elegant examples of such microneedle systems

developed for TDM applications have been shown in **Figure 1**. **Figure 1h** illustrates unmodified and tyrosinase enzyme-modified carbon paste-packed microneedles (on the same patch) to enable orthogonal detection of L-dopa for monitoring Parkinson's disease patients.[17] **Figure 1i** shows a first in-human evaluation of solid microneedles for monitoring antibiotics,[61] relying on ß-lactamase enzyme-modified iridium-oxide deposited microneedles for measuring penicillin antibiotic drugs using potentiometric detection of the protons liberated from the enzymatic reaction.

The continued innovations over the last few decades in various fields of micro/nanofabrication techniques, material sciences, digital technologies, biosensing platforms, and flexible electronics have accelerated the development of powerful miniaturized microneedle-based detection systems. Microneedles currently offer a tremendous future potential to realize wearable sensors toward on-body monitoring of a wide range of metabolites, electrolytes, therapeutics, illicit drugs, chemical threats and even hormones, proteins and genes. Supported by the distinct multiplexed sensing ability of microneedle arrays involving multiple individually addressable sensing tips on the same patch, it is possible to realize a powerful diagnostic lab under the skin surface. Furthermore, the drug delivery capability of microneedles can be merged with the sub-skin microscale laboratory, helping patients to autonomously self-manage a wide variety of chronic diseases. Yet, there are still grand challenges in advancing the microneedle-based detection technology to routine on-body sensing devices. These reflect the goal of direct reliable measurements at the microneedle tip without any sample manipulation. Some major challenges include reliable skin penetration, surface biofouling and related inflammatory response, sensitivity and selectivity and the need for extensive clinical validations. However, the benefits of realizing

real-time continuous simultaneous monitoring of multiple chemical markers outweigh these risks and justify extensive research efforts and proper investments to tackle these challenges.

3. Microneedles as electrodes

3. 1. Microneedle Fabrication Methods

The field of microneedles has witnessed exponential growth since the first demonstration of a microneedle based on silicon microfabrication technology.[34] A wide variety of microneedle designs has been introduced (*i.e.*, solid, hollow, porous, swellable, and dissolving microneedles) using various fabrication techniques. Diverse materials have been employed for fabricating the microneedles, including silicon, glass, metal, polymers, and carbohydrates. A key challenge in developing effective microneedle sensor arrays is the requirement to fabricate low-cost devices that retain the tip sharpness of silicon microneedles. As the current review focuses on microneedle sensors, we limit our discussion here primarily to solid and hollow microneedles and a brief overview of their fabrication methods. We refer our readers to some excellent recent reviews for thorough and comprehensive discussions on the microneedle manufacturing methods.[32,62,63]

Figure 2 shows various techniques that are commonly used for fabrication of microneedle sensors along with their corresponding materials. *Photolithography* is now a mature technology that has been the forefront of silicon-based microneedle array fabrication. This method generally involves the use of silicon wafers with desired thickness and diameter that are coated with either positive or negative photoresist, a UV exposure step, and subsequently an etching process to form microneedles with varying size, height and geometry. Photolithography has extensively been utilized for the fabrication of hollow, solid, and planar microneedle arrays, either by using wet (involving solvents) or dry (by vapor plasma or plasma) etching procedures.[34,45,63–67]

Photolithography-based techniques offer high reproducibility and resolution in fabricating solid and hollow microneedles. Nevertheless, these techniques involve complex, multistep and costly procedures. Additionally, the producible maximum height of the microneedle array is dictated by the thickness of the used silicon wafer.

Micro-molding is another widely used fabrication technique of microneedles as it is simple, scalable, and low cost.[62,68–70] Micro-molding is basically a technique where the final structure is fabricated by the use of molten or liquid form materials such as molten metals or polymeric resins poured into a micro-mold being premade as the negative of the final structure. In case of fabricating ceramic based MNs, the ceramic slurry is cast into the mold followed by a sintering process. The poured material is then transformed, after degassing, to the final solid form using a variety of methods such as UV photocuring for polymeric microneedle structures and air, water, or oil cooling for metal-based structures. However, micro-molding is mostly limited to solid microneedle arrays and also provide lower resolution compared to other methods. Hot embossing, and injection molding can be categorized under micro-molding fabrication method, where external pressure is applied to the precursor material inside the cast before it fully solidifies to form the microneedle array. These two methods can partially address the issues associated with micro-molding techniques.

Drawing lithography, first proposed by Lee *et al*.[71], is another fabrication method in which a melted polymer is drawn from a planar substrate directly to a 3D microneedle structure without the need for a mask and light irradiation. The advantages include low-cost fabrication and overcoming the length and sharpness dimensional limitations.[32,72] The primary limitation of this method lies in the limited choice of the materials that can be processed. Magnetorheological drawing lithography (MRDL) is a modified form of drawing lithography, in which an external

magnetic field is used to draw a droplet of a curable magnetorheological fluid to form 3D microneedle structures with improved sharpness and length of the resulted microneedles.[73]

The next interesting fabrication method is *micromachining* explored by Wang's group.[74,75] This method is a top-down technique with the final structure produced by removal of a stock material to the desired geometry. The desired geometry is first virtually created in a 3D modeling software, and then transferred to the micro-computer numerical control (CNC) machine that runs in XYZ axes while chipping off the materials from the stock material by the CNC bits installed on the tip of the moving CNC head. Aside from its reproducible precision, high yield, and scalability, the method offers other advantages of high-level flexibility in the microneedle design and geometry. Furthermore, this technique can be implemented to manufacture both hollow and solid microneedles using a wide variety of materials. Although the most frequently used materials for micromachining are the machinable polymeric materials (i.e., PMMA, Acrylic, Polycarbonate, etc.), some metals (i.e., Aluminum, 316L Stainless Steel) and even some softer ceramic materials can also be used for the fabrication of microneedle arrays. The disadvantages are related to the costs of the equipment and of the CNC milling bits and the need for a skilled operator.

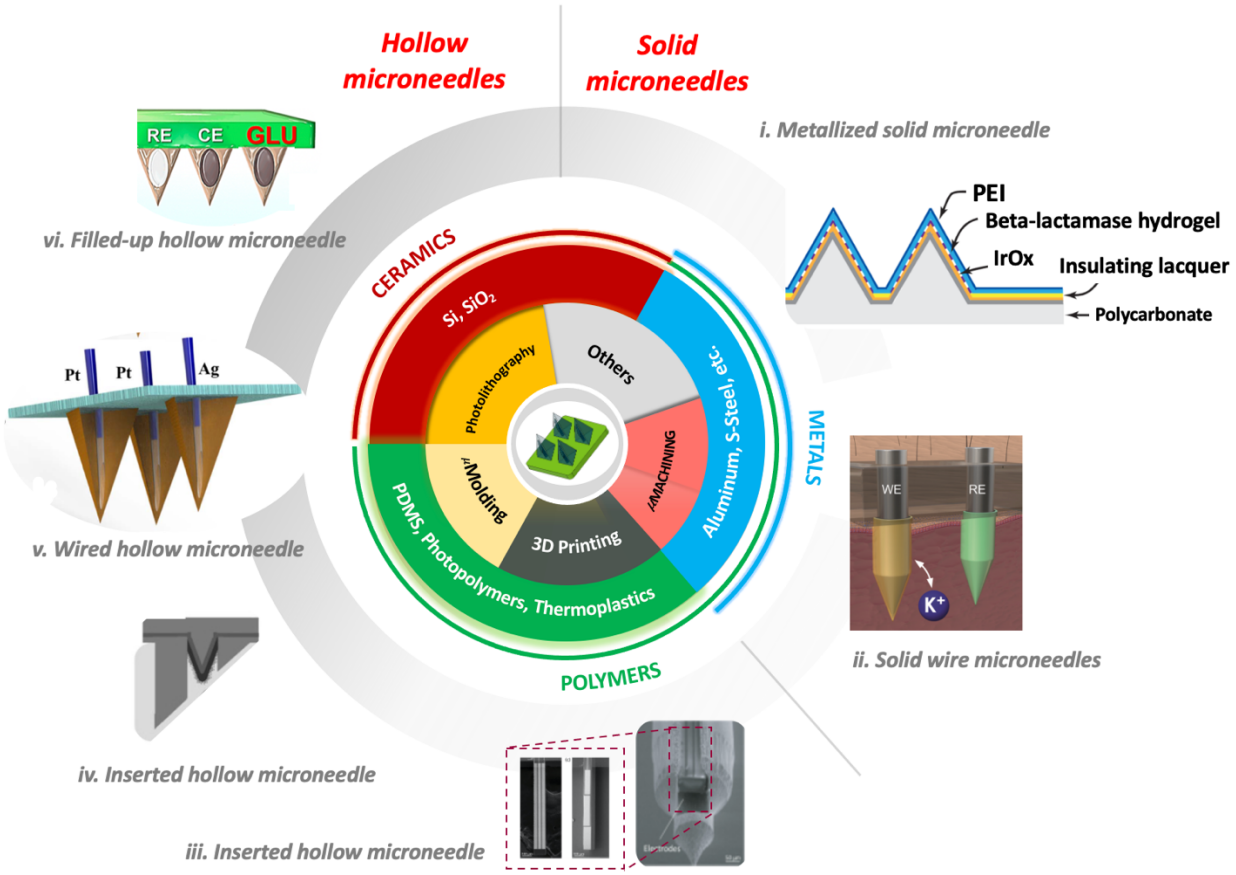

Figure 1. 2. Major fabrication methods. Hollow and solid microneedles highlighting the corresponding engineering materials that can be used by any of the methods. Outer diameter indicates the kinds of electrode/MN integration for on-the-tip sensing: **i**) Metallized solid microneedle reported for antibiotic detection. Reproduced with permission. [18] Copyright 2019, American Chemical Society. **ii**) Carbon and Ag/AgCl-coated stainless steel solid metal microneedles for potassium detection. Reproduced with permission. [76] Copyright 2018, American Chemical Society. **iii**) Photolithography-made miniature electrochemical probe inserted inside a single microneedle. Reproduced with permission. [77] Copyright 2018, Springer. **iv**) Biocomponent microneedle sensor based on integrating solid and hollow microneedles for the detection of glutamate and glucose based on their respective enzymes. [56] Reproduced with permission. Copyright 2011, John Wiley and Sons. **v**) Wire-embedded microneedle/electrode integration. Reproduced with permission. [78] Copyright 2017, Elsevier. **vi**) Carbon paste packed microneedle for glucose detection. Reproduced with permission. [75] Copyright 2020, American Chemical Society. Abbreviations: poly(ethylenimine) (PEI); Iridium oxide (IrOx); Polydimethylsiloxane (PDMS); Silicon (Si); Silicon dioxide (SiO_2); Micro-molding (mMolding); Platinum (Pt); Silver (Ag); Reference electrode (RE); Counter electrode (CE); and Working electrode functionalized with glucose oxidase (GLU).

3D printing is a method which primarily employs polymer-based photocurable resins or filaments for fabrication of microneedles. 3D printing is used here as a general term for

stereolithography (SLA),[79] fused filament fabrication (FDM),[80] digital light processing (DLP),[81] and scan, spin & selectively photocuring (3SP) methods. Even though 3D printing techniques are versatile fabrication methods in terms of microneedle geometry, spacing, height, numbers, etc., most of them are constrained by their limited true resolution (>50 μm). Such resolution leads to relatively dull MN tips, which specifically impacts skin penetration and subsequently, their sensing ability. An exception to this is the two-photon polymerization (TPP) stereolithography which allows the fabrication of higher resolution (10 nm) structures.[82] However, due to the extremely low micro-size throughput and extremely high price tag of the machine, TPP can be hardly considered as a viable alternative method for the fabrication of microneedles for sensing applications.

3.2. Design criteria of microneedles

The common required denominator for all these fabricating techniques toward a reliable skin penetration and transdermal sensing is a high resolution below 20 μm. Such resolution is particularly important for producing sharp microneedle tips which would allow skin penetration with negligible pain induction and skin damage, which also seems necessary toward mitigating the body immune response. Additional important factors for successful skin penetration include the aspect ratio of the microneedle, geometry (shape), needles spacing, and layout (distribution configuration) . For example, microneedles with a base diameter of 400 μm have demonstrated higher penetration percentage (60%) on cadaver skin compared to ones with 200 μm. Additionally, the microneedle array with 2400 μm of spacing, while requiring larger skin penetration force, showed 20% more skin penetration compared to those with 800 μm of spacing.[83] In another study, it has been shown that sharper microneedle tips reduce the required penetration force.[84] Other important considerations include the materials' mechanical fracture toughness, Young's modulus,

which determines the stiffness of the microneedle, and finally safety factors such as materials' biocompatibility. While designing the microneedle geometrical features, special attention should also be paid to the biomechanical properties of the skin to overcome the counteracting skin elasticity.

3.3. Microneedle-electrode integration

To realize on-the-tip electrochemical detection, the sensing electrodes should be close or at the tip of the microneedle. Such arrangements have been used in multiple electrode/microneedle integration variations, with examples for each variation depicted in **Figure 2 (i-vi**). The primary strategies for integrating the sensing electrodes involve solid and hollow microneedles, as summarized in this section. Solid microneedles can be sputtered with thin conducting films of the desired metal transducers on their surface **(Figure 2 i)** to make 2- or 3-electrode system devices.[18] Such configuration usually involves sputtering of several metal layers including an adhesion promoting layer (Cr or Ti), followed by sputtering of noble metals such as Au or Pt and finally Ag. Working and counter electrodes of Au or Pt are then formed by chemical etching of the top Ag layer while the reference electrode is obtained upon the Ag to form Ag/AgCl. This configuration is usually simple and straightforward which is followed by further chemical functionalization of the metalized microneedle for various sensing applications. The only limitation in such an integration strategy is to devise a method to reproducibly insulate the electrodes to ensure equal surface areas among different microneedle arrays. Another example of electrodes integration into the solid microneedles was reported by Parrilla *et al*. using PDMS-hosted, laser-cut stainless steel wires of 300 μm diameter (**Figure 2 ii**).[76] To realize microneedle potentiometric sensing, the working and reference electrodes were fabricated by dip coating of

stainless steel wires in commercial inks of carbon and Ag/AgCl, followed by coating of the respective ion-sensing cocktail polymer membrane solution.

Multiple electrode/microneedle integration strategies have also been devised for hollow microneedles. In inserted hollow microneedle strategy **(Figure 2 iii-v)**, an insert (i.e., a miniature electrode system, metal sputtered polymeric electrodes or a metallic wire) is embedded inside the lumens of a hollow microneedle array. These devices require proper sealing of the insert for defining the electrode area and preventing solution creeping. For example, Ribet *et al*. inserted a photolithography-made, miniaturized 3-electrode probe inside a single microneedle **(Figure 2 iii)**.[77] In an interesting strategy, metal-sputtered solid microneedles were included inside the hollow ones to serve as the electrodes. In this design, the hollow microneedle physically protects the embedded sensor and its reagent layers against potential friction to the skin during insertion, representing an advantage of this microneedle sensor configuration **(Figure 2 iv)**.[56] Another inserted integration protocol was described by Mohan *et al*., based on inserting the Pt and Ag metallic microwires inside the hollow microneedles and adjusting the wires to the tip of the microneedle **(Figure 2 v)**.[78] The wires can be functionalized either before or after insertion and insulated from the backside of the microneedle array to avoid movement during penetration to the skin. A small recess can be maintained to cover the working electrode with multiple reagent layers (imparting the necessary selectivity and stability). A similar recess can be used also for preparing packed hollow microneedle sensors. Such packed hollow microneedle arrays represent another type of preparing microneedle sensors which employs conductive inks or pastes, particularly carbon pastes along with the connection from the backside using silver epoxy **(Figure 2 vi)**.[75] The advantages of this method are relatively reproducible electrode surface areas and more importantly, the possibility of using the conductive paste for incorporating the sensing

components. Particularly attractive are enzyme-containing carbon pastes that offer high enzymatic stability. Further attention should be given to the automation of the electrode MN integration process towards large-scale manufacturing processes. This should be coupled with automated high-precision liquid dispensing systems for rapid functionalization of the resulting electrode transducers with the corresponding reagent layers reproducibly and scale-ability.

4. Recognition chemistries and the electrochemical transduction modes in microneedle sensors

Besides a few exceptions, almost all microneedle-based sensors reported so far have been based on electrochemical transduction approaches. This is due to their distinct benefits of electrochemical monitoring, such as inherent miniaturization, high speed, low cost, and low power consumption requirements, along with highly scalable fabrication and easier adaptation to microneedle ISF-sensing platforms.[60] Electrochemical (bio)sensors combine the sensitivity of electrochemical transduction methods with the selectivity of (bio)recognition elements.[85] In such sensors, the recognition event (i.e., the selective analyte-receptor interaction) is translated by the electrode transducer into a measurable electrical signal, whose intensity is proportional to the concentration of the target analyte. Different recognition chemistries and transduction modes can be combined and adapted in developing microneedle electrochemical sensors (**Figure 3**), the selection of which is determined by the targeted analyte. In the next section, we provide a brief discussion on different types of electrochemical microneedle (bio)sensors in terms of the exploited receptor and transduction modes.

4.1. Conventional Electrodes without Recognition Element

Conventional microneedle sensing electrodes, referred hereto as sensors in which no recognition element is used, are the simplest electrode configurations that have been adapted to

the microneedle sensors (**Figure 3 I)**. Such sensors are based on the use of the bare surface of the working electrode for detecting electroactive analytes, such as drug molecules, and are commonly relying on scanning-potential voltammetric measurements (mostly square wave voltammetry (SWV) and differential pulse voltammetry (DPV)) to provide high sensitivity along with the electrochemical (voltammetric) signature of the target analyte, the latter reflect the redox characteristics of the target analyte. **(Figure 3 I-a)**.[86] For example, unmodified carbon paste microneedle electrodes have been proposed for continuous ISF monitoring of fentanyl opioid molecules.[87] Fixed-potential amperometric measurements **(Figure 3 I-b)**, have also been applied for enzyme-free monitoring of metabolites (e.g. glucose).[88,89]

In the absence of a confined recognition element, the use of an unmodified microneedle electrode is prone to low selectivity. Efforts to enhance the selectivity and sensitivity of such microneedle ISF monitoring have involved the surface confinement of different nanomaterials onto the bare working electrodes for increasing the surface area and electrocatalytic activities,[87] or inducing enzyme-mimicking properties and thus, imparting partial selectivity to the sensor.[88] The detection capabilities can be enhanced by orthogonal detection combining of unmodified voltammetric microneedle electrodes with amperometric enzyme-modified electrodes.[17]

4.2. Ion-Selective Electrodes

Ion-selective electrodes (ISEs) convert primary ion activities to an electrical potential difference, measured by the potentiometric method **(Figure 3 II)**. The potential difference, developed across a selective membrane, is correlated to the logarithm of the ion activity according to the Nernst equation **(Figure 3 II-c)**.[41] The selectivity of potentiometric sensors comes from the incorporation of ionophore molecular receptors relying on the specific surface chemisorption and equilibrium partitioning of the primary target ions. Unlike the classical bulky ISEs, with inner

solutions, microneedle potentiometric sensors commonly rely on solid contact ISEs. Solid contact electrodes, usually based on ionophore-doped polymeric membranes, have especially attracted extensive interest over the last decade, owing to their high compatibility with modern micro/nanofabrication techniques towards the development of miniaturized, flexible sensors and the ease of merging with wearable technologies.[91] ISEs have also been reported in connection to microneedle platforms for monitoring the transdermal potassium ion concentrations.[76] Such integration of solid contact electrodes and microneedles offers valuable tools toward minimally-invasive, continuous tracking of electrolytes.

Potentiometric sensors are simple, fast, and low cost, and offer minimum power requirements.[92] Additionally, since the potentiometric signal does not depend on the electrode surface area, they are less prone to biofouling and foreign body response issues compared to voltammetric and amperometric techniques, which make them highly suitable for long-term in-vivo monitoring operations.[93] A variety of ionophore receptors are now available for selective ISF monitoring of key electrolytes. However, the overall selectivity of the corresponding microneedle sensor depends on their selectivity coefficients (discrimination against interfering ions) and the actual relative ISF concentrations of the target and interfering ions. The sensor should be capable of distinguishing the subtle differences of ISF electrolyte concentrations within a narrow range, such as 120-150 mM and 3.5-5.5 mM for Na^+ and K^+, respectively. The sensitivity of potentiometric MN sensors limits their operation to millimolar or sub-millimolar concentration ranges.

4.3. Enzyme-based electrodes

Enzymes are the most widely used recognition elements in biosensors design, owing to their selective behavior, simplicity, low cost, and regenerability.[85] Enzymes selectively catalyze the

conversion of a metabolite biomarker to generate a product **(Figure 3 III)**, that can be electrochemically detected using amperometry **(Figure 3 III-d)**, voltammetry **(Figure 3 III-e),** and potentiometry **(Figure 3 III-f),** depending on the redox behavior of the formed product. Amperometric enzyme electrodes using the oxidase family of the enzymes are the most common type of biosensors.[1,94] Oxidase enzyme-based biosensors for in-vivo monitoring applications rely mainly on measuring the oxidation current of the hydrogen peroxide enzymatic product. Such oxidase enzymes have been used with microneedle platforms toward sensing of biomarkers such as glucose,[56,77,95] alcohol,[78] glutamate[56], lactate[57,96], and theophylline[97]. Other types of enzymes have also been incorporated into microneedle sensing devices, including ß-hydroxybutyrate dehydrogenase,[75] and tyrosinase[17] for amperometric monitoring of their corresponding substrates of ketone bodies and L-dopa, respectively. Despite the widespread use of dehydrogenase enzymes in electrochemical biosensors, their adaption to continuous microneedle monitoring applications requires attention to the stable confinement of their NAD^+ cofactor and the stable detection of the NADH product. While enzymes offer the most promising recognition capability, they face some barriers such as their restricted long-term operational stability and more importantly, the limited number of available enzymes and thus, the limited scope of analytes that can be readily detected by enzyme electrodes.

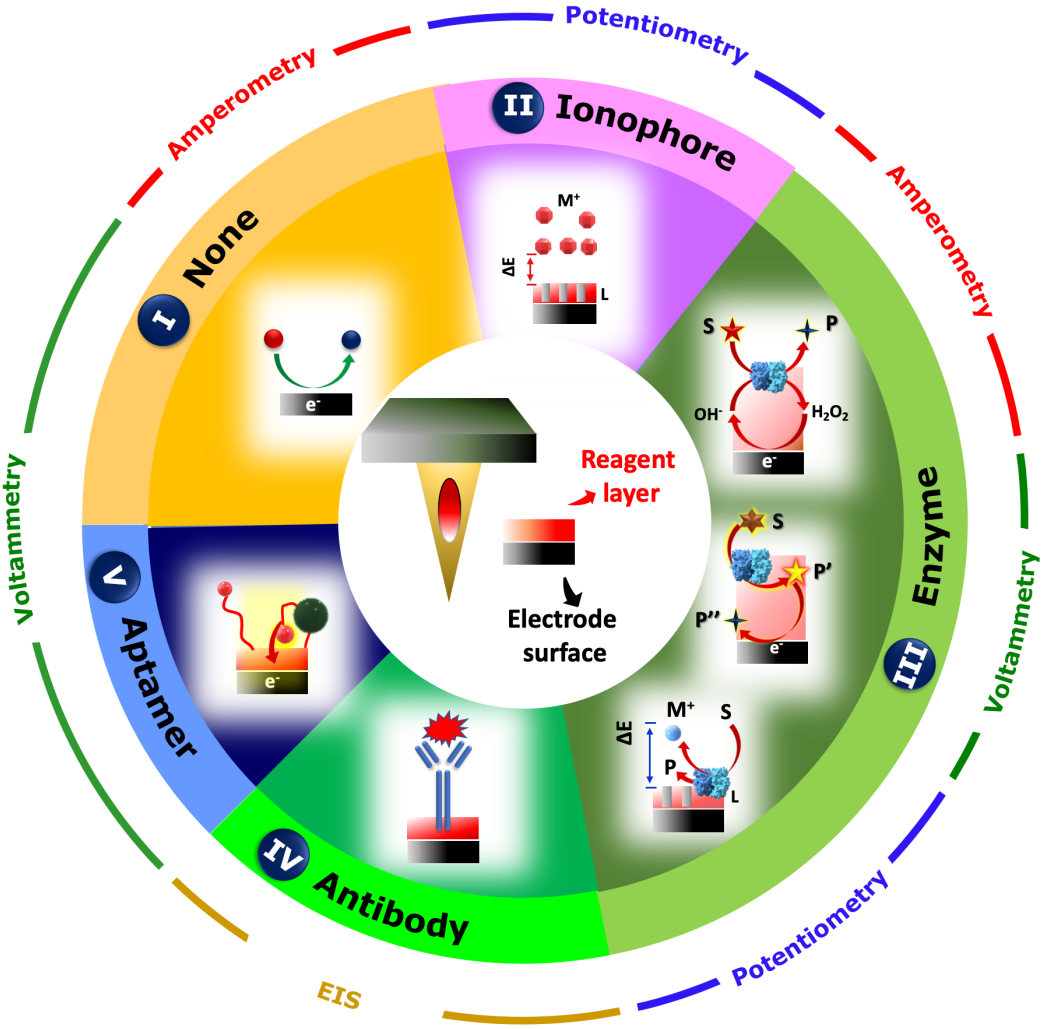

Figure 1. 3. The recognition chemistries and electrochemical signal generation methods. This can be adapted into microneedle-based sensors. I- Conventional electrodes with no recognition element, in which either voltammetric or amperometric transducers are applied. II- Solid-contact ion-selective sensors based on the use of ionophores and potentiometric transduction for monitoring of electrolytes. III- Enzyme-based biorecognition which, depending on the analyte of interest, can be used along with amperometry, voltammetry, and potentiometry. IV- Affinity biosensors based on antibody-antigen recognition, in which the impedimetric signal is measured for a label-free, non-Faradaic mode. V- Aptamer-based recognition, based on a reversible, binding-induced conformational change of the aptamer receptor, in which the resulting alteration in electron transfer of redox reporter tag is voltammetrically measured. Abbreviations: Substrate (S); Product (P, P', P''); Ionophore (ligand, L) and Ionic species (M^+).

4.4. Affinity sensors

Affinity sensors employ the strong and selective binding of immobilized bioreceptors, like antibodies or oligonucleotides to the target analytes, usually governed by the size and shape or

base complementarity, to produce a measurable analytical signal.[85] Antibody-based sensors, known as immunosensors, typically use an enzyme-tagging strategy hand are currently the gold standard in-vitro assays for highly sensitive (nM and pM) and specific quantitation of a wide spectrum of analytes including drugs, pesticides, hormone and protein biomarkers, bacteria and viruses. While there are also several reports on developing microneedle-based immunosensors, such platforms have solely been limited to in-vivo capturing of different antigens, followed by the off-body analysis of the captured biomolecules. This reflects problems inherent to the antibody bioreceptors such as slow kinetics of binding, poor stability, multistep transduction procedure requiring additional tagging, washing and detecting reagents, and most importantly, difficult regeneration of binding sites which impedes continuous on-body sensing operation.[92,98] A potential immunoassay format for on-body sensing could be based on label-free and wash-free, non-Faradaic approaches using impedimetric transduction **(Figure 3 IV-g)**;[99,100] yet, these approaches still need an efficient strategy to overcome the antibody regeneration issue.

Aptamers are another class of affinity sensors that have attracted increasing attention in recent years to realize continuous, in-vivo monitoring applications. Aptamers are artificial nucleic acid ligands that are produced through a process called SELEX (systematic evolution of ligands by exponential enrichment) and exhibit a specific binding affinity for amino acids, drugs, and protein biomolecules.[101] The easy modification of aptamers with redox markers (e.g. methylene blue) and their reversible and fast binding with the target analyte offer the promising opportunity of integrating aptamers with microneedle arrays toward continuous, high-frequency monitoring of a vast panel of biomarkers; a merit that is not affordable by other receptors. Signal transduction in aptamer-based sensors commonly relies on measuring a binding-induced conformational change in the aptamer receptor, producing changes in the electron transfer characteristics of the redox

reporter molecule (typically followed by SWV) which are proportional to the concentration of theanalyte of interest (**Figure 3 V-h**).[102] While aptamers have demonstrated promising capability toward specific, sensitive, and rapid detection of drugs in the blood veins of ambulatory animals; yet, expanding the protocol to minimally-invasive microneedle-based aptamer sensors for ISF monitoring of various analytes including larger size protein biomarkers needs more systematic efforts in the future.[103]

5. Single-analyte microneedle sensors

Initial stages of research on microneedle-based sensors involved ISF extraction coupled with a commercial or custom-designed sensor to measure the levels of an analyte in the drawn ISF. The ISF extraction is mainly implemented through the capillary forces through the internal walls of hollow microneedle arrays,[46] or through puncturing the skin by an array of microneedles to create micron scale holes across the skin followed by applying a negative pressure to collect some measurable volume of ISF.[104] In such designs, sensing is completed either in-line enabled by microfluidic channels to bring the extracted ISF to the on-the-chip electrochemical detector, or off-line using a laboratory-based procedure. Other ISF extraction protocols have also been introduced over the last years, such as swellable hydrogel-based microneedles.[54,55] These methods are not adaptable for continuous monitoring since they face numerous problems, including their inability to extract a sufficient amount of ISF, complicated design and setup of microfluidics, and long turnaround analysis times. On-the-tip microneedle-based sensing was introduced in 2011 to overcome these challenges[56,57] and since then, numerous reports have demonstrated its attractive features toward continuous, real-time monitoring for a variety of clinically informative analytes. In this section, we summarize some representative examples of the microneedle sensors.

5.1. Microneedle-based CGM devices

Frequent monitoring of glucose levels is essential toward effective management of diabetes. The current generation of wearable CGM devices provides accurate analytical data regarding the duration, direction, and magnitude of ISF glucose levels without the need for calibration against blood glucose.[105] Yet, the needle-type CGM devices are invasive as the smallest type of such devices employs a 9-mm long and 27-gauge (420 μm diameter) needle.[30] In contrast, microneedles with typical tip diameters of 50 μm reach the ISF in less than 1 mm and thereby, offer a minimally-invasive tool for glucose monitoring without compromising the sensor accuracy.

Jina *et al.* from ArKal Medical Inc (Fremont, CA) were the first to report microneedles for long-term, in-vivo continuous glucose measurement.[16] A microneedle array of 200 hollow silicon microneedles, each approximately 300 μm in length with a 50 × 50 μm lumen over a total area of 6 × 6 mm was applied to the skin via a spring-loaded applicator (**Figure 4a**). A screen-printed biosensor, including a GOx-modified Pt/C working electrode, was integrated with the microneedle and placed on the opposite side of a glucose collection chamber. Ten diabetic subjects participated in the clinical study to evaluate the accuracy of the microneedle CGM by wearing 4 microneedle devices on each subject. Calibrations were carried out using blood glucose meters after an initial 2-hour warm-up period and then once daily with the morning fingerstick glucose value (**Figure 4a**).[16] Comparison of 1396 paired device glucose measurements and fingerstick blood glucose readings for up to 72-hour wear time demonstrated the accuracy of the device with the overall mean absolute relative difference (MARD) of 15%, with 98.4% of the results residing in the A+B region of the Clarke error grid.[16]

Sharma *et al.* reported the application of solid microneedle arrays for CGM, where epoxy-based negative photoresist material (SU8 50) was used for fabricating the microneedles, followed by thin film sputtering of Pt and Ag/AgCl to form the electrodes (**Figure 4b**).[95,106] The Pt-sputtered microneedles were functionalized by entrapping the GOx enzyme in polyphenol via electropolymerization. Prior to in-vivo trials, the microneedles were sterilized by 25 kGy of gamma radiation, which had a small effect on the sensitivity of the sensors. The performance of the sensors was assessed in healthy and type 1 diabetes subjects for 24 hr, with the microneedle readings compared and calibrated against venous blood glucose data.[95] While it is hard to conclude a strong correlation between the microneedle CGM and blood readings (**Figure 4b(ii))**, an overall MARD of 9% has been claimed with over 94% of data points falling within the A and B zones of Clark error grid.[95] Ribet *et al*. positioned a microfabricated glucose biosensor inside the lumen of a single hollow silicon microneedle and employed the microneedle device for in-vivo CGM.[77] The 700 μm long silicon microneedle with approximate lumen diameter of 90 μm was fabricated with a sequence of isotropic and anisotropic dry etching steps on front and back sides of a silicon wafer (**Figure 4c**).[77] The anodic detection of H_2O_2 was carried out at 0.55 V vs. an integrated IrOx pseudo-reference electrode. The in-vivo characterization of the microneedle CGM device was performed by applying the device on the forearm of a healthy human volunteer in a glucose tolerance test, where the subject intakes a high sugar dose under fasting conditions. The results were well correlated with the reference finger-prick blood glucose readings measured at 10 min intervals (**Figure 4c(ii)**), proving the potential of such a device toward accurately measure the glucose in intradermal compartment of the skin.

Figure 1. 4. Examples of glucose detection using microneedle-based sensors. a) Hollow silicon microneedle array-based glucose sensor integrated with a three-electrode system on the back (**i**). The measured glucose data by two independent microneedle arrays on the same human subject (solid and dashed blue curves) and reference blood glucose data (red points) over 72 hours (**ii**). Reproduced with permission. [16] Copyright 2014, SAGE publications. **b**) An array of 64 metalized solid microneedles comprising 4 × 4 microneedles (i), where two collections of 16 Pt-sputtered microneedles served as two independent working electrodes and the other two corners of the pod involved Pt- and Ag-sputtered microneedles as counter and reference electrodes, respectively. The correlational response plot for the two developed sensors (WE-1 and WE-2) with the YSI blood analyzer over 20 hours, Reproduced with permission. [95] Copyright 2018, Royal Society of Chemistry. **c**) SEM micrograph of a single hollow silicon microneedle with the embedded glucose biosensor (**i**). Images of the two different configurations of the electrode system (**ii**). Time-dependent responses for glucose monitoring with the developed microneedle system correlated with finger-prick blood glucose data (**iii**). Reproduced with permission. [77] Copyright 2018, Springer. d) Schematic representation of the developed microneedle sensor probe using highly porous gold for second-generation glucose biosensing (**i**). SEM micrograph of the sensor probe showing surface topology of activated porous gold and the cyclic voltammetric response of the sensor in the absence and presence of glucose. Reproduced with permission. [107] Copyright 2019, MDPI. **e**) Self-powered microneedle-based glucose monitoring system. Schematic illustration of the catalytic reactions on bioanode and cathode. Optical image of the microneedles (cross sectional view), **i**). The obtained power density for varying glucose concentrations from 0 to 25 mM in 5 mM increments (**ii**). Adopted with permission. [59] Copyright 2014, Elsevier. Abbreviations: Reference electrode (RE); Working electrode (WE); Counter electrode (CE); Flavin adenine dinucleotide-glucose dehydrogenase (FAD-GDH); 6-(ferrocenyl)hexanethiol (FCSH); Gold microneedles (Au MNs); tetrathiafulvalene (TTF) and Glucose oxidase (GOx).

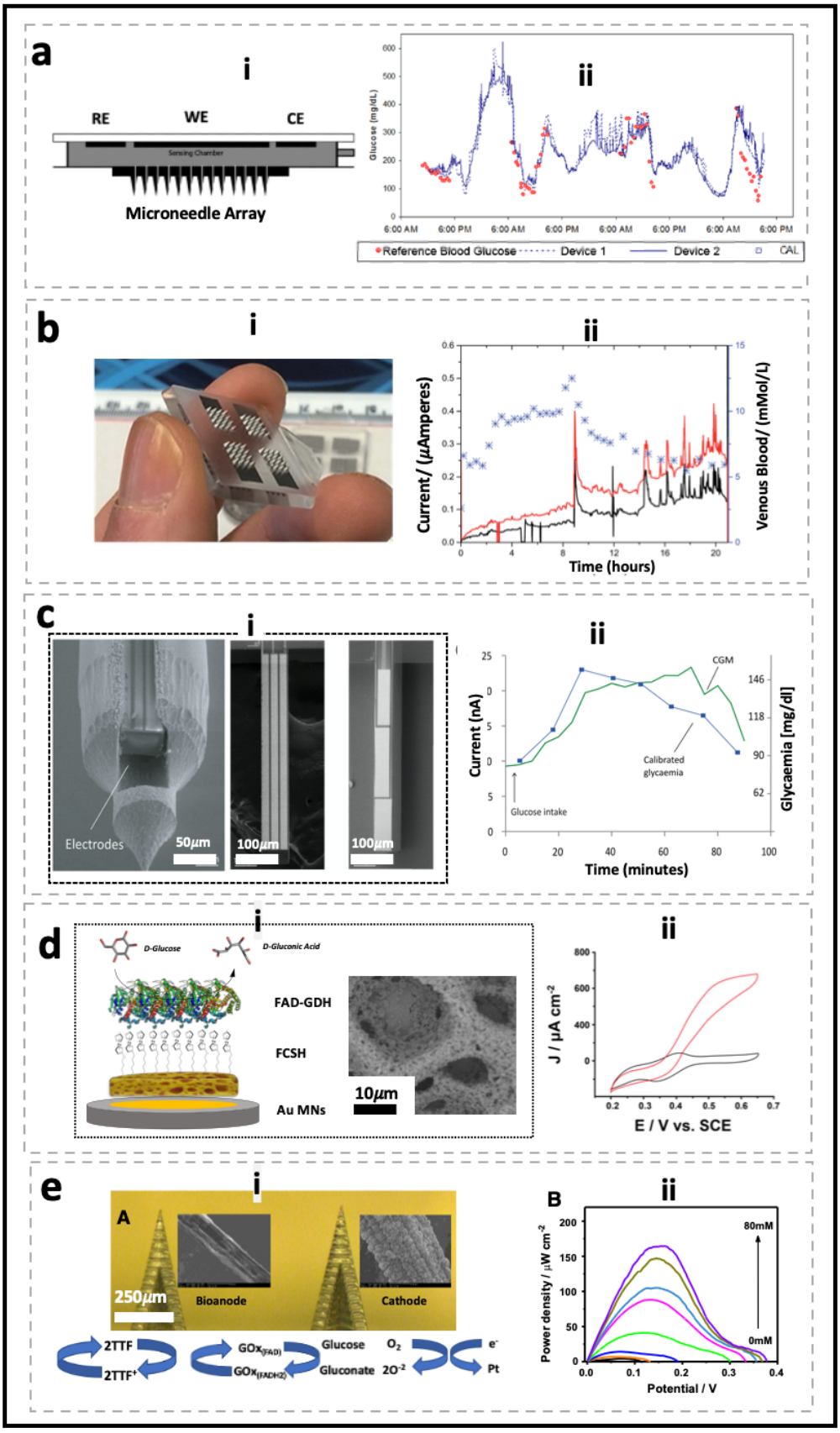
a
i
RE
WE
CE
Sensing Chamber
Microneedle Array
ii
Glucose (mg/dL)
6:00 AM
6:00 PM
Reference Blood Glucose
Device 1
Device 2
CAL
b
i
ii
Current/ (μAmperes)
Venous Blood/ (mMol/L)
Time (hours)
c
i
Electrodes
50μm
100μm
100μm
ii
Current (nA)
Glycaemia [mg/dl]
CGM
Calibrated glycaemia
Glucose intake
Time (minutes)
d
i
D-Glucose
D-Gluconic Acid
FAD-GDH
FCSH
Au MNs
10μm
ii
J / μA cm-2
E / V vs. SCE
e
i
A
250μm
Bioanode
Cathode
2TTF
2TTF+
GOx(FAD)
GOx(FADH2)
Glucose
Gluconate
O2
2O-2
e-
Pt
ii
B
Power density / μW cm-2
80mM
0mM
Potential / V

Bollella *et al.* described a CGM microneedle device for in-vitro glucose measurements in artificial ISF which relied on a second-generation transduction mechanism.[107] Highly porous gold was formed through an electrochemical self-templating method and used as the microneedle-based electrode transducer to enhance the active surface area (**Figure 4d**). The porous gold microneedle electrode was functionalized with a thiolated ferrocene derivative, followed by modification by flavin adenine dinucleotide (FAD)-dependent glucose dehydrogenase (GDH) enzyme (**Figure 4d**). The microneedle electrode presented a typical ferrocene-mediated electrocatalytic oxidative current in the presence of glucose and was assessed by amperometric glucose detection at 0.5 V vs. SCE.

On-body biofuel cells (BFCs) capable of harvesting biochemical energy from body fluids provide an attractive approach to realize autonomous energy supply in medical devices.[108,109] Valdés-Ramírez et al. described the first example of a microneedle-based BFC for glucose sensing, based on integrating carbon paste bioanode and cathode into a hollow microneedle (**Figure 4e**).[59] The bioanode was obtained by mixing carbon paste with the GOx enzyme and tetrathiafulvalene (TTF) mediator while the cathode relied on a platinum black-carbon paste mixture (**Figure 4e**). The performed experiments in artificial ISF solution demonstrated a strong correlation between glucose biofuel concentration and the power density, along with a good selectivity in the presence of electroactive constituents and long-term stability.

5.2. Microneedle-based monitoring of other analytes

Apart from the advances made in microneedle-assisted CGM, the utility of such microneedle sensors has also been explored for the detection of other clinical markers. To this aim, various recognition chemistries and electrochemical transduction methods have been combined and adapted on either solid or hollow microneedle electrodes. Driven by the known contribution

of ions in the normal functioning of the body and their relevance to dehydration and electrolyte imbalance-related diseases, the design and development of wearable sensors for real-time, in-vivo monitoring of ions is extremely important. While Miller *et al.*[110] were the first to describe microneedle-based potassium ion sensing relying on ISF extraction coupled with microfluidic channels and porous carbon potentiometric sensor, the recently reported work by Parilla *et al.*[76] considerably improved the initial concept of microneedle potassium sensor toward its real applications. For this, a stainless steel solid microneedle was coated sequentially with layers of carbon ink, functionalized carbon nanotube (f-MWCNT), and potassium-selective polymeric membrane to form the working electrode. For the reference electrodes, the coating was performed with Ag/AgCl ink, poly (vinyl butyral), and polyurethane layers (**Figure 5a**). The ex-vivo experiments of the potentiometric sensors in chicken and porcine skin showed attractive features of the developed platform toward ISF potassium monitoring within both clinical and harmful levels. A negligible signal drift was seen over prolonged operation of the sensor (0.35±0.28 $mV.h^{-1}$), attributed to the highly lipophilic nature of f-MWCNT avoiding the water layer formation in the electrode-membrane interface. In vitro cytotoxicity studies were also performed, indicating the appropriate and safe short-term performance of the intradermal potassium microneedle sensor.

Enzyme-based biosensors, especially oxidase enzymes, have frequently been utilized in microneedle patches for monitoring of clinical markers including glutamate,[56] lactate,[96] alcohol,[78] etc. For instance, a hollow microneedle-based patch has been developed by Mohan *et al.* for alcohol detection in ISF.[78] A three-electrode system was adopted based on Pt and Ag wires embedded and fixed into the microneedle bores (**Figure 5b**). A multilayer modification approach was used to construct the amperometric alcohol biosensor, relying on an electrodeposited polyphenylene diamine (PPD) layer, coated with alcohol oxidase (AOx) in chitosan, and nafion

polymer. The combination of internal and external PPD and nafion polymer layers imparted a good selectivity and stability to the sensor, showed through in-vitro measurements of alcohol in artificial ISF solution. Ex vivo experiments using mice skin model substantiated the skin penetration ability and efficaciousness of the platform toward subcutaneous alcohol monitoring.

Microneedle patches have also been developed for detecting enzyme biomarkers, where Ciui et al. reported microneedle-based carbon paste electrodes to monitor the enzyme tyrosinase (**Figure 5c**).[111] Tyrosinase is involved in melanin synthesis and its overexpression and accumulation in skin cells can lead to the formation of skin melanoma.[111] Catechol, as the enzyme-substrate, was coated over the surface of carbon paste-packed microneedle working electrodes. In the presence of enzyme, catechol was catalyzed to benzoquinone whose electro-reduction current at -0.25 V was measured amperometrically as the analytical signal (**Figure 5c**). The utility of the developed microneedle platform was confirmed in vitro in porcine skin tissues, while a flexible ultralight electronic board was used to wireless data collection, processing, and transmission.

In another report, Mishra *et al.* described a microneedle patch for the detection of toxic organophosphate (OP), chemical agents.[112] The sensor relied on the effective catalytic action of organophosphorus hydrolase (OPH) enzyme to cleave the single P-O bond in OP compounds coupled with the rapid SWV interrogation of the hydrolysis product, para nitrophenol (**Figure 5 d**). The OPH enzyme was immobilized onto the carbon paste-packed hollow microneedles along with a protective Nafion layer. Ex vivo tests using mice skin samples exposed to methyl paraoxon illustrated the promise of such a minimally-invasive analytical platform toward monitoring OP chemical threat agents in the intradermal space.

Figure 1. 5. Examples of the detection of other analytes using MN-based sensors. a) Solid conical tip-based microneedle system for the detection of potassium in ex vivo setting: **i**) schematic illustration of the sensor surfaces. **ii**) representative potentiometric analytical responses obtained from the doses dependent study. Reproduced with permission. [76] Copyright 2019, American Chemical Society. **b**) Cylindrical hollow cavity with a pyramid-shaped microneedle system for the detection of alcohol: **i**) schematic illustration of the probe development. **ii**) obtained dose-dependent responses. Reproduced with permission. [78] Copyright 2017, Elsevier Inc. **c**) Solid microneedle-based patch portable system for melanoma screening: **i**) microneedle patch assembly of the prototype with the bandage and portable analyzer. **ii**) the chronoamperometric analytical responses in the absence and presence of the melanoma cells. Reproduced with permission. [111] Copyright 2018, Wiley-VCH Verlag GmbH & Co. **d**) solid microneedle-based system for nerve agent detection: **i**) schematic illustration of the sensor probe and detection principle. **ii**) the image of a coin-sized prototype of a microneedle-based patch. **iii**) voltammetric responses obtained on the dose-dependent spike of the nerve agent. Reproduced with permission. [112] Copyright 2017, Royal Society of Chemistry. **e**) Solid microneedle patch-based sensor for the orthogonal detection of L-dopa: i) schematic illustration of the sensor patch and detection principle. **ii-iii**) analytical responses obtained from voltammetry and amperometry on the dose-dependent spikes. Reproduced with permission. [17] Copyright 2019, American Chemical Society. **f**) Polymeric solid microneedle-based system for the detection of drug in in vivo system. **i**) schematic representation of the developed sensor. **ii**) potentiometric analytical response obtained during the in vivo study. Reproduced with permission. [18,61] Copyright 2019, American Chemical Society and Elsevier. Abbreviations: Reference electrode (RE); Working electrode (WE); Counter electrode (CE); Platinum (Pt); Silver (Ag), polyphenylene diamine (PPD); Chitosan-alcohol oxidase (Chit-AOx); Tyrosinase (TYR); Catechol (CAT); Benzoquinone (BQ); Organophosphorus hydrolase (OPH); and Organophosphorus (OP).

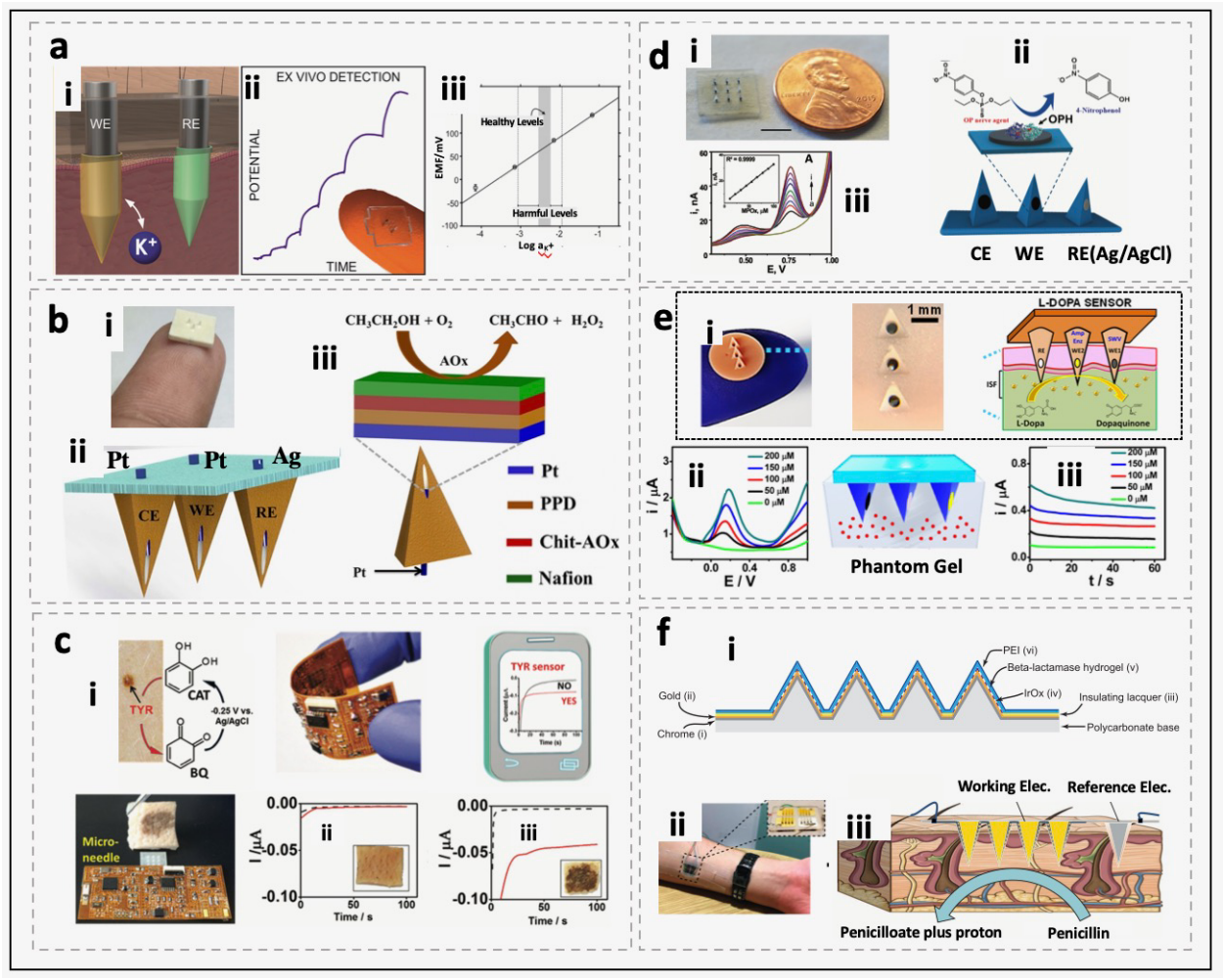
a
i
WE
RE
K+
ii
EX VIVO DETECTION
POTENTIAL
TIME
iii
Healthy Levels
Harmful Levels
EMF/mV
Log aK+
b
i
ii
Pt
Pt
Ag
CE
WE
RE
iii
CH3CH2OH + O2
CH3CHO + H2O2
AOx
Pt
PPD
Chit-AOx
Nafion
c
i
TYR
CAT
BQ
-0.25 V vs. Ag/AgCl
TYR sensor
NO
YES
Micro-needle
ii
iii
I /µA
Time / s
d
i
ii
OPH
4-Nitrophenol
CE
WE
RE(Ag/AgCl)
iii
i, nA
E, V
e
i
1 mm
L-DOPA SENSOR
ISF
L-Dopa
Dopaquinone
ii
iii
200 µM
150 µM
100 µM
50 µM
0 µM
i / µA
E / V
t / s
Phantom Gel
f
i
PEI (vi)
Beta-lactamase hydrogel (v)
IrOx (iv)
Insulating lacquer (iii)
Polycarbonate base
Gold (ii)
Chrome (i)
ii
iii
Working Elec.
Reference Elec.
Penicilloate plus proton
Penicillin

Microneedle sensors are particularly attractive for realizing personalized wearables for TDM applications, where drug dosing regimens are tailored based on the individual's metabolism to address intra- and interpatient variations that influence the drug pharmacokinetics.[60] In this regard, Goud *et al*. have described the first example of a microneedle patch to monitor L-dopa, the most commonly used drug to manage the symptoms of Parkinson's disease.[17] L-dopa has a short half-life in the body and a narrow therapeutic range which necessitates its tight monitoring to minimize the associated non-motor symptoms and motor complications. The described system employs a multimodal sensing platform relying on parallel simultaneous enzymatic and nonenzymatic transduction modes using independent microneedles on the same patch (**Figure 5e**). The enzymatic amperometric detection has been realized using tyrosinase-incorporated carbon paste-packed microneedles, while unmodified carbon paste was used for non-enzymatic SWV detection of L-dopa. Such real-time orthogonal detection system provides a built-in redundancy and different dimensions of information toward selective and sensitive tracking of L-dopa levels in the body. The potential wearable applications of the developed system were demonstrated in the skin mimicking phantom gel and in mice skin model; yet, critical and extensive clinical evaluation is essential before such a system can be deployed for managing Parkinson's disease patients.

Most recently, Rawson *et al.* demonstrated the first in-human evaluation of microneedle sensors toward TDM, where metallized solid microneedles were used for real-time tracking of ß-lactam antibiotics (**Figure 5f**).[61] While antibiotics are widely used for the treatment of infections, they need to be closely monitored as their overdosing can provoke severe toxicity and suboptimal dosing can result in antimicrobial resistance. In this work, phenoxymethylpenicillin was chosen as ß-lactam antibiotic based on its convenient oral administration route, well-documented safety profile, and narrow therapeutic range. With the fabrication and in-vitro validations of the sensor

being reported in previous research studies by the same group,[18,113] the recent work evaluated the potential of the microneedle sensor toward clinical applications on human subjects. The working electrode was constructed through electrodeposition of iridium oxide film on the gold-coated polycarbonate microneedle, followed by entrapping beta-lactamase enzyme in an optimized composition of a poly(ethylenimine)-based hydrogel layer. The reaction of penicillin derivative with the enzyme results in a change in the local pH and thus in the open circuit potential, which is measured by the underlying iridium oxide layer. 10 volunteers participated in a 6 hours long study while subjected to 5 doses of phenoxymethylpenicillin (500 mg). Each subject wore two microneedle patches, with one microneedle without the enzyme serving as the control to correct for any time-dependent pH changes which were not related to the analyte. The results from the microneedle were compared with the parallel data obtained with venous blood extracted by a cannula and the extracellular fluid (ECF) data from a microdialysis tube inserted in the tissue near the microneedle patch. The pharmacokinetic profiles obtained on the microneedle sensor showed a close correlation with those from blood and ECF, indicating the potential applicability of the developed system toward future minimally invasive TDM practices.

While the above-mentioned studies have substantially expanded the scope of microneedle-based sensors to new important analytes, they involved primarily ex-vivo assays of spiked artificial ISF. Future efforts should aim at extensive in-vivo clinical tests and large scale validation to unravel the potential of these microneedle sensors towards continuous on-body monitoring.

6. Multiplexed detection on Microneedle arrays

While the majority of wearable and point-of-care sensors have been developed for single-analyte determinations, current recent evidence supports the superiority of multianalyte

determinations toward collecting more comprehensive and accurate information regarding an individual's health status.[105,114–116] For example, using CGM-delivered glucose signals in insulin pumps leads to a slow and inadequate response to glycemic variability and hence, the inclusion of additional biomarkers (e.g. insulin, ketone bodies, cortisol, lactate, etc.) as inputs of control algorithms can effectively balance the effects of delivered insulin with those of other hormones that contribute to glucose metabolism.[105,117–119]

By providing spatially-resolved microelectrodes on a small array, microneedles can potentially support simultaneous, multiplexed detection of a panel of biomarkers. The first example of microneedle-based multiplexed sensing of glucose, lactate, and pH was demonstrated by Miller *et al.* to characterize the metabolic acidosis (**Figure 6a**).[58] An array of hollow microneedle array was aligned with the microwells created on a flexible flat cable. The microneedle manufacture was implemented by the dynamic light micro-stereolithography system, with its design defined using computer-aided design software. **Figure 6a** shows the schematic representation of the microneedle-electrode assembly. The microwells, each packed by a tailored carbon paste formulation, provided individually addressable electrodes to enable multiplexed detection of glucose, lactate, and pH. The application of a cell-resistant coating (Lipidure) was also reported to inhibit macrophage adhesion and thus, to provide prolonged operational stability of the system in-vivo.

In another study, Gao *et al.* reported a flexible microneedle array for multiplexed detection of glucose, uric acid, and cholesterol (**Figure 6b**).[120] Solid microneedle electrodes were created on a flexible polyimide substrate by using magnetorheological drawing lithography and sputter coating of the microneedles with Ti/Au thin films. This was followed by electrodepositing polyaniline and Pt nanoparticles and finally, by the biofunctionalization of spatially-resolved

microneedles with the respective oxidase enzymes. The flexible microneedle-based biosensor array was coupled to a home-made multi-channel portable electrochemical analyzer and in connection to external reference and counter electrodes and was used for simultaneous detection of the three biomarkers in their physiological ranges at an applied potential of 0.425 V *vs*. Ag/AgCl.

In a recent work, Teymourian *et al.* expanded the scope of biocatalytic systems used in microneedle sensors to the NAD-dependent dehydrogenase enzymes.[75] NAD-dependent dehydrogenases constitute the largest group of redox enzymes and relate to many important substrates.[75] As they do not suffer from the 'oxygen-deficiency' issue of oxidase enzymes, dehydrogenases can offer attractive biocatalytic systems toward continuous monitoring of a wide variety of substrates. However, their use in continuous monitoring wearables is quite challenging, mainly due to their need to a stable confinement strategy of the small-size NAD^+ cofactor biomolecule and the large overpotential and strong fouling effects related to the NADH oxidation. Such key challenges were addressed through a judicious integration of different biosensor components toward developing microneedle-based continuous ketone bodies monitoring (CKM) system. ß-hydroxybutyrate (HB), as the most important index of ketone bodies, is a marker for diabetic acidosis/ketoacidosis which is a severe complication of diabetes with potentially fatal consequences, can be detected through recognition by an immobilized ß-hydroxybutyrate dehydrogenase (HBD). The HB biosensor was based on an ionic liquid (IL)-carbon paste transducer electrode incorporated with the phenanthroline dione (PD) mediator, followed by a mixed HBD/NAD^+ layer, glutaraldehyde (GA) cross-linking, and further coating with chitosan (Chit) and polyvinyl chloride (PVC) as outer polymer layers (**Figure 6c**). The HB biosensor enabled low potential HB detection (at 0 V *vs*. integrated Ag/AgCl electrode); the immobilization

of GOx and LOx onto neighboring microneedle electrodes of the array offered simultaneous HB/glucose/lacate monitoring toward a tight glycemic control.

Mishra *et al.* described recently a wearable microneedle sensor array for continuous monitoring of fentanyl opioid (OPi) molecule and organophosphate (OP) nerve agents on a single patch platform.[87] The multiplexed OPi/OP sensor was realized based on a multimodal approach using unmodified and OPH enzyme-modified carbon paste microneedle electrodes for SWV detection of the fentanyl and nerve agent targets, respectively (**Figure 6d**). Such a multiplexed transdermal sensing device, capable of distinguishing between episodes of opioid overdose and nerve agent poisoning, can be very advantageous toward a timely life-saving medical intervention to protect the soldiers and civilians.

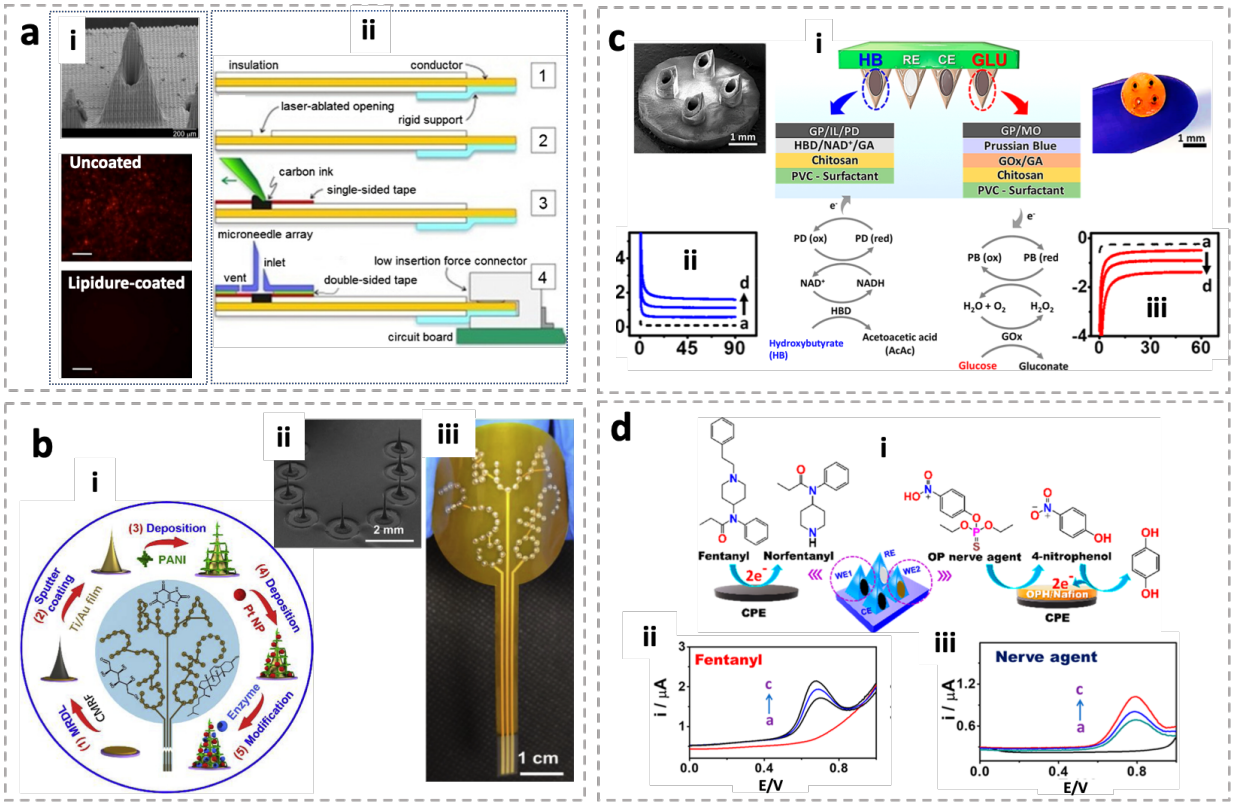

Figure 1.6. Examples of the multiplexed detection using microneedle-based sensors. a) Hollow microneedle array-based system for the multiplexed detection of pH, glucose, and lactate. **i**) Scanning electron microscopy (SEM) image of a single microneedle. Fluorescence images showing the macrophage adhesion experiments on the uncoated and Lipidure-coated microneedles at 24 hr post seeding (200 mm scale bar). **ii**) Schematic of microneedle-array assembly. Reproduced with permission. [58] Copyright 2012, Elsevier. **b)** Solid microneedle-based patch for multiplexed detection of glucose, uric acid and cholesterol. **i**) schematic illustration of microneedle sensors fabrication. **ii**) SEM image of the Ti/Au sputtered microneedles. iii) SEM micrograph showing the individual glucose, uric acid, and cholesterol sensors on a flexible polyimide substrate. Reproduced with permission. [120] Copyright 2019, Elsevier. **c)** Hollow microneedle-based sensing array for simultaneous detection of ketone bodies and glucose. **i**) SEM micrograph of the microneedle patch and the schematic illustration of the multilayer surface architectures used to prepare ß-hydroxybutyrate (HB) and glucose microneedle sensors. **ii, iii**) Chronoamperometric curves for increasing concentrations of HB (blue curves, 2-6 mM) and glucose (red curves, 2-6 mM). Reproduced with permission. [75] Copyright 2020, American Chemical Society. **d)** Multiplexed microneedle detection of the fentanyl opioid drug and an organophosphate nerve agent. **i**) Schematic illustration of the drug/nerve-agent sensor patch, showing the electrochemical detection principle of such multiplexed sensing. **ii, iii**) SWV response for increasing concentrations of fentanyl and methyl paraoxon organophosphate agent (50, 100, and 150 mM) carried out in a skin-mimicking 1% agarose gel. Reproduced with permission. [87] American Chemical Society. Abbreviations: Magnetorheological drawing lithography (MRDL); Polyaniline (PANI); Platinum nanoparticles (PtNPs); Reference electrode (RE); Counter electrode (CE); ß-hydroxybutyrate (HB); Glucose (GLU); Graphite powder (GP); Ionoc liquid (IL); Phenanthroline dione (PD) β-hydroxybutyrate dehydrogenase (HBD); Nicotinamide adenine dinucleotide (NAD); Glutaraldehyde (GA); Polyvinyl chloride (PVC); Mineral oil (MO); Glucose oxidase (GOx); and Carbon paste electrode (CPE).

7. Conclusion – Future prospects and challenges

The rapidly rising demands in the healthcare sector for wearable monitoring technologies have substantially intensified the efforts across academic and industrial communities to meet these needs. While the market for wearable devices of vital signs monitoring is continuing to expand, the most recent focus has been directed toward developing medical wearables capable of monitoring molecular indicators. These advances in microneedle sensor arrays have been facilitated by modern microfabrication techniques, available in the semiconductor industry. Microneedle-based transdermal electrochemical sensors are in a prime position to be a key player in the future of medical wearables, with considerable potential to transform the patient outcomes. Such microneedle patches are painlessly inserted to the layer underneath the skin to contact with the ISF, where the integrated electrochemical sensors can constantly collect clinically relevant real-time information. The potential of microneedle-based biosensors is huge; yet, there are challenges that need to be addressed before such sensors can be deployed in routine clinical practice. Here, we will briefly discuss the current picture and future prospects as well as the remaining unmet challenges of this rapidly evolving field.

Current picture and future prospects – The ISF is known to be a rich source of biomarkers, with a composition mirroring that of blood. In particular, the systematic studies on human subjects conducted over the last three years by several research groups further confirmed the unique potential of dermal ISF to supplant the current blood-based gold standard body fluid.[5–9] A promising example is the recent work of Samant *et al.*,[5] where microneedles were applied to the skin of 50 human subjects to form shallow micropores across the skin, followed by mild suction to draw the ISF. The LC-MS analysis of the extracted ISF showed around 10,000 compounds, most of which were also detected in the blood. Interestingly, 12% of molecular species were only

detected in the ISF and some others were found in larger concentrations than those in blood. Such studies can largely expand our knowledge and understanding of the diversity of chemical markers and identifying the diagnostic potential of the ISF biofluid toward routine clinical monitoring.

Microneedle sensors have recently seen atremendous progress, with microneedle-based CGM biosensor serving as the most advanced corner of research in this area. In comparison to well-established needle-type CGMs, microneedles offer several advantages and are anticipated to compete with needle-type CGMs in the next few years. Unlike current CGMs, microneedles are minimally-invasive, can provide multiple, redundant measurements across the sensor array which enhance the accuracy and detects the outliers, are easily adaptable to multiplexed sensing of other diabetes-related biomarkers, and can be more cost-effective in connection to common scalable manufacturing techniques. Microneedle CGM devices are currently under development by several start-up companies. San Diego-based Biolinq announced in June 2020 its first successful human trial with results showing promising correlation and no lag time compared to the venous blood. Caura (London, UK) is currently working on its microneedle technology to simultaneously monitor glucose and lactate along with the heart rate. Melbourne-based Nutromics (Australia) has started working on a personalized nutrition microneedle-based smart patch to detect analytes, such as glucose for diabetes people. We anticipate to see the first generations of such devices reach the market in the next three years.

Multiplexed monitoring can be readily achieved on microneedles using several spatially resolved individually addressable needle electrodes on a single patch. This represents a major and distinct advantage of microneedles as compared to single-analyte sensing devices; multiplexed monitoring can provide a holistic view of the metabolism and thus, leading to more advanced comprehensive patient monitoring.[121] This possibility has been well demonstrated in several in-

vitro studies over the last three years.[75,87,120] Looking forward, we expect to see microneedle-empowered multiplexed sensing devices to be available in the near future.

Microneedles also hold enormous potential to be employed in future TDM wearables. Some important examples have already been demonstrated toward antimicrobial dosing for infection treatment[61] and monitoring of L-dopa for Parkinson's disease management[17]. Such drugs have a narrow therapeutic range and a short pharmacokinetic profile. In addition, their pharmacodynamics change with disease progression, and thus, they need to be closely monitored during short time intervals to prevent over-or under-dosing courses. Microneedle-based transdermal sensors represent an attractive option toward high-frequency monitoring of therapeutics. The recently conducted human trial on microneedle-based antibiotics monitoring, although still limited, has been a major leap forward toward afurther extensive clinical analysis of microneedle patches for TDM applications and their commercialization in a foreseeable future.[61] Microneedle electrochemical sensors, however, offered limited use for continuous monitoring of non-electroactive proteins, hormones, and genes. This area lags behind mostly because of the complex multistep nature of their current standard transduction methods and the lack of suitable sensing chemistry capable of regenerating the recognition sites. While it is not the topic of this review paper, there have been several advances towards applying microneedles for ISF extraction coupled with on-chip sensing and it is anticipated to observe these devices in the next years. An example is a recent report on the use of a hollow microneedle test strip to extract the ISF and transport it to a colorimetric lateral flow immunoassay to detect malaria infection in less than 20 min.[122] Such ISF-based rapid point-of-care testing can be highly valuable in low resource settings in developing countries where the access to advanced clinical laboratories is limited.

Microneedle sensors can play their part in the other half of a closed-loop device connected to an integrated array of drug-loaded microneedles. The capability of microneedles for delivering medications is well established, and many microneedle-based drug-delivery patches are already available or are in clinical trials toward commercialization.[123,124] Here, the continuous analytical data from the sensor component can be transmitted to a control algorithm, which, upon reaching a preset 'high' or 'low' threshold, can trigger the drug release on the delivery component. Such on-demand delivery on microneedle patches has recently been described in several innovative examples. A multiplexed drug delivery microneedle was demonstrated through electrochemically-controlled polypyrrole-based 'open/close' nanoactuators.[125] Most recently, a dual self-regulatory transdermal patch has been described to deliver insulin or glucagon to treat hyperglycemia and hypoglycemia, respectively, and thereby, to maintain normoglycemia during glucose fluctuations.[126] Such innovative responsive microneedle delivery strategies can be merged with advanced microneedle sensors on the same patch (or on neighboring epidermal patches) for creating a closed-loop 'Sense-Act' system which can provide personalized treatment regimens in response to the respective fluctuating concentrations of the molecular indicators.

Most current integrated microneedle sensing platforms rely on coupling the sensor array, the electronic interface, and a battery as a packed 'sandwich' assembly within an enclosure, on a small circular footprint of less than 10-15 mm diameter. We anticipate that significant advances in the area of low-power electronics, wireless communication, and self-powered biosensors will lead to fully-integrated, miniaturized battery-free microneedle-empowered electrochemical sensing devices in the foreseeable future.

Challenges – Aiming at continuous monitoring of analytes in the dermal space, an extremely important factor is achieving an efficient and reliable skin penetration and needle-tissue

interlocking of the microneedle. Achieving reliable skin penetration is challenging, especially regarding the elasticity of the skin, which results in a counteracting force to the penetration and thus, to a partial or incomplete piercing. Another complicating factor that needs to be considered is the variation in skin thickness originated from differences in age, gender, body mass index, and ethnicity of the wearer. However, it has been reported that reliable skin penetration could be realized through careful optimization of the microneedle geometrical parameters, including the height, tip radius, base diameter, needle density, and spacing, as these factors (along with the type of materials) determine the insertion and fracture forces.[63] These optimal microneedle arrays could be coupled with proper applicators to control the insertion force and ensure reliable skin insertion using a carefully defined velocity and angle.

Other technological challenges of microneedle sensors relate to reproducible insulation, sealing, and sensor modification protocols. While well-defined masking procedures are needed in order to define the electrode area, reliable modification of the microscale sensors with bioreagents and polymers could be achieved through precise liquid dispensers or via carefully controlled spray coating methods. Furthermore, a cost-effective method to sterilize the microneedles before their on-body operation is another challenge that needs to be addressed.

From the sensing chemistry point of view, one of the challenges that will need to be addressed is extending the operation of electrochemical microneedle sensors towards the continuous monitoring of major protein biomarkers, such as insulin, cortisol, and cytokines to name a few. Accordingly, there are critical needs to develop microneedle devices based on new detection principles to enable real-time, on-body monitoring of wide range of analytes. In this regard, aptamer-based electrochemical transduction represents a promising route toward realizing

this aim, although additional work is needed to make aptamer microneedle sensors reliable enough for routine clinical practice.[102,103,127]

Biofouling and foreign body response are other limiting issues that affect the long-term on-body operation of the sensors. While this issue can potentially be addressed through the application of fine tunable polymeric protective layers to exclude surface-active macromolecules, the minimally-invasive performance of the microneedle sensor results in minimal tissue trauma and inflammation and this may cause less intensive body response compared to the current CGMs or other implantable sensors. A fascinating approach to extend the long-term stability of the microneedle sensors could be achieved using several subarrays with various types/thicknesses of transient coatings to sequentially expose and activate each sensor array.[128] The post–sensor implantation foreign body inflammatory response also requires attention to the initial stabilization time of microneedle sensors, prior to the acquisition of the analytical data.

Realizing an ultrasensitive response essential for direct detection of trace (nanomolar) levels of many important target molecules (e.g., drugs) is another key issue. Add to this, the high required selectivity for the target analyte in the presence of many constituents which are structurally related to the analyte of interest or can undergo redox reactions in the desired potential window and thus, can lead to false negative or positive signals. Resolving sensitivity and selectivity issues should be addressed by custom designing the sensing chemistry toward the target analyte.

The final step would be critical evaluation of the sensor performance through gold standard analytical instruments and extensive validations in large populations to ensure high accuracy of the sensor. This is highly essential, in particular, for closed-loop 'sense-act' systems where a small variation may lead to a wrong dosing regimen, that could result in life-threatening issues to the

wearer. As a final consideration, we believe that the huge potential benefits of microneedle sensors will drive, in the near future, extensive multidisciplinary efforts to transform such devices from labs out onto the people's bodies, and eventually towards creating 'labs under the skin'.

Acknowledgement

In the thesis, **Chapter 1** is based, in part, on the material as it appears in Advanced Healthcare Materials, 2021, by Hazhir Teymourian, Farshad Tehrani, Kuldeep Mahato, in Advanced Healthcare Materials. The dissertation author was the primary co-investigator and co-author of this paper.

8. References

[1] H. Teymourian, A. Barfidokht, J. Wang, *Chem. Soc. Rev.* **2020**, *49*, 7671.

[2] H. Wiig, M. A. Swartz, *Physiol. Rev.* **2012**, *92*, 1005.

[3] L. Ventrelli, L. Marsilio Strambini, G. Barillaro, *Adv. Healthc. Mater.* **2015**, *4*, 2606.

[4] J. Heikenfeld, A. Jajack, B. Feldman, S. W. Granger, S. Gaitonde, G. Begtrup, B. A. Katchman, *Nat. Biotechnol.* **2019**, *37*, 407.

[5] P. P. Samant, M. M. Niedzwiecki, N. Raviele, V. Tran, J. Mena-Lapaix, D. I. Walker, E. I. Felner, D. P. Jones, G. W. Miller, M. R. Prausnitz, *Sci. Transl. Med.* **2020**, *12*, eaaw0285.

[6] C. Kolluru, M. Williams, J. Chae, M. R. Prausnitz, *Adv. Healthc. Mater.* **2019**, *8*, 1801262.

[7] M. M. Niedzwiecki, P. Samant, D. I. Walker, V. Tran, D. P. Jones, M. R. Prausnitz, G. W. Miller, *Anal. Chem.* **2018**, *90*, 3786.

[8] A. K. Nilsson, U. Sjöbom, K. Christenson, A. Hellström, *Lipids Health Dis.* **2019**, *18*, 164.

[9] B. Q. Tran, P. R. Miller, R. M. Taylor, G. Boyd, P. M. Mach, C. N. Rosenzweig, J. T. Baca, R. Polsky, T. Glaros, *J. Proteome Res.* **2018**, *17*, 479.

[10] P. R. Miller, R. M. Taylor, B. Q. Tran, G. Boyd, T. Glaros, V. H. Chavez, R. Krishnakumar, A. Sinha, K. Poorey, K. P. Williams, et al., *Commun. Biol.* **2018**, *1*, 173.

[11] U. Sjöbom, K. Christenson, A. Hellström, A. K. Nilsson, *Front. Immunol.* **2020**, *11*, 2869.

[12] P. Greenwald, *Br. Med. J.* **2002**, *324*, 714.

[13] I. Ilias, N. Nikitas, M. Theodorakopoulou, I. Dimopoulou, *Recent Pat. Endocr. Metab. Immune Drug Discov.* **2018**, *11*, 32.

[14] M. Venugopal, K. E. Feuvrel, D. Mongin, S. Bambot, M. Faupel, A. Panangadan, A. Talukder, R. Pidva, *IEEE Sens. J.* **2008**, *8*, 71.

[15] A. J. Bandodkar, W. Jia, C. Yardimci, X. Wang, J. Ramirez, J. Wang, *Anal. Chem.* **2015**, *87*, 394.

[16] A. Jina, M. J. Tierney, J. A. Tamada, S. McGill, S. Desai, B. Chua, A. Chang, M. Christiansen, *J. Diabetes Sci. Technol.* **2014**, *8*, 483.

[17] K. Y. Goud, C. Moonla, R. K. Mishra, C. Yu, R. Narayan, I. Litvan, J. Wang, *ACS Sensors* **2019**, *4*, 2196.

[18] S. A. N. Gowers, D. M. E. Freeman, T. M. Rawson, M. L. Rogers, R. C. Wilson, A. H. Holmes, A. E. Cass, D. O'Hare, *ACS Sensors* **2019**, *4*, 1072.

[19] L. Lipani, B. G. R. Dupont, F. Doungmene, F. Marken, R. M. Tyrrell, R. H. Guy, A. Ilie, *Nat. Nanotechnol.* **2018**, *13*, 504.

[20] C. Kolluru, M. Williams, J. S. Yeh, R. K. Noel, J. Knaack, M. R. Prausnitz, *Biomed. Microdevices* **2019**, *21*, 14.

[21] E. Waltz, *Nat. Biotechnol.* **2019**, *37*, 340.

[22] J. Madden, C. O'Mahony, M. Thompson, A. O'Riordan, P. Galvin, *Sens. Bio-Sensing Res.* **2020**, 100348.

[23] F. Tasca, C. Tortolini, P. Bollella, R. Antiochia, *Curr. Opin. Electrochem.* **2019**, *16*, 42.

[24] B. L. Zhang, X. P. Zhang, B. Z. Chen, W. M. Fei, Y. Cui, X. D. Guo, *Microchem. J.* **2021**, *162*, 105830.

[25] G. S. Liu, Y. Kong, Y. Wang, Y. Luo, X. Fan, X. Xie, B. R. Yang, M. X. Wu, *Biomaterials* **2020**, *232*, 119740.

[26] S. R. Chinnadayyala, K. D. Park, S. Cho, *ECS J. Solid State Sci. Technol.* **2018**, *7*, Q3159.

[27] M. Wang, L. Hu, C. Xu, *Lab Chip* **2017**, *17*, 1373.

[28] P. R. Miller, R. J. Narayan, R. Polsky, *J. Mater. Chem. B* **2016**, *4*, 1379.

[29] K. Takeuchi, B. Kim, *Nano Converg*. **2018**, *5*, 28.

[30] A. El-Laboudi, N. S. Oliver, A. Cass, D. Johnston, *Diabetes Technol. Ther*. **2013**, *15*, 101.

[31] S. Babity, M. Roohnikan, D. Brambilla, *Small* **2018**, *14*, 1803186.

[32] L. Xie, H. Zeng, J. Sun, W. Qian, *Micromachines* **2020**, *11*, 271.

[33] M. S. Gerstel, V. A. Place, *Drug Delivery Device*, **1976**, US3964482A.

[34] S. Henry, D. V. McAllister, M. G. Allen, M. R. Prausnitz, *J. Pharm. Sci*. **1998**, *87*, 922.

[35] M. A. Lopez-Ramirez, F. Soto, C. Wang, R. Rueda, S. Shukla, C. Silva-Lopez, D. Kupor, D. A. McBride, J. K. Pokorski, A. Nourhani, Joseph Wang, *Adv. Mater*. **2020**, *32*, 1905740.

[36] M. Qu, H.-J. Kim, X. Zhou, C. Wang, X. Jiang, J. Zhu, Y. Xue, P. Tebon, S. A. Sarabi, S. Ahadian, Ali Khademhoseseini., *Nanoscale* **2020**, *12*, 16724.

[37] K. Lee, Y. Xue, J. Lee, H.-J. Kim, Y. Liu, P. Tebon, E. Sarikhani, W. Sun, S. Zhang, R. Haghniaz, Ali Khademhosseini., *Adv. Funct. Mater*. **2020**, *30*, 2000086.

[38] M. R. Prausnitz, Y. Gomaa, W. Li, *Nat. Med*. **2019**, *25*, 1471.

[39] W. Li, J. Tang, R. N. Terry, S. Li, A. Brunie, R. L. Callahan, R. K. Noel, C. A. Rodríguez, S. P. Schwendeman, M. R. Prausnitz, *Sci. Adv*. **2019**, *5*, eaaw8145.

[40] P. M. Frew, M. B. Paine, N. Rouphael, J. Schamel, Y. Chung, M. J. Mulligan, M. R. Prausnitz, *Vaccine* **2020**, *38*, 7175.

[41] F. Wang, X. Zhang, G. Chen, Y. Zhao, *Research* **2020**, *2020*, 2760594.

[42] X. Zhang, F. Wang, Y. Yu, G. Chen, L. Shang, L. Sun, Y. Zhao, *Sci. Bull*. **2019**, *64*, 1110.

[43] E. Caffarel-Salvador, S. Kim, V. Soares, R. Y. Tian, S. R. Stern, D. Minahan, R. Yona, X. Lu, F. R. Zakaria, J. Collins, Giovanni Traverso, *Sci. Adv*. **2021**, *7*, eabe2620.

[44] W. H. Smart, K. Subramanian, *Diabetes Technol. Ther*. **2000**, *2*, 549.

[45] H. J. G. E. Gardeniers, R. Luttge, E. J. W. Berenschot, M. J. de Boer, S. Y. Yeshurun, M. Hefetz, R. van-t Oever, A. van den Berg, *J. Microelectromechanical Syst*. **2003**, *12*, 855.

[46] E. V. Mukerjee, S. D. Collins, R. R. Isseroff, R. L. Smith, *Sensors Actuators A Phys*. **2004**, *114*, 267.

[47] S. R. Corrie, G. J. P. Fernando, M. L. Crichton, M. E. G. Brunck, C. D. Anderson, M. A.

F. Kendall, *Lab Chip* **2010**, *10*, 2655.

[48] D. A. Muller, S. R. Corrie, J. Coffey, P. R. Young, M. A. Kendall, *Anal. Chem.* **2012**, *84*, 3262.

[49] J. W. Coffey, S. R. Corrie, M. A. F. Kendall, *Biomaterials* **2018**, *170*, 49.

[50] X. Zhang, G. Chen, F. Bian, L. Cai, Y. Zhao, *Adv. Mater.* **2019**, *31*, 1902825.

[51] Z. Wang, J. Luan, A. Seth, L. Liu, M. You, P. Gupta, P. Rathi, Y. Wang, S. Cao, Q. Jiang, Srikanth Singamaneni, *Nat. Biomed. Eng.* **2021**, *5*, 64.

[52] D. Al Sulaiman, J. Y. H. Chang, N. R. Bennett, H. Topouzi, C. A. Higgins, D. J. Irvine, S. Ladame, *ACS Nano* **2019**, *13*, 9620.

[53] B. Yang, X. Fang, J. Kong, *ACS Appl. Mater. Interfaces* **2019**, *11*, 38448.

[54] A. V. Romanyuk, V. N. Zvezdin, P. Samant, M. I. Grenader, M. Zemlyanova, M. R. Prausnitz, *Anal. Chem.* **2014**, *86*, 10520.

[55] H. Chang, M. Zheng, X. Yu, A. Than, R. Z. Seeni, R. Kang, J. Tian, D. P. Khanh, L. Liu, P. Chen, Chenjie Xu, *Adv. Mater.* **2017**, *29*, 1702243.

[56] J. R. Windmiller, G. Valdés-Ramírez, N. Zhou, M. Zhou, P. R. Miller, C. Jin, S. M. Brozik, R. Polsky, E. Katz, R. Narayan, Joseph Wang., *Electroanalysis* **2011**, *23*, 2302.

[57] J. R. Windmiller, N. Zhou, M.-C. Chuang, G. Valdés-Ramírez, P. Santhosh, P. R. Miller, R. Narayan, J. Wang, *Analyst* **2011**, *136*, 1846.

[58] P. R. Miller, S. A. Skoog, T. L. Edwards, D. M. Lopez, D. R. Wheeler, D. C. Arango, X. Xiao, S. M. Brozik, J. Wang, R. Polsky, Roger J Narayan, *Talanta* **2012**, *88*, 739.

[59] G. Valdés-Ramírez, Y.-C. Li, J. Kim, W. Jia, A. J. Bandodkar, R. Nuñez-Flores, P. R. Miller, S.-Y. Wu, R. Narayan, J. R. Windmiller, Joseph Wang, *Electrochem. commun.* **2014**, *47*, 58.

[60] H. Teymourian, M. Parrilla, J. R. Sempionatto, N. F. Montiel, A. Barfidokht, R. Van Echelpoel, K. De Wael, J. Wang, *ACS Sensors* **2020**, *5*, 2679.

[61] T. M. Rawson, S. A. N. Gowers, D. M. E. Freeman, R. C. Wilson, S. Sharma, M. Gilchrist, A. MacGowan, A. Lovering, M. Bayliss, M. Kyriakides, Alison H Holmes. *Lancet Digit. Heal.* **2019**, *1*, e335.

[62] E. Larrañeta, R. E. M. Lutton, A. D. Woolfson, R. F. Donnelly, *Mater. Sci. Eng. R Reports* **2016**, *104*, 1.

[63] R. F. Donnelly, T. R. Raj Singh, D. I. . Morrow, A. D. Woolfson, *Microneedle-Mediated*

Transdermal Intradermal Drug Deliv. **2012**, 20.

[64] H. Kathuria, J. S. Kochhar, M. H. M. Fong, M. Hashimoto, C. Iliescu, H. Yu, L. Kang, *J. Vis. Exp.* **2015**, *2015*, 52914.

[65] B. Ma, S. Liu, Z. Gan, G. Liu, X. Cai, H. Zhang, Z. Yang, *Microfluid. Nanofluidics* **2006**, *2*, 417.

[66] A. Rodriguez, D. Molinero, E. Valera, T. Trifonov, L. F. Marsal, J. Pallarès, R. Alcubilla, *Sensors Actuators B Chem.* **2005**, *109*, 135.

[67] S.-J. Paik, S. Byun, J.-M. Lim, Y. Park, A. Lee, S. Chung, J. Chang, K. Chun, D. "Dan" Cho, *Sensors Actuators A Phys.* **2004**, *114*, 276.

[68] S. D. Gittard, A. Ovsianikov, N. A. Monteiro-Riviere, J. Lusk, P. Morel, P. Minghetti, C. Lenardi, B. N. Chichkov, R. J. Narayan, *J. Diabetes Sci. Technol.* **2009**, *3*, 304.

[69] N. Reddy Mogusala, V. Ratnam Devadasu, R. Kumar Venisetty, *Am. J. Drug Deliv. Ther.* **2015**.

[70] S. Bystrova, R. Luttge, *Microelectron. Eng.* **2011**, *88*, 1681.

[71] K. Lee, H. C. Lee, D.-S. Lee, H. Jung, *Adv. Mater.* **2010**, *22*, 483.

[72] K. Lee, H. Jung, *Biomaterials* **2012**, *33*, 7309.

[73] Z. Chen, L. Ren, J. Li, L. Yao, Y. Chen, B. Liu, L. Jiang, *Acta Biomater.* **2018**, *65*, 283.

[74] E. García-López, H. R. Siller, C. A. Rodríguez, *Procedia Manuf.* **2018**, *26*, 117.

[75] H. Teymourian, C. Moonla, F. Tehrani, E. Vargas, R. Aghavali, A. Barfidokht, T. Tangkuaram, P. P. Mercier, E. Dassau, J. Wang, *Anal. Chem.* **2020**, *92*, 2291.

[76] M. Parrilla, M. Cuartero, S. Padrell Sánchez, M. Rajabi, N. Roxhed, F. Niklaus, G. A. Crespo, *Anal. Chem.* **2019**, *91*, 1578.

[77] F. Ribet, G. Stemme, N. Roxhed, *Biomed. Microdevices* **2018**, *20*, 101.

[78] A. M. V. Mohan, J. R. Windmiller, R. K. Mishra, J. Wang, *Biosens. Bioelectron.* **2017**, *91*, 574.

[79] F. Jacobs, Paul, *J. Manuf. Syst.* **1993**, *12*, 430.

[80] B. L. Douglass, C. R. Douglass, *Fused Filament Fabrication System and Method*, **2014**, US9469071B2.

[81] D. K. Patel, A. H. Sakhaei, M. Layani, B. Zhang, Q. Ge, S. Magdassi, *Adv. Mater.* **2017**, *29*, 1606000.

[82] S.-H. Park, D.-Y. Yang, K.-S. Lee, *Laser Photon. Rev.* **2009**, *3*, 1.

[83] J. S. Kochhar, T. C. Quek, W. J. Soon, J. Choi, S. Zou, L. Kang, *J. Pharm. Sci.* **2013**, *102*, 4100.

[84] B. Ahn, *Int. J. Control. Autom. Syst.* **2020**, *18*, 143.

[85] N. J. Ronkainen, H. B. Halsall, W. R. Heineman, *Chem. Soc. Rev.* **2010**, *39*, 1747.

[86] J. Wang, *Analytical Electrochemistry, Third Edition*, John Wiley & Sons, Inc., Hoboken, NJ, USA, **2006**.

[87] R. K. Mishra, K. Y. Goud, Z. Li, C. Moonla, M. A. Mohamed, F. Tehrani, H. Teymourian, J. Wang, *J. Am. Chem. Soc.* **2020**, *142*, 5991.

[88] S. J. Lee, H. S. Yoon, X. Xuan, J. Y. Park, S. J. Paik, M. G. Allen, *Sensors Actuators, B Chem.* **2016**, DOI 10.1016/j.snb.2015.08.013.

[89] Y. Yoon, G. Lee, K. Yoo, J.-B. Lee, *Sensors* **2013**, *13*, 16672.

[90] Y. Shao, Y. Ying, J. Ping, *Chem. Soc. Rev.* **2020**, DOI 10.1039/c9cs00587k.

[91] J. Hu, A. Stein, P. Bühlmann, *TrAC - Trends Anal. Chem.* **2016**, *76*, 102.

[92] J. Min, J. R. Sempionatto, H. Teymourian, J. Wang, W. Gao, *Biosens. Bioelectron.* **2020**, 112750.

[93] J. Kuhlmann, L. C. Dzugan, W. R. Heineman, *Electroanalysis* **2012**, *24*, 1732.

[94] J. Wang, *Chem. Rev.* **2007**, *108*, 814.

[95] S. Sharma, A. El-Laboudi, M. Reddy, N. Jugnee, S. Sivasubramaniyam, M. El Sharkawy, P. Georgiou, D. Johnston, N. Oliver, A. E. G. Cass, *Anal. Methods* **2018**, *10*, 2088.

[96] P. Bollella, S. Sharma, A. E. G. Cass, R. Antiochia, *Biosens. Bioelectron.* **2019**, *123*, 152.

[97] S. Sharma, A. Saeed, C. Johnson, N. Gadegaard, A. E. Cass, *Sens. Bio-Sensing Res.* **2017**, *13*, 104.

[98] J. Tu, R. M. Torrente-Rodríguez, M. Wang, W. Gao, *Adv. Funct. Mater.* **2020**, *30*, 1906713.

[99] D. Kinnamon, R. Ghanta, K.-C. Lin, S. Muthukumar, S. Prasad, *Sci. Rep.* **2017**, *7*, 13312.

[100] X. Luo, M. Xu, C. Freeman, T. James, J. J. Davis, *Anal. Chem.* **2013**, *85*, 4129.

[101] S. Khezrian, A. Salimi, H. Teymourian, R. Hallaj, *Biosens. Bioelectron.* **2013**, *43*, 218.

[102] N. Arroyo-Currás, P. Dauphin-Ducharme, K. Scida, J. L. Chávez, *Anal. Methods* **2020**, *12*, 1288.

[103] N. Arroyo-Currás, G. Ortega, D. A. Copp, K. L. Ploense, Z. A. Plaxco, T. E. Kippin, J. P. Hespanha, K. W. Plaxco, *ACS Pharmacol. Transl. Sci.* **2018**, *1*, 110.

[104] P. M. Wang, M. Cornwell, M. R. Prausnitz, *Diabetes Technol. Ther.* **2005**, *7*, 131.

[105] K. L. Wolkowicz, E. M. Aiello, E. Vargas, H. Teymourian, F. Tehrani, J. Wang, J. E. Pinsker, F. J. Doyle III, M.-E. Patti, L. M. Laffel, Chenjie Xu, *Bioeng. Transl. Med.* **2020**, *n/a*, e10201.

[106] S. Sharma, Z. Huang, M. Rogers, M. Boutelle, A. E. G. Cass, *Anal. Bioanal. Chem.* **2016**, *408*, 8427.

[107] P. Bollella, S. Sharma, A. E. G. Cass, F. Tasca, R. Antiochia, *Catalysts* **2019**, *9*, 580.

[108] E. Katz, A. F. Bückmann, I. Willner, *J. Am. Chem. Soc.* **2001**, *123*, 10752.

[109] E. Katz, *Implant. Bioelectron.* **2014**, 363.

[110] P. R. Miller, X. Xiao, I. Brener, D. B. Burckel, R. Narayan, R. Polsky, *Adv. Healthc. Mater.* **2014**, *3*, 876.

[111] B. Ciui, A. Martin, R. K. Mishra, B. Brunetti, T. Nakagawa, T. J. Dawkins, M. Lyu, C. Cristea, R. Sandulescu, J. Wang, *Adv. Healthc. Mater.* **2018**, *7*, 1701264.

[112] R. K. Mishra, A. M. Vinu Mohan, F. Soto, R. Chrostowski, J. Wang, *Analyst* **2017**, *142*, 918.

[113] T. M. Rawson, S. Sharma, P. Georgiou, A. Holmes, A. Cass, D. O'Hare, *Electrochem. commun.* **2017**, *82*, 1.

[114] E. C. Lee, M. S. Fragala, S. A. Kavouras, R. M. Queen, J. L. Pryor, D. J. Casa, *J. strength Cond. Res.* **2017**, *31*, 2920.

[115] P. Yáñez-Sedeño, S. Campuzano, J. M. Pingarrón, *Sensors* **2017**, *17*, 965.

[116] D. Brennan, P. Galvin, *MRS Commun.* **2018**, *8*, 627.

[117] E. Vargas, H. Teymourian, F. Tehrani, E. Eksin, E. Sánchez-Tirado, P. Warren, A. Erdem, E. Dassau, J. Wang, *Angew. Chemie - Int. Ed.* **2019**, *58*, 6376.

[118] R. Soffe, V. Nock, J. G. Chase, *ACS Sensors* **2019**, *4*, 3.

[119] J. Kim, J. R. Sempionatto, S. Imani, M. C. Hartel, A. Barfidokht, G. Tang, A. S. Campbell, P. P. Mercier, J. Wang, *Adv. Sci.* **2018**, *5*, 1800880.

[120] J. Gao, W. Huang, Z. Chen, C. Yi, L. Jiang, *Sensors Actuators, B Chem.* **2019**, *287*, 102.

[121] M. Kastellorizios, D. J. Burgess, *Sci. Rep.* **2015**, *5*, 10603.

[122] X. Jiang, P. B. Lillehoj, *Microsystems Nanoeng.* **2020**, *6*, 96.

[123] A. F. Moreira, C. F. Rodrigues, T. A. Jacinto, S. P. Miguel, E. C. Costa, I. J. Correia, *Pharmacol. Res.* **2019**, *148*, 104438.

[124] S. Duarah, M. Sharma, J. Wen, *Eur. J. Pharm. Biopharm.* **2019**, *136*, 48.

[125] G. Valdés-Ramírez, J. R. Windmiller, J. C. Claussen, A. G. Martinez, F. Kuralay, M. Zhou, N. Zhou, R. Polsky, P. R. Miller, R. Narayan, Lutz Mädler., *Sensors Actuators, B Chem.* **2012**, *161*, 1018.

[126] Z. Wang, J. Wang, H. Li, J. Yu, G. Chen, A. R. Kahkoska, V. Wu, Y. Zeng, D. Wen, J. R. Miedema, Zhen Gu, *Proc. Natl. Acad. Sci.* **2020**, *117*, 29512 LP.

[127] C. Parolo, A. Idili, G. Ortega, A. Csordas, A. Hsu, N. Arroyo-Currás, Q. Yang, B. S. Ferguson, J. Wang, K. W. Plaxco, *ACS Sensors* **2020**, *5*, 1877.

[128] V. Ruiz-Valdepeñas Montiel, J. R. Sempionatto, B. Esteban-Fernández de Ávila, A. Whitworth, S. Campuzano, J. M. Pingarrón, J. Wang, *J. Am. Chem. Soc.* **2018**, *140*, 14050.

Chapter 2. An Integrated Microneedle Sensor Platform

A Non-Intrusive Lab-Under-the-Skin: *Continuous Monitoring of Multiple Interstitial Fluid Biomarkers via a Fully Integrated Wearable Microneedle Platform*

1. Introduction.

Wearable sensors capable of monitoring biochemical markers are poised to help enable a new revolution in personalized healthcare, telehealth, and early disease diagnosis[1,2]. Among potential biomolecular sampling biofluids accessible via wearable sensors, interstitial fluid (ISF) has the closest composition to the blood, with temporal profiles of most analytes approaching those observed in blood[3–6]. In addition, direct ISF measurements are not affected by major issues common to other biofluids such as long lag times, variable secretion rates, sample contamination and dilution, and most importantly limited correlation, all of which greatly limit the sensor's clinical utility[3,7–10]. Microneedle (MN)-based sensing technologies provide pain-free, and non-intrusive continuous access to constantly revitalizing ISF. Here, we present the first demonstration of a fully integrated non-intrusive wearable sensor platform, based on a biocompatible array of MNs fabricated via our newly developed advanced micro-machining technique, optimized for real-time, continuous, and multiplexed biomolecular measurements on freely behaving human subjects. Our work addresses multifaceted challenges in the areas of system integration, fabrication, packaging, biocompatibility and sterilization, skin penetration, sensitivity and stability, and low-power yet real-time biosensing in an inexpensive manner. The fully integrated sensor array, comprised of two components of a reusable electronics and a disposable sensor, shows remarkable

ability in tracking the dynamic profiles of key metabolites (i.e., lactate, glucose, and alcohol) during common daily activities via a small, wireless-enabled wearable, with results well correlated to gold-standard metrics. The multiplexed sensing potential of the platform is also demonstrated through simultaneous on-body monitoring of lactate-glucose and alcohol-glucose, along with the demonstration of a custom designed smartphone app for data capture and visualization. The developed system marks a major new milestone for continuous, real-time, and accurate monitoring of clinically relevant biomolecules, and presents a major leap forward for next-generation wearable health monitors.

By nature of being attached to the body, wearable sensors offer the ability to continuously monitor physiological parameters in real-time on freely behaving subjects, providing interesting new insights into human health and wellness not offered by spot measurements taken in the clinic or by point-of-care devices[1,2]. Merging wearable sensors with rapidly growing "omics" technologies, internet of things devices, and artificial intelligence, can potentially offer revolutionary advances in personalized healthcare, early disease detection, telemedicine/remote monitoring, personalized nutrition or wellness, or even detection of symptoms associated with COVID-19 or other viral infections[11–14]. However, most commercial wearables monitor only a handful of physical parameters, such as heart rate and motion, which offer only generic physiological insights[2]. To address this issue, recent efforts have shifted to wearable devices that can detect in real time molecular markers on the skin surface through electrochemical analysis[1,15–17]. State-of-the-art, non-invasive chemical sensor research has mainly revolved around epidermal sensors utilizing stimulated sweat[15,18–21] or extracted interstitial fluid (ISF)[22,23]. However, both these skin-worn sensors still face significant challenges, including how to continuously access to the biofluid (e.g., via exercise or electrical stimulation), fluctuating flow rates, varying parameters

(e.g., sweat pH, salinity, and temperature), sample mixing, carry-over, dilution, or contamination[3,7]. These challenges, along with the limited correlation of some sweat biomarkers to gold-standard blood assays,[8,9] and significant lag time[24], require considerable research efforts towards making these epidermal platforms clinically viable.

Instead of analyzing biochemical markers on the surface of the skin, analysis under the skin - directly in ISF - provides a well-established, high degree of correlation with blood for many biomarkers of interest[4–6]. In fact, continuous glucose monitors (CGMs), approved for use by the US Food and Drug Administration for diabetes management, sense glucose in ISF with excellent correlation to blood. However, current CGMs rely on invasive needle-based sensors, and are limited to measuring only a single analyte[25,26]. In contrast, microneedle (MN) technology, hailed recently by Scientific American and the World Economic Forum as the top emerging technology for shaping the future of healthcare[27], utilizes micron-sized needles that penetrate the skin by only a few hundred microns to offer a pain- and discomfort-free way of accessing ISF, obviating the need for 5-11 mm long needles common to CGMs [6,28]. In addition, the limited single-analyte sensing capability of current CGM devices is readily addressable in MN platforms by utilizing multiple individually-addressable spatially-isolated sensing electrodes on a single platform, which allows for significant new detection opporunities[29,30]. The micron-scale nature of the MN sensors allows for their application on multiple locations on the body, making it adaptable to different form factors such as rings, and epidermal patches. Despite the tremendous opportunities offered by MNs, the realization of their full potential for practical wearable chemical sensing has remained an unmet challenge, reflecting primarily the multidisciplinary nature of these challenges that calls for a holistic approach in reliably addressing them.

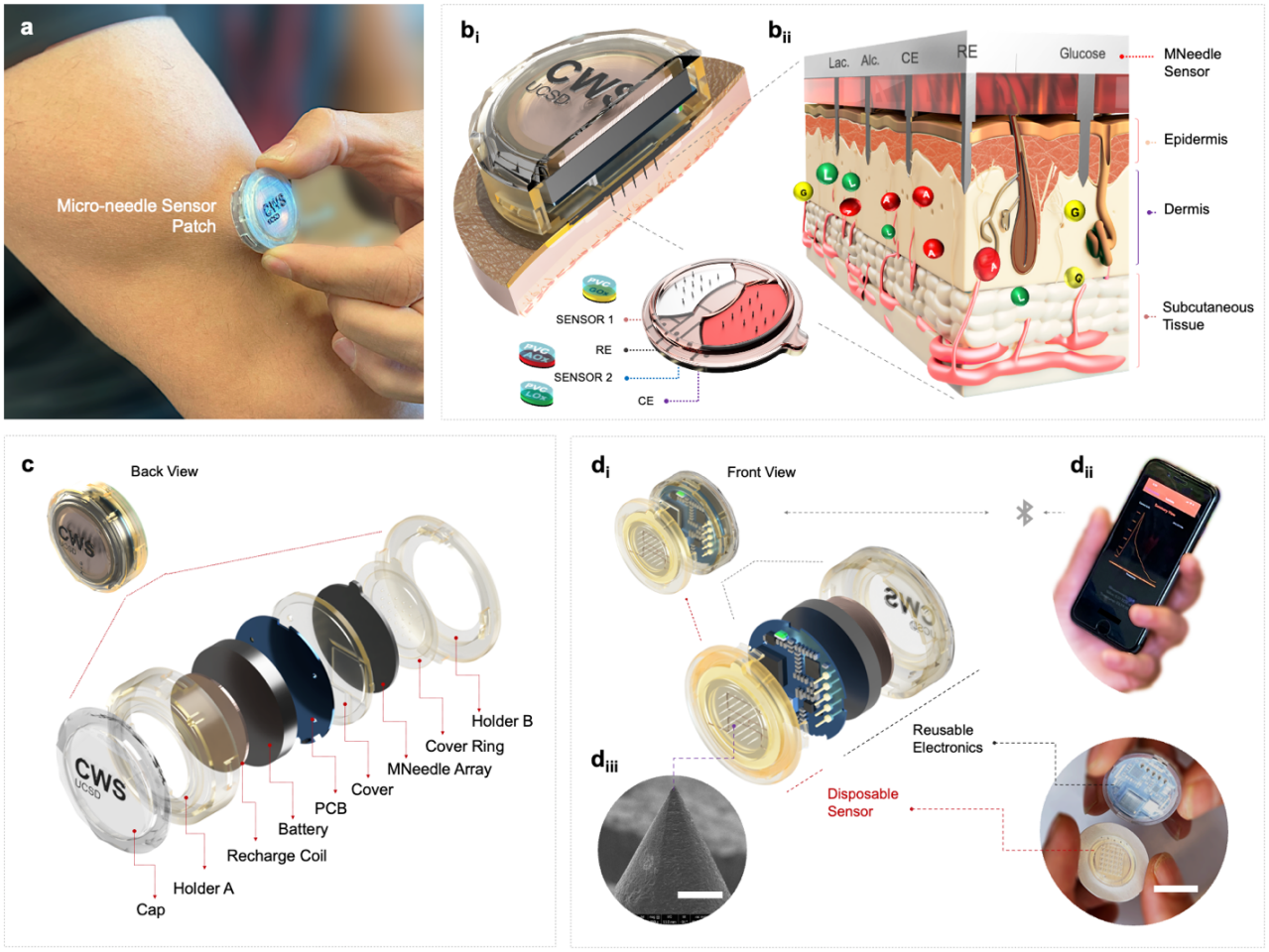

Figure 2. 1. Illustrations of the multiplexed microneedle wearable sensor system and subcomponents. **a.** The sensor patch adhered to the arm of a wearer. **b_i.** A cross-sectional illustration of the sensor patch with the Microneedles (MNs) pierced the skin to reach the epidermis, along with the schematics of the microelectrodes' configuration used in multiplexed sensor component. **b_{ii}.** Close-up cross-sectional illustration of the MN/skin interface (image is not to scale). **c.** Back view of the MN sensor patch with exploded view of the corresponding subcomponents. **d_i.** Front view of the MN sensor patch with the two primary components of disposable sensor array and reusable electronics (scale bar: 1.5 cm). **d_{ii}.** A smartphone held by a user and displaying sensing results in the App.'s summary view page. **d_{iii}.** Cone-like tip of an individual MN electrode by scanning electron microscopy (SEM) (scale bar: 75 μm).

Herein, we demonstrate, for the first time, a fully integrated, wirelessly operated MN platform for continuous monitoring of ISF biomarkers on human subjects (Figure 1a). The wearable system continuously collects rich molecular data to facilitate greater understanding of the body's response to daily activities. Real-time monitoring of ISF biomarkers (glucose, lactate,

and alcohol) is demonstrated both individually (single analyte) and simultaneously (multiplexed), with results well correlated to those of the corresponding gold standard (blood or breath) measurements over a prolonged duration. To achieve this, multifaceted challenges in the areas of system integration (sensor, electronics, firmware, and mobile app development), fabrication, skin penetration, and stable, accurate, and cross-talk-free biosensing, are successfully addressed through a holistic approach which is elaborated below. As illustrated in Figure 1, a fully integrated MN sensor system, composed of an array of multiple sensors and custom electronics was designed, fabricated, developed, and tested. The integrated system is made of nine distinct sub-components (Figure 1c and Extended Data Fig. 1), which are assembled into two primary components - "disposable sensor" and "reusable electronics" (Figure 1d_i) – to allow convenient replacement of the low-cost disposable sensor component according to its functional life. Molecular level electrochemical signals from the wearer's ISF are continuously and selectively gathered by the epidermis-inserted MN tips (Figure 1b_{ii} & d_{iii}), carried through the low-noise, reusable sensor-electronics physical interface acquired by the electronics, and wirelessly transmitted to the wearer's mobile app (Figure 1d_{ii}) for visualization and analysis. The entire operation is thus wirelessly controlled by the accompanying mobile application (app).

Figure 2$a_{i,ii}$ provides an overview of the electronics, which was designed for functionality, compactness, and low power operation. To acquire electrochemical signal data and subsequently transmit it, the electronic system utilizes two integrated circuits – an electrochemical analog front end (AFE) and a Bluetooth Low Energy (BLE) system-in-package (SiP). The AFE (Figure 2a_{iii}) provides the circuitry for multiplexing between up to 4 independent working electrodes, signal conditioning (amplification and filtering), and signal digitization, while the BLE SiP provides a low power microcontroller for processing the digitized signals, as well as a BLE radio and

embedded antenna for data transmission. Powering these components is accomplished by a lithium-polymer battery (through a voltage regulator), which is inductively charged through a wireless charging IC and charging coil (Extended Data Fig. 2). Additionally, power optimizations for the AFE and BLE SiP enable ~30 days of battery life while maintaining a relatively small battery size (Extended Data Fig. 3). Minimizing the number of necessary ICs to only four (2 for signal acquisition/transmission and 2 for voltage regulation / recharging), in addition to the power optimizations, allow for a compact design (Figure $2a_{iv}$). Manufacturing the electronics is intrinsically scalable, as the PCB and parts were fabricated and assembled using commercial processes. Further explanation of the electronics/app operation is provided in Methods and Extended Data Figs. 2-5.

The MN microelectrodes were fabricated by our newly developed, scalable, tremendously cost-effective, and highly reproducible micromachining method through transferring the 3D Computer-Aided Design (CAD) model of the optimized geometrical design to a Computer-Aided Manufacturing (CAD) file used for micro-computer numerical control (CNC) machining of the MN microelectrodes from a poly (methyl methacrylate) stock material (Extended Data Fig. 6). The dimensions, geometrical shape, and configuration of the microelectrodes (Fig. 2b, c) as well as the working-counter-reference electrode ratio (Extended Data Fig. 7) were judiciously optimized to achieve reliable mechanical robustness and maximized analytical performance while bio compatibly providing a pain-free skin penetration with a ≈5 μm MN tip diameter (Figure $2c_{i\text{-}vii}$). Additionally, time lapse images of the human subject's arm, taken after wearing the MN for 5 hours, showed no skin irritation or inflammation in the applied area (Extended Data Fig. 8). The biocompatible PMMA-based MN array along with the developed two-step sterilization protocol

ensured the safe deployment of the assembled MN sensor for in-vivo trials on human subjects (Extended Data Fig. 9).

Figure 2. 2. Electronics & Sensor Architecture. $\mathbf{a_i}$. Functional block diagram of the electronics' major components. $\mathbf{a_{ii}}$. Abridged functional block diagram of the AD5940 electrochemical AFE (recreated from the component's datasheet). $\mathbf{a_{iii}}$. Electronic system PCB connection to the battery (through a low-profile connector) and to the charging coil (through large solder pads). $\mathbf{a_{iv}}$. Major components labeled on the electronics. The electronic system interfaces MN sensor array through pins which insert into conductive holes on the sensor (sputter deposited metal within CNC milled holes). Mechanical guides at the base of the pins provide mechanical retention to the electronic system PCB. $\mathbf{b_i}$. Illustration of an individual MN with the corresponding dimensions. $\mathbf{b_{ii}}$. Side-view depiction of disposable component (A) and reusable electronics (B). $\mathbf{b_{iii}}$. Depiction of a multiplexed sensor with labeled microneedle groups as two separated working, counter and reference electrodes. $\mathbf{c_{i,ii}}$. SEM images showing side- and top-view of an individual MN tip (scale bar of 100 μm). $\mathbf{c_{iii}}$. SEM image of multiple MNs (scale bar of 500 μm). $\mathbf{c_{iv,v}}$. A batch of four micromachined MN arrays before after sputtering of thin film metals (scale bar: 2.5 cm and 2 cm, respectively). $\mathbf{c_{vi,vii}}$. Assembled MN-cover ring for single and multiple sensing, respectively (scale bar of 1 cm).

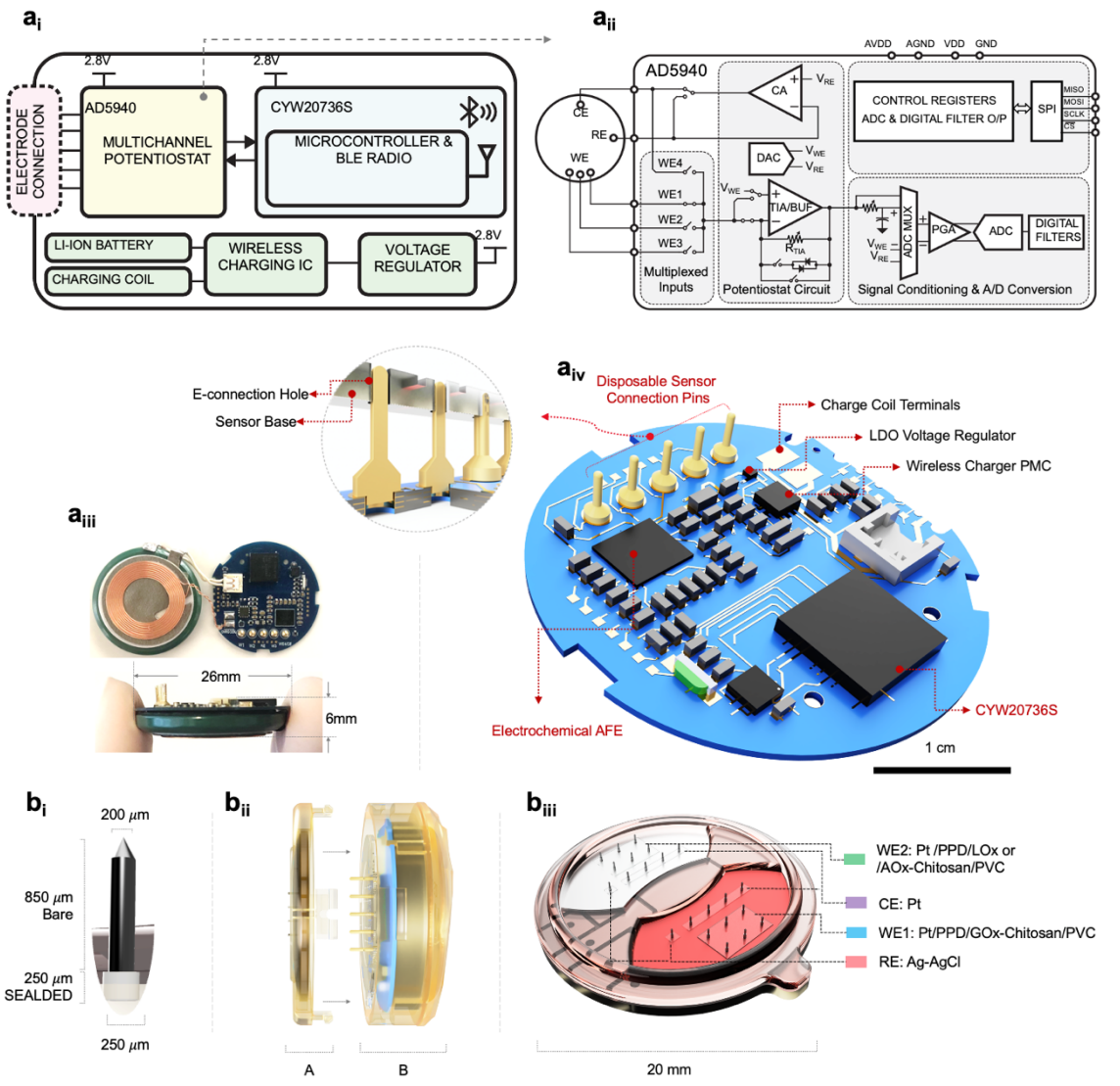
a_i
2.8V
2.8V
ELECTRODE CONNECTION
AD5940
MULTICHANNEL POTENTIOSTAT
CYW20736S
MICROCONTROLLER & BLE RADIO
LI-ION BATTERY
CHARGING COIL
WIRELESS CHARGING IC
VOLTAGE REGULATOR
2.8V
a_ii
AD5940
AVDD AGND VDD GND
CE
RE
WE
CA
DAC
TIA/BUF
CONTROL REGISTERS
ADC & DIGITAL FILTER O/P
SPI
MISO
MOSI
SCLK
CS
WE4
WE1
WE2
WE3
Multiplexed Inputs
Potentiostat Circuit
ADC MUX
PGA
ADC
DIGITAL FILTERS
Signal Conditioning & A/D Conversion
E-connection Hole
Sensor Base
a_iii
26mm
6mm
a_iv
Disposable Sensor Connection Pins
Charge Coil Terminals
LDO Voltage Regulator
Wireless Charger PMC
CYW20736S
Electrochemical AFE
1 cm
b_i
200 μm
850 μm Bare
250 μm SEALDED
250 μm
b_ii
A
B
b_iii
WE2: Pt /PPD/LOx or /AOx-Chitosan/PVC
CE: Pt
WE1: Pt/PPD/GOx-Chitosan/PVC
RE: Ag-AgCl
20 mm
c_i
c_ii
c_iii
c_iv
c_v
c_vi
c_vii

Our fully integrated wearable sensor system enables continuous monitoring of lactate, glucose, and alcohol, each of which can potentially provide unprecedented insights into the (patho)physiology of the body with multiple applications including early diagnosis, prognosis, and management of diseases. For instance, blood lactate level is the most reliable predictor of morbidity and mortality in various groups of critically ill patients with sepsis, organ failure, trauma, and/or acute inflammatory response syndrome[31]. Continuous lactate sensing offers a significant direct benefit in guiding of early resuscitation therapies in patients with emergency health conditions, and the way these patients are treated. It can also be a valuable tool for athletes to reach their maximum body performance and reduce risk of injuries (e.g., by identifying and monitoring their lactate threshold, obtained by plotting the rapidly changing lactate levels during the course of an incrementally intensifying exercise until the point of failure). Additionally, continuous monitoring of glucose is an essential part of managing diabetes for ever increasing number of people with diabetes worldwide[26]. Furthermore, the prevalence of alcohol consumption is linked to a bevy of health complications and therefore, continuous real-time alcohol monitoring could provide functional information to early treatment of alcohol-related health complications including prevalent alcohol use disorders.

Lactate, alcohol, and glucose biosensors were developed on the tip of the MNs. The developed protocol relied on electrodepositing an innermost interference-rejecting polymer layer, poly-*o*-phenylenediamine (PPD), followed by immobilizing the respective oxidase enzyme intermingled in chitosan polyelectrolyte layer and finally, forming non-ionic surfactant-containing polyvinyl chloride (PVC) as the diffusion-limiting outer film. Enzyme loadings and the thickness of each polymer layer were carefully optimized to enable accurate continuous monitoring for each biomarker with excellent selectivity and stability while mitigating biofouling and 'oxygen-

deficiency'. Prior to in-vivo testing on human subjects, the in-vitro analytical performance of each biosensor was investigated in an artificial ISF solution, and results verified their excellent performance in detecting each target biomarker within physiologically relevant concentration ranges, stably and selectively (Extended Data Fig. 10).

2. Results and Discussion

The on-body performance of the MN array biosensor is depicted in Figure 3. The testing protocol is split into an **unchanging single-event** performed for each target analyte biosensor on five different human subjects (Figure 3a – 3d) and **varying multi-event** activities performed for each biosensor on a single human subject (Figure 3e – 3h). The unchanging single-event activities involve asking all the participants to follow an identical exercise protocol, consume identical meal, and an equal amount of wine, serving as triggers to induce concentration fluctuations of lactate, glucose, and alcohol, respectively, and to test the performance of the sensors. Multi-event activities demonstrate each sensor's performance on a human subject in response to a varying activity (i.e., from a low intensity exercise to a high intensity exercise, consuming a full meal to a dessert, and consuming a glass of wine rapidly and then gradually, respectively). The assembly of the integrated wearable sensor components and attaching it to the wearer's arm is shown in Extended Data Video 1. Setup of the custom designed mobile app. alongside a signal test of a sensor on body are presented in Extended Data Fig. 11 and in Extended Data Video 2, respectively.

Figure 2. 3. In-vivo performance of the single analyte sensors. a. Photograph of sensor placed on subject's arm. $\mathbf{b_{i\text{-}iii}}$. Lactate sensor performance study on five human subjects throughout a 4-min high-intensity exercise followed by a resting session, with corresponding lactate blood validation. $\mathbf{b_{iv}}$**.** Plot of ISF lactate data measurements by the sensors *vs*. blood lactate reference measurements. $\mathbf{c_{i\text{-}iii}}$. Glucose sensor performance study on five human subjects following an identical meal consumption event with corresponding blood glucose validation. $\mathbf{c_{iv}}$**.** Plot of ISF glucose data points by the sensors *vs*. blood glucose reference measurements. $\mathbf{d_{i\text{-}iii}}$. Alcohol sensor performance study on five different human subjects throughout a wine consumption event with breathalyzer alcohol measurement validation. $\mathbf{d_{iv}}$. Plot of ISF alcohol data points by the sensors *vs*. alcohol breathalyzer reference measurements. **e.** Photograph of sensor placed on subject's arm. $\mathbf{f_{i\text{-}iii}}$**.** Multi-event study of the lactate sensor throughout varying exercise session beginning with a 1 min of moderate-intensity biking $\mathbf{(f_{ii\text{-}I})}$ followed by a 4 min high-intensity squat-biking combination session $\mathbf{(f_{ii\text{-}II})}$, along with the corresponding plot of ISF lactate measurements by the sensor *vs*. lactate blood strip reference measurements $\mathbf{(f_{iv})}$. $\mathbf{g_{i\text{-}iii}}$**.** Multi-event study of the glucose sensor involving varying food consumption events beginning with consumption of a meal $\mathbf{(g_{ii\text{-}I})}$, then an interval of fasting, and finally consumption of a dessert $\mathbf{(g_{ii\text{-}II})}$, with the corresponding plot of ISF glucose measurements by the sensor *vs*. blood lactate strip reference measurements ($\mathbf{g_{iv}}$). $\mathbf{h_{i\text{-}iii}}$**.** Multi-event alcohol sensor study involving varying wine consumption events beginning with rapid consumption of a glass of wine $\mathbf{(h_{ii\text{-}I})}$, followed by gradual consumption of the same amount of wine spread out between 15 minutes intervals $\mathbf{(h_{ii\text{-}II})}$, with the corresponding plot of ISF alcohol measurements by the sensor *vs*. breathalyzer reference measurements ($\mathbf{h_{iv}}$).

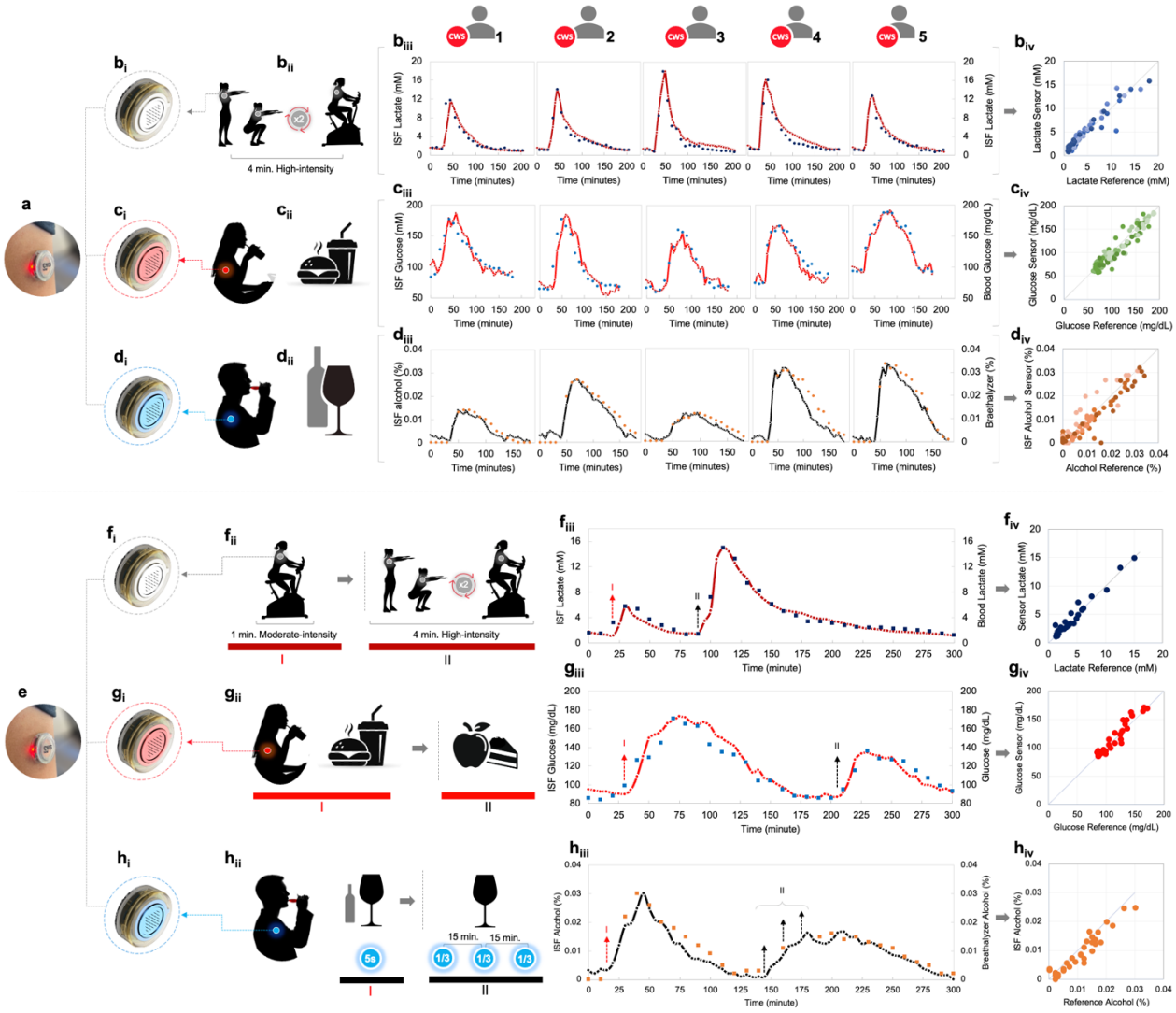
a
b_i
b_ii
4 min. High-intensity
b_iii
CWS 1
CWS 2
CWS 3
CWS 4
CWS 5
ISF Lactate (mM)
Time (minutes)
b_iv
Lactate Sensor (mM)
Lactate Reference (mM)
c_i
c_ii
c_iii
ISF Glucose (mM)
Blood Glucose (mg/dL)
Time (minute)
c_iv
Glucose Sensor (mg/dL)
Glucose Reference (mg/dL)
d_i
d_ii
d_iii
ISF alcohol (%)
Breathalyzer (%)
d_iv
ISF Alcohol Sensor (%)
Alcohol Reference (%)
e
f_i
f_ii
1 min. Moderate-intensity
4 min. High-intensity
I
II
f_iii
Blood Lactate (mM)
f_iv
g_i
g_ii
g_iii
ISF Glucose (mg/dL)
Glucose (mg/dL)
g_iv
h_i
h_ii
5s
15 min.
1/3
h_iii
ISF Alcohol (%)
Breathalyzer Alcohol (%)
h_iv
Reference Alcohol (%)

As shown in Fig. 3b, ISF lactate levels, monitored for each subject in 5 min intervals, rapidly rises from the background value (1-2 mM under resting) after 4 min of a high-intensity exercise, then peaks, and thereafter declines gradually to the original base value. For all subjects, the calibrated ISF lactate levels closely track blood lactate measurements (taken every 10 min) with negligible lag time (< 5 min). The Pearson correlation coefficient (Pearson's r) for the two data sets was found to be 0.94 (105 paired data points), highlighting the strong performance of the wearable MN patch in accurately and continuously tracking the dynamic lactate fluctuations in the body. Highly personalized responses were observed in terms of lactate peak intensities (11.8-18.1 mM), lactate production rate (15-25 min), and its elimination rate (85-130 min). The area under the curve (AUC) for lactate was found to range from 11.27 to 14.82 mM-h. The lactate AUC can provide vital insights into severity and duration of hyperlactatemia in of critically ill patients, and it has been shown as a reliable prognostic marker of septic shock in emergency rooms[32]. The developed MN sensor can thus potentially have a life-saving impact on septic shock patients and substantially reduce the mortality rate among these patients by enabling early diagnosis and timely feedbacks on the undergoing interventions.

Similarly, a high performance was obtained for glucose sensing for all five subjects (Figure 3c), with a mean absolute relative difference (MARD) of 8.83 % (95 paired data points). Personalized responses (i.e., each subject having a unique base glucose level, peaking and decline rates) in terms of the rates of glucose uptake and glycolysis were observed. AUC analyses for glucose data produce values ranging from 220 to 304 mg-h/dL. AUC for glucose has been shown to be a more sensitive predictor than HbA1c and fasting plasma glucose levels for detecting diabetes, and impaired glucose tolerance, and identifying people at increased risk of diabetes[33].

Accordingly, AUC analysis of the MN sensor data suggests that subject #5 can be at an increased risk of developing diabetes.

Instantaneous response to alcohol consumption (Figure 3d) was found with the MN alcohol sensor, beginning from the expected sober values of 0% and thereafter tracking measurements from the gold-standard breathalyzer unit with a Pearson's r of 0.94 (95 paired points). The obtained data showed a large inter-subject variability with peak values ranging from 0.012 % (2.6 mM) to 0.034 % (7.4 mM) and AUC values from 3.29 to 9.25 mM-h, reflecting sex-, weight-, metabolism-, and age-related differences, as well as genetic parameters among participants. Currently, transdermal alcohol monitors, which are mainly approved for research applications, are only able to provide semi-quantitative measures of alcohol consumption. Besides, these sensors suffer from major problems such as considerable lag time (up to several hours), unestablished correlation to blood/breath alcohol content, and thus unreliable detection performances[34]. This work presents the first demonstration of truly continuous, real-time alcohol monitoring with tremendous clinical and personalized utility.

The sensor' response to **varying multi-event** activity/stimuli expected during daily activity is illustrated in Figure 3f-h. Here, the sensor response reflects the differences in intensity between events for each sensor type. For instance, the lactate levels showed a peak intensity of only 5.8 mM with a shorter ~50 min return-to-baseline time corresponding to a one-minute low intensity exercise, but a 15 mM lactate peak with a longer ~160 min return-to-baseline time in the case of the 4 min high intensity exercise. Similarly, the glucose results reflect closely the meal consumed, Figure 3g. In the case of the alcohol levels, the effect of varying the alcohol consumption rate on the subject was captured with a rapid alcohol consumption leading to a higher, sharper peak, whereas a slower one resulted in a lower, wider peak. AUC values were very similar (5.1 *vs*. 5.3

mM-h), reflecting the identical amounts of alcohol consumed for both events. The multi-event profiles obtained for the 3 target analytes with the MN sensors are in excellent agreement with the results of the corresponding reference (blood, breathalyzer) method. Of considerable note is the subjects' pain and discomfort associated with the validation experiments using finger pricking blood meters, as each of single- and multi-event trials required over 30 capillary blood samplings.

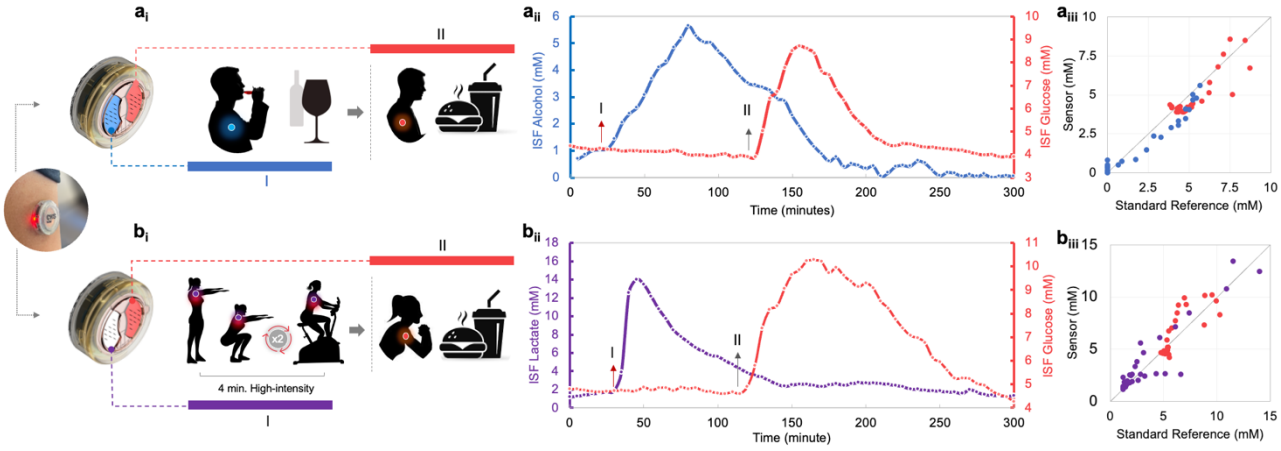

Figure 2. 4. In-vivo performance of the multiple analyte sensors. a. Performance study of the alcohol-glucose multiplexed sensor during ($\mathbf{a_i}$) a wine-consumption event followed by ($\mathbf{a_{ii}}$) a meal-consumption event with ($\mathbf{a_{iii}}$) the corresponding plot of ISF alcohol and glucose measurements by the sensor *vs*. blood alcohol breathalyzer and blood glucose strip reference measurements. **b.** Performance study of the lactate-glucose multiplexed sensor during a 4-minute high-intensity workout followed by consumption of a full meal with ($\mathbf{b_{iii}}$) the corresponding plot of ISF lactate and glucose measurements by the sensor vs. the blood lactate and glucose strip reference measurements.

The multiplexed monitoring ability of the MN sensor is demonstrated for simultaneous alcohol-glucose and lactate-glucose sensing. Given the influence of alcohol consumption on glucose homeostasis, alcohol monitoring along with glucose can provide invaluable personalized information for individuals toward reducing their risk of developing type 2 diabetes[35]. The ability of multiplexed alcohol-glucose monitoring in real-time can also help people with diabetes avoid delayed hypoglycemia which usually occurs following alcohol intake due to the reduced gluconeogenesis and depleting the glycogen stores[36]. On the other hand, monitoring lactate along

with glucose can offer a more comprehensive pro-diagnostic information regarding the risk of metabolic syndrome[37]. Additionally, given different glycemic response of the people with diabetes to exercise, lactate monitoring can help more precise insulin delivery adjustment in these patients[36]. Despite the high demands for such multiplexed monitoring of metabolites, to date there is no device capable of continuously and simultaneously measuring glucose-lactate in real-time. Figure 4a illustrates the response of the alcohol-glucose sensing for alcohol consumption followed by consumption of a glucose-rich meal. The lag-free temporal biomarker profiles (Figure $4a_{ii}$) of the sensor corresponds to the breath- and blood-based validation measurements (taken in parallel) without any evidence of chemical or electronic crosstalk between the individual sensors. The chemical crosstalk, which can occur due to the migration of hydrogen peroxide between sensors of different analytes, is especially a major concern when designing an oxidase-based multi-sensor for in-vivo applications. Molecular crosstalk is herein addressed through both a judicious design via spatially separating the dual sensing regions (11 mm) and an optimized mitigated sensitivity achieved via utilizing a smaller number of working electrodes for each analyte. Accordingly, the Pearson's r for alcohol and glucose were found to be 0.98 and 0.86, respectively, highlighting the high accuracy of the multiplexed MN monitoring of the two markers. Moreover, simultaneous monitoring of lactate and glucose resulted in successful tracking of each metabolite in response to their respective stimuli without any crosstalk between the two sensing systems, Figure 4b (Pearson's r of 0.92 and 0.81 for lactate and glucose, respectively).

3. Conclusion

In summary, we have successfully demonstrated a fully integrated wearable microneedle platform for painless, continuous, real-time simultaneous measurements of multiple biomolecules from interstitial fluid in a tremendously low-cost manner. Measurement data was acquired through

custom designed electronics, and wirelessly transmitted to an accompanying smartphone app for capture and visualization. By relying on the ISF as a rich source of biochemical information, the system collects in real-time rich molecular data continuously during diverse daily activities that currently can be obtained only as a single measurement by centralized laboratory tests. The performance of the wearable platform was thus demonstrated by monitoring fluctuating ISF levels of key biochemical markers lactate, alcohol, and glucose- in single and multiplexed configurations, in response to stimuli associated with common daily routines, namely exercise, food consumption, and alcohol consumption. Every experiment on each human subject was validated by parallel measurements using standard reference methods. Our system addresses the fundamental practicality issues of epidermal sweat measuring wearables, as well as the invasiveness and limited single-analyte capability of CGMs, thereby enabling pain-free, non-intrusive, multiplexed monitoring of biomarkers from the body. Furthermore, the platform can readily be reconfigured for detection of additional biomarkers, facilitating the continuous collection of clinically relevant data not previously accessible and therefore potentially providing a more comprehensive view into the body's physiology. Future steps will include developing calibration-free MN sensors with largely extended operational lifetimes. Lastly, by filling the current gaps between research and commercialization, the current work presents a significant leap forward in the field and can accelerate the emergence of next generation, patient-centered remote monitoring wearable sensors, thereby offering a pathway to transform the digital healthcare as we currently know.

4. Methods & Materials

Glucose oxidase (GOx, EC 1.1.3.4, from Aspergillus niger), D-(+)-glucose anhydrous, alcohol oxidase (AOx, from Pichia pastoris, 10–40 units/mg), chitosan (medium molecular weight), bovine serum albumin (BSA), γ-globulins from bovine blood, L-lactic acid, ascorbic acid

(AA), calcium chloride anhydrous ($CaCl_2$), glacial acetic acid (HOAc), poly(ethylene glycol) diglycidyl ether (PEGDE), hydrochloric acid (HCl), polyvinyl chloride (PVC), Triton X-100, *o*-phenylene diamine (oPD), acetaminophen, and uric acid (UA), sodium sulphate (Na_2SO_4), iron (III) chloride ($FeCl_3$), magnesium sulfate anhydrous ($MgSO_4$), phosphate buffer solution (PBS) (1.0 M, pH 7.4), potassium chloride (KCl), sodium dihydrogen phosphate (NaH_2PO_4), sodium bicarbonate (NaHCO3), sodium chloride (NaCl), sodium gluconate, and sucrose were purchased from Sigma-Aldrich. Lactate oxidase (LOx, EC 1.1.3.2, 106 U/mg) was obtained from Toyobo, USA. Ethanol was obtained from Decon Laboratories (Austin, USA). Tetrahydrofuran (THF) was provided by Millipore (Massachusetts, USA). Biocompatible BioMed photocurable resins were purchased from Formlabs (Berlin, Germany). 3.2 mm thick poly (methyl methacrylate) (PMMA) sheets were purchased from McMaster-Carr (Chicago, USA). 3M™ Medical Tape was purchased from Tekra (New Berlin, USA).

Design and fabrication of disposable MN component. The MN array with the capillary channels on the base for sealing, the MN covers, enclosure and holder components were all designed using Fusion 360 software (Extended Data Fig. 6). 3D printing (Formlabs 3) was used to fabricate the cover ring, and reproducibly high resolution (1μm) micromachining process was used to fabricate the MN array with the sealing microfluidic channels on the base of the MN array (Extended Data Fig. 6) in a scalable and cost-effective manner. The cover and MN array were then assembled with the photocurable resin being introduced to the interface followed by spontaneously forming a sealant layer at the interface and around the MNs up to the MNs reproducibility cutoff line. Briefly, for the single analyte sensors (i.e., lactate, glucose, alcohol), a 3-electrode electrochemical system was used with the electrodes ratio of 16WE/8CE/1RE, Extended Data Fig. 6,7. The multiplexed sensors (i.e., lactate-glucose, alcohol-glucose), relied on two 3-electrode

systems, with 2 physically isolated working electrodes, 2 complementary counter electrodes, and 2 complementary reference electrodes, in the ratio of 6WE/8CE/1RE (Fig. $2b_{iii}$).

4.2. Preparation of biosensors.

o-PD (5 mM) solution was prepared in an acetate buffer (I = 0.2 M, pH 5.2) and electrodeposited at 0.65 V (vs. Ag/AgCl) for 15 min. The enzyme solutions GOx (20 mg/mL), LOx (12 mg/mL), and AOx (10 mg/mL) were prepared in chitosan (1 wt% in 1% HOAc) in optimized volume ratios of 1:2, 1:10, and 1:1, respectively. 2 μL of each enzyme solution was used to modify the corresponding biosensor by covering the microneedle array, followed by crosslinking with 1 μL of PEGDE (1%). The electrodes were then modified by casting chitosan solution (1, 2, and 1 μL for glucose, lactate, and alcohol biosensors, respectively). Finally, a 2% PVC solution prepared in THF solvent and containing 1 mM Triton X-100 was cast onto the microneedle (1 μL for the glucose and lactate biosensors, and 1.5 μL for the alcohol biosensor) and chilled for 4 h at 4°C for further experimentation.

4.3. Sterilization and cytotoxicity test.

Cytotoxicity of the MN array was tested through Live/Dead staining of J774 cells in DMEM media (Thermo Fisher, Waltham, USA), by immersing the disposable piece of the MN patch in advance. J774 macrophage cells (2×105/ml) were seeded to a 6-well plate and cultured for 24 h at 37 °C. The sample was prepared by immersing the MN patch that is sterilized by UVc and autoclave for 24 h. The cell-containing wells were washed with PBS, then treated with a Live/Dead staining kit (BioLegend, San Diego, USA). Fluorescence images were taken by an inverted fluorescent microscope and analyzed using ImageJ to determine the percentage of live and dead cells in each sample (N=5) (Extended Data Fig. 9a, b). Further UVc sterilization was

performed on each enzyme immobilized sensor (30 minutes, Level II) prior to application onto the body, (Extended Data Fig. 9a, b).

4.4. Electronic System Fabrication and Assembly.

All the components of the electronic system are assembled onto a 4-layer FR4 printed circuit board (PCB) which measures 0.5mm in height and 5.3 cm^2 in area (r = 13mm). Fabrication and assembly were performed by PCBminions (Princeton, NJ, USA & Shenzhen, China). All components were sourced from Digi-Key Electronics (Thief River Falls, MN, USA). Components include the AD5940 electrochemical analog front end (AD5940BCBZ-RL, Analog Devices, Inc., Wilmington, MA, USA), the CYW20736S Bluetooth Low Energy (BLE) system-in-package (SiP) module (CYW20736S, Cypress Semiconductor Corporation, San Jose, CA, USA), a 2.8V low-noise, low quiescent current low-dropout (LDO) regulator (LP5907UVX-2.8/NOPB, Texas Instruments, Dallas, TX, USA), a wireless Li-ion battery charger (LTC4124EV#TRMPBF, Analog Devices, Inc., Wilmington, MA, USA), a wireless charging coil (WR202020-18M8-G, TDK, Chuo City, Tokyo, Japan), and a 110mAh Li-ion coin cell battery (RJD2430C1ST1, Illinois Capacitor, Des Plaines, IL, USA). The electrode connection consists of 5 gold plated nickel, 0.508mm diameter pins (0508-0-00-15-00-00-03-0, Mill-Max Manufacturing Corporation, Oyster Bay, NY, USA).

4. 5. Electrochemical Sensing Operation.

The AD5940 electrochemical analog front end (AFE) integrates multiple circuits for performing electrochemical analysis, which are functionally grouped into circuitry for multiplexed input selection, potentiostat operation, signal conditioning and digital conversion, and data communication. The AFE interfaces with the sensor array through the five gold-plated pins. Four of the pins are used as multiplexed input channels when operating in a 2-electrode configuration

(labeled WE1, WE2, WE3, and WE4), with the fifth pin used for a combined counter / reference electrode. When operating in a 3-electrode configuration, three working electrodes are available for multiplexing (WE1, WE2, WE3), and the fourth and fifth pins are used for the counter and reference electrodes. Each working electrode input can be individually addressed to connect the electrode to the potentiostat circuit for electrochemical analysis.

The potentiostat circuit consists of a control amplifier (CA), a transimpedance amplifier (TIA), and a 12-bit dual output digital-to-analog converter (DAC) which sets the common mode reference electrode potential (V_{RE}) and working electrode potential (V_{WE}). The TIA converts input current I_{In} into a voltage to be measured by the ADC. The potential difference ($V_{WE} - V_{RE}$), set by the DAC, is applied to a connected electrochemical cell through the control amplifier and TIA. The operational range for the applied potential is +/- 1.0V with a resolution of 0.537mV (12-bit DAC, $V_{Ref} = 2.2V$).

Signals from the TIA feed into the signal conditioning and digital conversion circuitry, which include a programmable analog RC filter, a differential multiplexer (labeled ADC MUX), a programmable gain amplifier (PGA), a 16-bit analog-to-digital converter (ADC) for digitizing signals into measurement data, and cascaded digital $sinc^3$ and $sinc^2$ filters. Both the TIA and PGA feature programmable gain values. The ADC is configured to measure the differential voltage between the amplifier output and V_{WE} via the ADC MUX.

The AFE also contains data registers to store configuration information and for storing measurement data from the ADC or digital filters. All data communication with these data registers occurs through the AFE's SPI interface.

Signal filtering on the AFE, which is used to suppress random electronic noise and electrochemical noise, is accomplished in both the analog and digital domains. A single pole low

pass analog filter is formed by a programmable resistor and a 1μF capacitor located at the output of the TIA/BUF amplifier. The resistor is set to 20kΩ, resulting in a 3dB cutoff frequency of 7.96 Hz, which was chosen suppress noise whilst not allowing the filter's settling time to cause measurement inaccuracies for the capacitive currents found in amperometry tests. The ADC output connects to a digital $sinc^3$ filter followed by a $sinc^2$ filter. Configuring the bandwidths of these filters is done by digitally setting their oversampling ratios, which are set to 5 and 1333 for $sinc^3$ and $sinc^2$, respectively (the maximum setting on the AFE). This produces an overall filter 3dB bandwidth of 38.32 Hz at a sampling rate of 800kSPS (found through simulation). Note that the frequency response of digital sinc filters is similar to that of averaging / integration methods commonly used in electrochemical analysis. An additional 60 Hz / 50 Hz mains filter is used after the sinc filters.

Signal amplification is performed by the TIA and PGA to ensure that their levels are always within the detectable limits of the ADC over a wide range of input current. An autoranging system is employed to dynamically adjust the TIA and PGA gains during tests to do so (Temporary Figure S3b). The system algorithm, depicted in Temporary Figure $S3b_i$, recursively tests different transimpedance values until the signal level is within 20% to 80% of the ADC's full range. Each gain level covers 12.04dB of range, except for the highest transimpedance level (upper left bar in Temporary Figure $S3b_{ii}$) which covers 73.1dB from 16.2nA down to 3.6pA (the limit of detection for the electronic system), and the lowest transimpedance gain level (lower right bar in Temporary Figure $S3b_{ii}$) which extends from 0.83mA up to 2.15mA for a range of 8.3dB. The autoranging system allows the electronic system to support a range of 2.15mA to 3.6pA (175dB of range). Note that a diode pair is connected to the TIA's feedback path to not disturb the cell biasing (allowing current to flow) while switching between R_{TIA} values.

4. 6. BLE Operation.

The CYW20736S BLE SiP module features an ARM Cortex-M3 microcontroller (MCU), a BLE radio, and an embedded planar inverted-F antenna. The module is programmed to control all electronic system functionality, namely configuration of the AFE through its SPI bus, control of electrochemical measurement data acquisition, and wireless communication with a mobile device over BLE.

Wireless BLE operation of the electronic system is depicted in Temporary Figure S3c. The electronic system is configured as a Bluetooth Generic Attribute Profile (GATT) server and hosts custom services and characteristics which a GATT client – the smartphone – can interact with. The BLE GATT is organized into "services" which group together pieces of data referred to as "characteristics." Two services are used for electrochemical tests: a configuration service and a measurement data service. The configuration service contains characteristics for setting test parameters (e.g., applied potential for amperometry). The measurement data services act as unique data channels for transmitting data, and trivially contains a characteristic for measurement data. Prior to transmission, measurement data acquired through the ADC is converted to relevant measurement units – current in pA for amperometry.

4.7. Power Management and Wireless Recharging.

The power management and wireless recharging circuitry on the electronic system consist of a wireless recharger IC, a 2.8V LDO, and a wireless charging receive coil. Power for the electronics is sourced from the rechargeable Li-ion battery – a 2430 type (24mm in diameter, 3.0mm in height) coin cell. The battery, receive coil, and PCB are adhered to each other with double-sided tape, resulting in a total device height (from the top of the battery connector to the bottom of charging coil) of 6mm and a diameter of 26mm.

Under normal operation, power is sourced from battery, through the wireless recharger IC, and into the LDO. The LDO then regulates the battery voltage (~3.7V) down to 2.8V, which is supplied to the AD5940 and CYW20736S. The electronic systems begin inductively charging the battery when it is placed on a transmitter pad (Temporary Figure S2). Charging is regulated by the wireless recharging IC, which features over-discharge protection and constant current / constant voltage charging capability to quickly charge the battery without overcharging.

4. 8. Power Optimizations.

Both the AD5940 AFE and CYW20736S BLE module feature "sleep" modes to reduce average power consumption by power-gating and/or clock-gating circuit blocks. This is leveraged on the AFE by turning the ADC and digital filters *on* solely for periodic sampling events and turning them *off* outside of these events. Furthermore, the microcontroller and BLE radio on the CYW20736S are deterministically gated between sampling events. Note that throughout an entire electrochemical test, the DAC, control amplifier, and TIA/BUF amplifier are left on to maintain the reference electrode potential and maintain / measure the working electrode potential for potential-controlled / potentiometry tests.

Temporary Figure S1 depicts the instantaneous current consumption before, during, and after a single sampling event. An increase in current to ~10mA is observed at t = 0.4s, indicating that the microcontroller, ADC, and digital filters have been turned on to begin a sampling event. The current drops down shortly after, indicating that data had been sampled and the microcontroller, ADC, and digital filters have turned off. Next, the current spikes to ~20-30mA, indicating that the BLE radio and microcontroller have turned on, which occurs for 3 sequential BLE connection events. During the first, data is transmitted to a mobile device. Next, the electronic system receives a confirmation from the mobile device that the measurement data had been

properly received. Lastly, the electronic system receives an empty BLE packet from the mobile device, telling the electronic system that no further BLE communication will take place, allowing the BLE radio to be kept off until the next sampling event. Before and after these events, the low current levels labeled “Sleep” verify that ICs were successfully placed into low power modes. Small spikes of ~5mA appear every 100ms – this is the CYW20736S periodically waking up to briefly to perform basic system operations, such as flashing the electronic system’s LED, taking battery level measurements, or checking if data needs to be retransmitted due to a BLE disconnect.

Temporary Figure S1b depicts the average current consumption of a 60s amperometry test (sampling interval = 1s) and the instantaneous current of 3 sampling events during this test for reference. Notice that the average current lies close to the “Sleep” current found between sampling events, as the electronic system remains primarily in sleep mode given the long sampling interval**.**

Current consumption decays back to 1.06mA as the sampling interval is increased back to 1s, resulting in a battery life of 4 days and 7.6 hours. Additionally, the electronic system can be placed into an ultra-low power mode via a BLE command whereby all components are turned off for a preset duration of time. In this mode, the electronic system consumes 53.5µA. Duty cycling this ultra-low power mode with continuous sampling allows for significant battery life gains, as shown in Temporary Figure S1c. For instance, 10% duty cycling with 1 minute of continuous sampling mode (sampling interval = 1s) followed by 9 minutes of ultra-low power mode results in average current consumption of 154µA and a battery life of approximately 30 days.

4. 9. Firmware Programming.

Temporary Figure S3a depicts the programming and reprogramming procedure for the electronic system. Programming uses UART connections (Tx, Rx, VCC, GND), and requires a physical connection between the electronics and a personal computer which hosts the firmware.

This is accomplished by first connecting the electronics to a Cypress BCM92073X_LE_KIT development kit through a 6-pin Molex PicoBlade cable, and connecting the kit to the personal computer using a micro-USB cable. The development kit is needed specifically for its on-board FTDI USB-UART interface chip, which converts serial UART signals into serial USB signals. Initial programming the electronics is accomplished using Cypress' WICED SMART, a software development kit (SDK) which provides an Eclipse-based integrated development environment (IDE) for building firmware and downloading it to the electronics. Thereafter, the programming header of the electronics (which has no active components) is cut off, making the electronic system ready to be integrated with the sensor array.

Reprogramming can be done through over-the-air (OTA) updates via BLE. Afterward, programming is done wirelessly via BLE through Over-the-Air (OTA) updates. This enables rapid deployment of firmware updates in line with today's agile software development environments

4. 10. In-vitro characterization of the sensors.

In-vitro characterizations were performed in an artificial ISF solution to evaluate and optimize the performance of each biosensor (Extended Data Fig. 10). The artificial ISF solution was prepared per the procedure described in our previous work[29]. Calibration experiments for each biomarker were performed, covering the physiological ranges of each analyte. The amperometric responses obtained at applied potential of 0.6 V (Extended Data Fig. 10 $a_{ii,}$ b_{ii}, and c_{ii} for lactate, alcohol, and glucose, respectively), and the corresponding calibration plots (Extended Data Fig. 10$a_{iii,}$ b_{iii}, and c_{iii}) reveal the excellent linearity of the biosensors. The stability of biosensors was examined by attaching a modified microneedle device to a custom-designed electrochemical chamber with full sealing of the containing solution (1 mL volume), spiking with specific target

analyte concentrations (10 mM lactate, 15 mM alcohol, and 10 mM glucose), and recording amperometric responses at 10 min intervals for 12 h. As illustrated in Extended Data Fig. 8a_{iv}, b_{iv}, and c_{iv}, the biosensors exhibited remarkable stability over a prolonged duration of time. Finally, the selectivity of the biosensors was verified by adding concentrations of the target analyte into artificial ISF containing common interfering species (i.e., ascorbic acid, uric acid, acetaminophen, tryptophane, methionine and histidine) (Extended Data Fig. 10 a_{vi}, b_{vi}, and c_{vi}).

4. 11. On-body characterization of the sensors.

Fully sterilized sensor patches were placed on the left or right arm of each subject using double-sided medical tape and an extra tape to cover the microneedle patch on the skin. Testing commenced immediately, achieving <6 initial data points (<30 minutes) to form a stable baseline followed by the initiation of the activity (e.g., exercise, food, or alcohol consumption) while sensor operating in the background. Protocol for each activity is as follows.

Lactate continuous sensing: In the unchanging single-event experiments (Fig. 3b), each participant went through a 4-minutes high-intensity exercise starting with a 1-minute body-squat (i.e., 30 repetitions), immediately followed by a 1-minute interval biking (i.e., a 30-second of slow low-intensity at 50 RPM with resistance of 3/10 that rapidly turns into a 30-seconds of a faster high-intensity at 50 RPM with resistance of 8/10), followed by 45 s of resting all of which were repeated for 2 times. For the varying multi-event lactate experiment (Fig. 3f), the participant first went through a 1-minute, moderate-intensity biking (i.e., at 50 RPM and a 6/10 resistance), and then 4 minutes of a high-intensity exercise session described above. A similar 4-minute high-intensity exercise was performed for the multiplexed lactate-glucose sensing experiment (Fig. 4b).

Glucose continuous sensing: For the unchanging single event (Fig. 3c), each participant consumed a “double quarter pound KING burger” with a “20 oz bottle of Coca-Cola”. In the varying multi-event glucose experiment (Fig. 3j), the participant, first consumed the same burger and coke combination, and then consumes one piece of a cheesecake (≅120g) and a large apple (≅200g). For both multiplexed sensing experiments, both participants consumed the same burger and coke combination.

Alcohol continuous sensing: One glass of wine (150 mL of 14.5% alcohol content purchased from a local supermarket) was consumed in every alcohol monitoring experiment (Fig. 3c & J, Fig. 4a). In the unchanging single event experiments, the alcohol was consumed in a rapid one-single shot (<5 seconds), and in the varying multi-event experiment, the same one-glass of wine was consumed in 3 occasions with 15 minutes of interval in between (Fig. 3h). Amperometric experiments carried out for 60 s at 5 minutes intervals were exploited for all experiments with the last data point being calibrated versus the gold-standard metrics using two-point calibration method.

The lactate, alcohol and glucose data were validated in 10 min intervals by commercial blood lactate meter (NOVA Biomedical), breathalyzer (BACtrack S80 Pro), and blood glucose meter (ACCU-CHEK), respectively. In case of alcohol monitoring tests and according to the instructions from the manufacturer, subjects were asked to wait 15 min before recording their breath alcohol content by breathalyzer.

Figure 2. Extended Data 1. Disassembled components of the sensor showing (from left to right) the patch enclosure cap, battery, recharge coil, PCB, holder B, MN single analyte 5-by-5 sensor array, multiple analyte sensor array (with corresponding cover ring of each on the below and the assembled piece on the top of each sensor array), holder A, and a double sided disposable medical tape

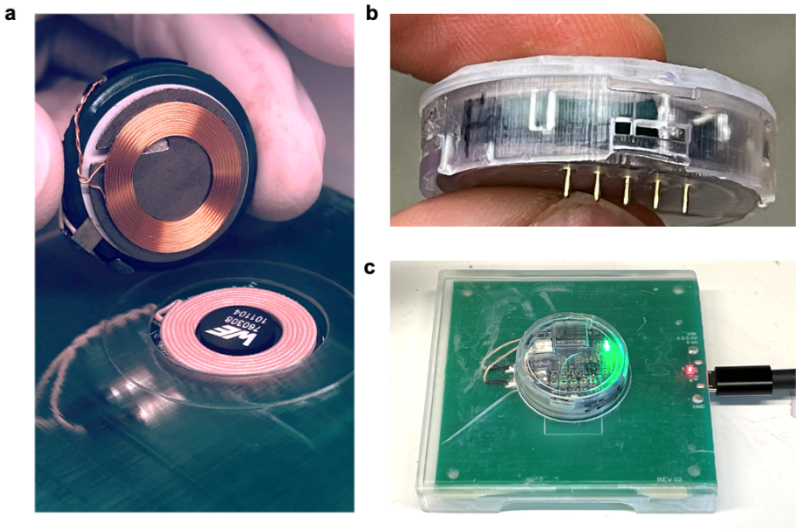

Figure 2. Extended Data 2. Wireless recharging hardware for the electronics sub-system. **a.** Inductively coupled coils on the electronics and transmitter pad (DC2771A-B WPT, Analog Devices, Inc., Wilmington, MA, USA) with coils to support wireless power transfer **b**. Plastic housing on the electronics, providing an air gap between the coils when charging without degrading charging performance. **c.** Electronics placed on transmitter pad, receiving power via the connected micro-USB cable.

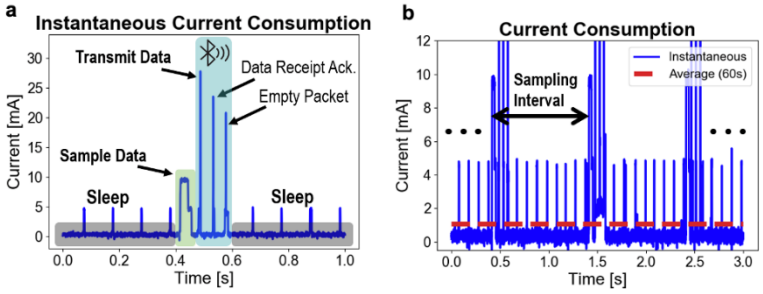

c

Duty Cycle	Avg. Current [mA]	Battery Life	Usage Example
100%	1.06	4 days, 8 hours	Continuous sampling
50%	0.557	8 days, 6 hours	1min. sampling, 1min. sleeping
20%	0.255	17 days, 24 hours	1min. sampling, 4min. sleeping
10%	0.154	29 days, 18 hours	1min. sampling, 9min. sleeping

Figure 2. Extended Data 3. Power optimization for the electronics. **a.** Instantaneous current consumption for 1 sampling event. **b**. Instantaneous and average current consumption (= 1.06mA) for a 60s test (sampling interval of 1s) zoomed into the first 3 sampling events. **c.** Utilizing the ultra-low power mode (current consumption = 53.5μA) to reduce average current consumption via duty cycling.

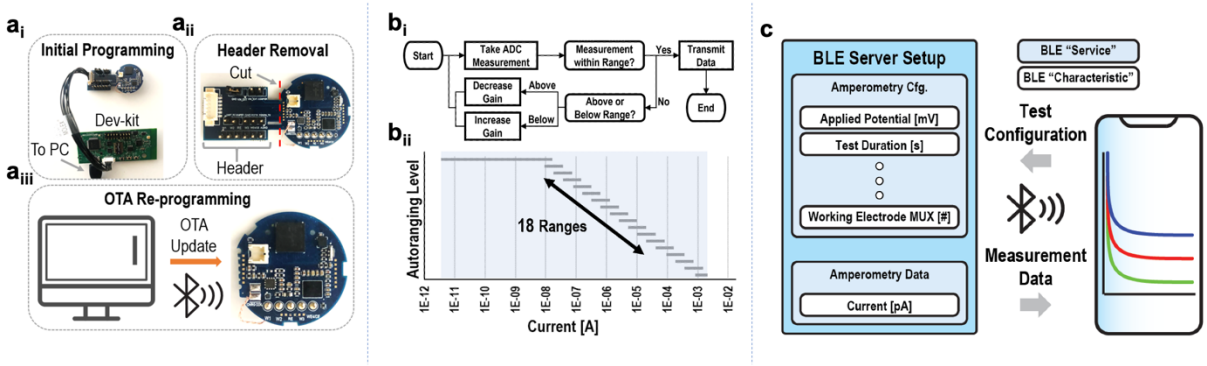

Figure 2. Extended Data 4. Software features of the electronics sub-system. a_i. Programming and reprogramming steps of the electronics, including initial programming from a PC hosting the firmware, removal of the programming header, and OTA reprogramming through wireless BLE communication. **b.** Autoranging system used for dynamic gain adjustment. b_i. Flowchart of autoranging algorithm. b_{ii}. Current ranges corresponding to each for each of the 18 levels available to the autoranging system. (**c**) BLE operation for the electronics. The BLE GATT server contains BLE services for configuring electrochemical tests and for test measurement data, allowing a mobile device to act as a proxy for easy control of the electronics.

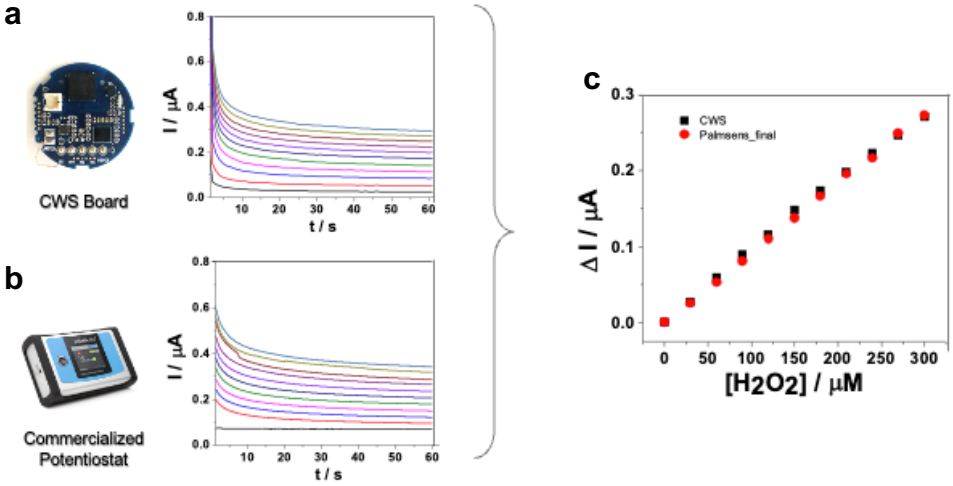

Figure 2. Extended Data 5. a. CWS board Electronic system *vs.* b. a commercialized potentiostat and their amperometric response to standard additions of 30 uM hydrogen peroxide in a PBS solution with **c**. their overlaid calibration curves. Applied potential, 600 mV.

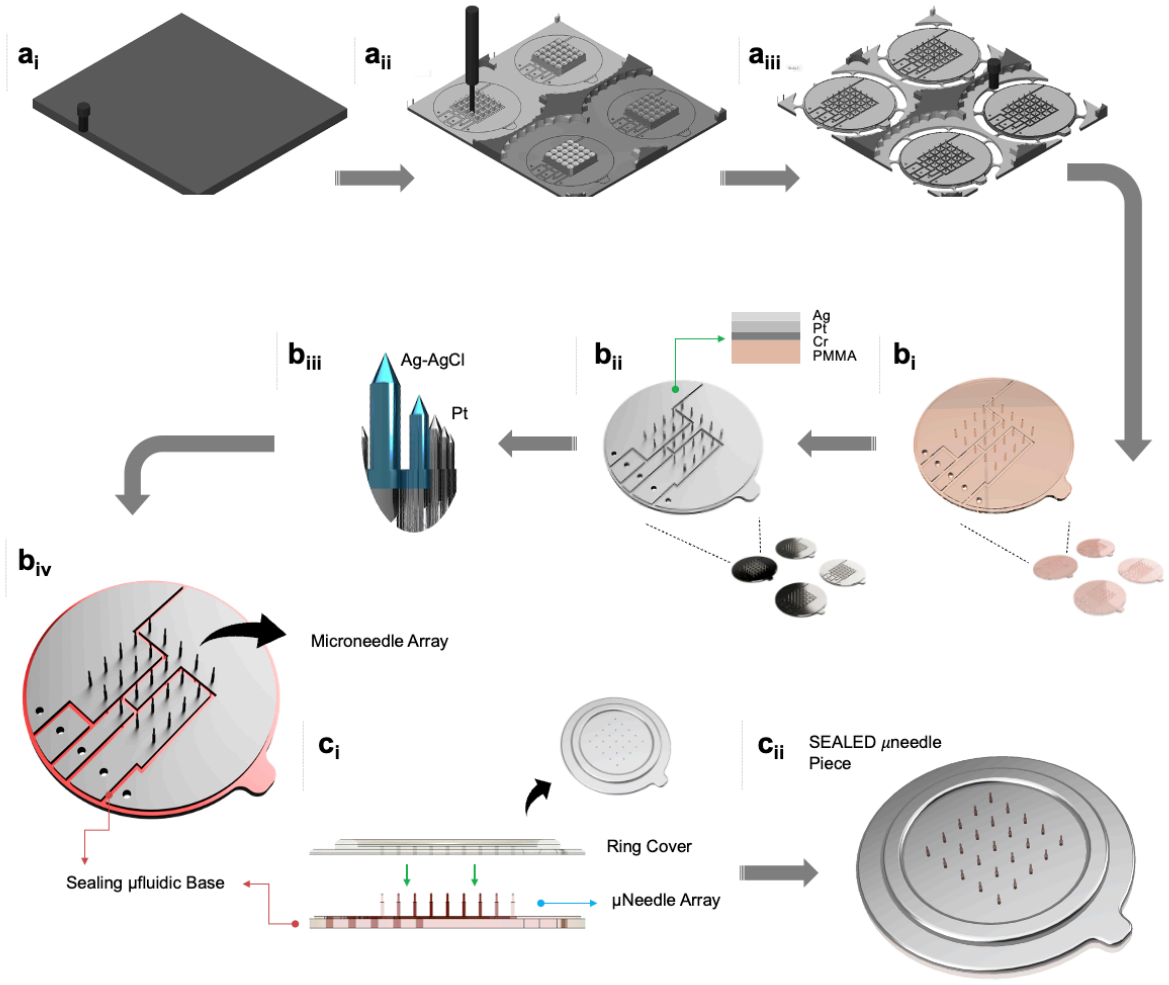

Figure 2. Extended Data 6. Fabrication method of the MN sensor array. $a_{i\text{-}ii}$. Micro-machining of the microneedle array and capillary channels for sealing a_i, a rectangular PMMA block to the intermediate **(a_{ii})** and final **(a_{iii})** engraving steps. $b_{i\text{-}iv}$. Thin-film deposition steps starting from a batch of a clean PMMA microneedle array **(b_i)** to the same batch being sputtered by Cr/Pt/Ag **(b_{ii}),** followed by etching of Ag from all working and counter microneedle microelectrodes, then chloritization of the Ag to Ag-AgCl as the reference microelectrodes **(b_{iii})**, which is followed by electrical isolation of the WE, CE, and RE regions **(b_{iv})**. $c_{i\ \&\ ii}$. Assembly of the ring cover and microneedle array followed by sealing/electrode definition steps.

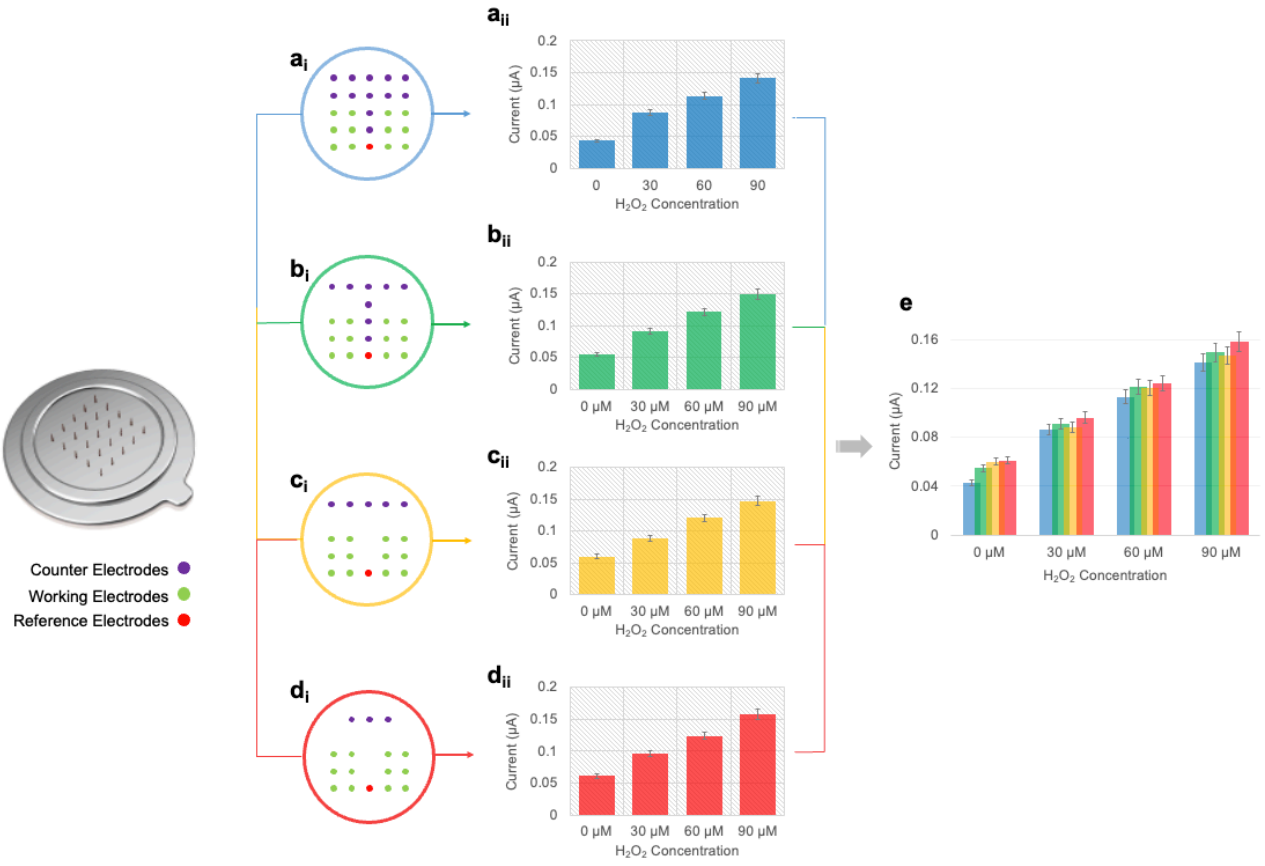

Figure 2. Extended Data 7. WE/CE/RE ratio study. ai-ii. 12/12/1 ratio of the WE/CE/RE respectively and its corresponding amperometric signal in the presence of 0 (PBS), 30, 60, and 90 μM of hydrogen peroxide. bi-ii. 12/8/1 ratio of the WE/CE/RE respectively and its corresponding amperometric signal in the presence of 0 (PBS), 30, 60, and 90 μM of hydrogen peroxide. of ci-ii. 12/5/1 of the WE/CE/RE respectively and its corresponding amperometry signal in the presence of 0 (PBS), 30, 60, and 90 μM of hydrogen peroxide. di-ii. 12/3/1 of the WE/CE/RE respectively and its corresponding amperometry signal in the presence of 0 (PBS), 30, 60, and 90 μM of hydrogen peroxide. e. Overlaid results of all three microelectrode ratios and their ampetrometric responses versus hydrogen peroxide concentration in the sensing medium.

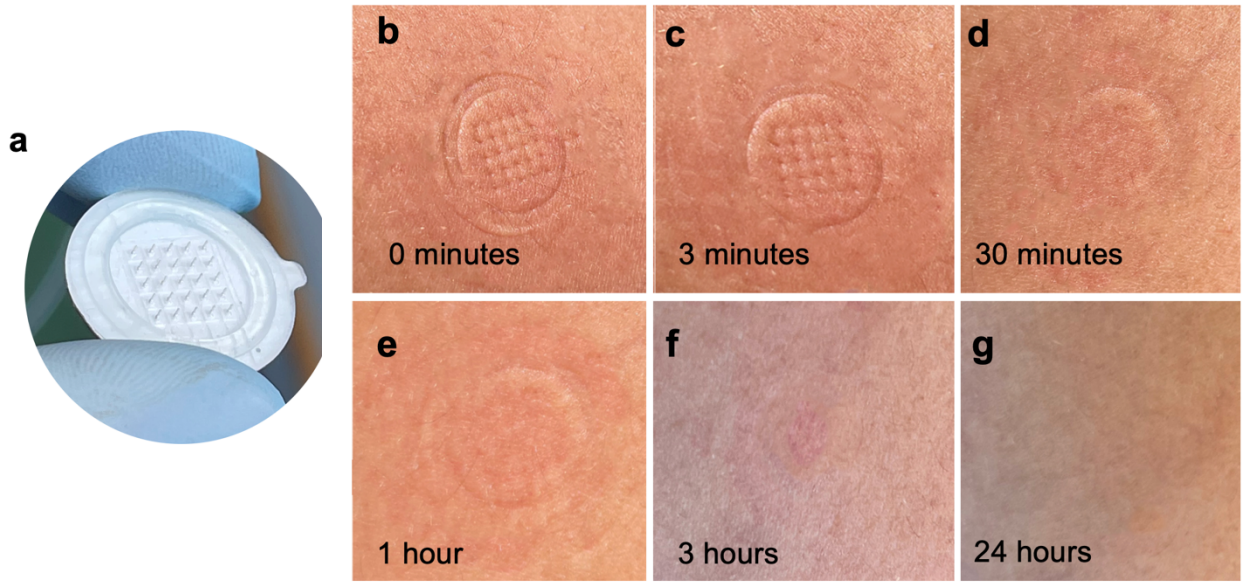

Figure 2. Extended Data 8. a. An individual disposable array of 5 by 5 microneedle component before application to the skin. **b-g.** sensor's visual impact on the skin of a subject immediately after removal of the sensor patch (0 minutes) to 24 hours after the time of removal.

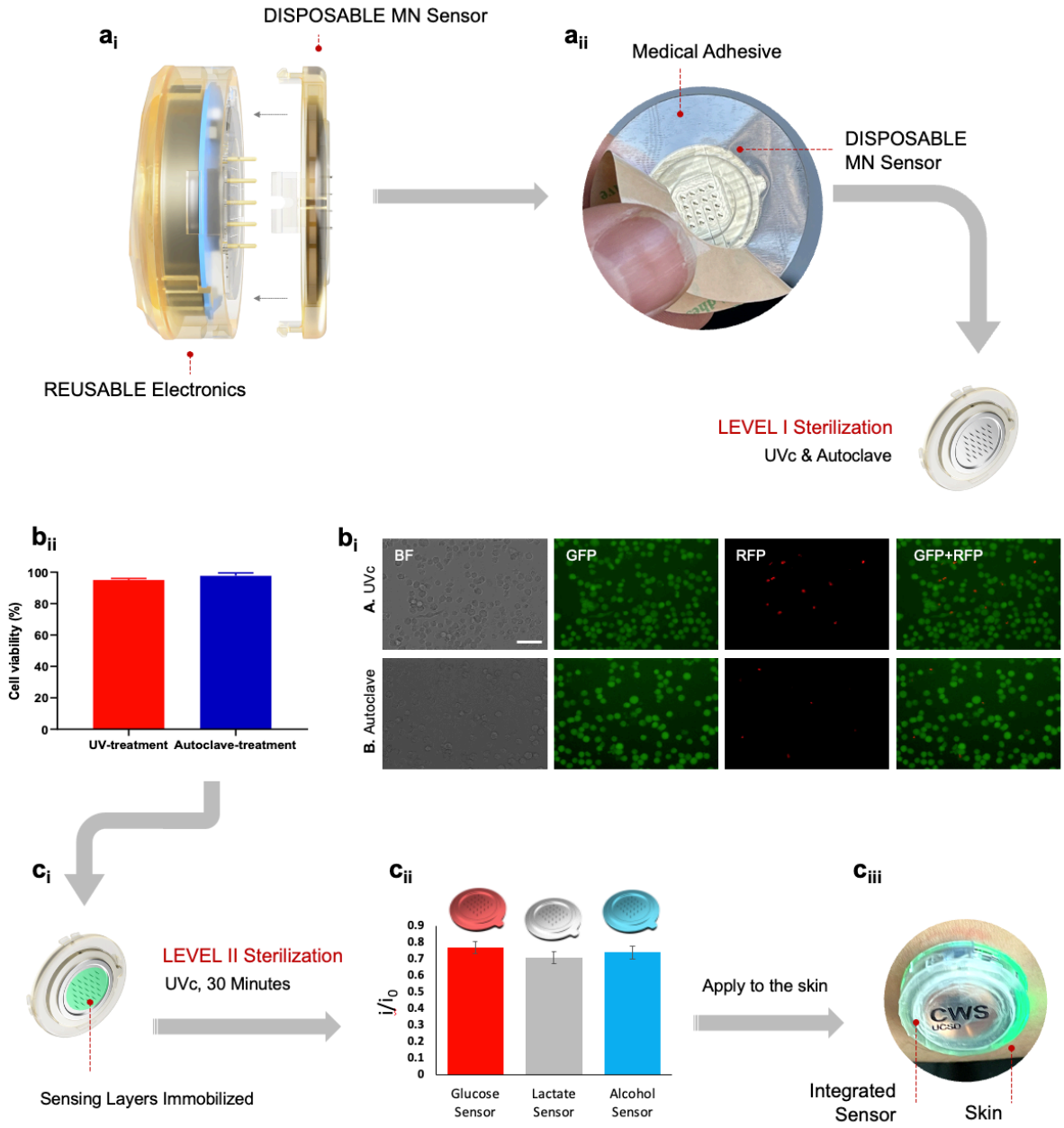

Figure 2. Extended Data 9. Sensor sterilization process and cytotoxicity studies. a_i. Illustration of the two disposable and reusable components of the sensor. **a_{ii}**. Sterilization process of the sensor's disposable component beginning by a 24- hour autoclave and UVc step, with the corresponding in-vitro cytotoxicity test with J774 cells. **b_i.** Representative microscopy images of live and dead cells after incubation with MN patch sterilized by ultraviolet (A) and autoclave (B). GFP: Calcein AM labeled live cells. RFP: propidium iodide labeled dead cells. Scale bar: 50µm. **b_{ii}**. Cytotoxicity of MN patch sterilized by ultraviolet and autoclave when incubated with J774 macrophages. **c_i**. Level II UVc sterilization of the disposable sensor component after immobilization of the sensing layers. **c_{ii}**. The impact of Level II sterilization on each sensor in terms of their sensitivity drop. **c_{iii}**. An image of a sterilized fully integrated sensor on a human subject skin with the disposable sensor being fully sterilized.

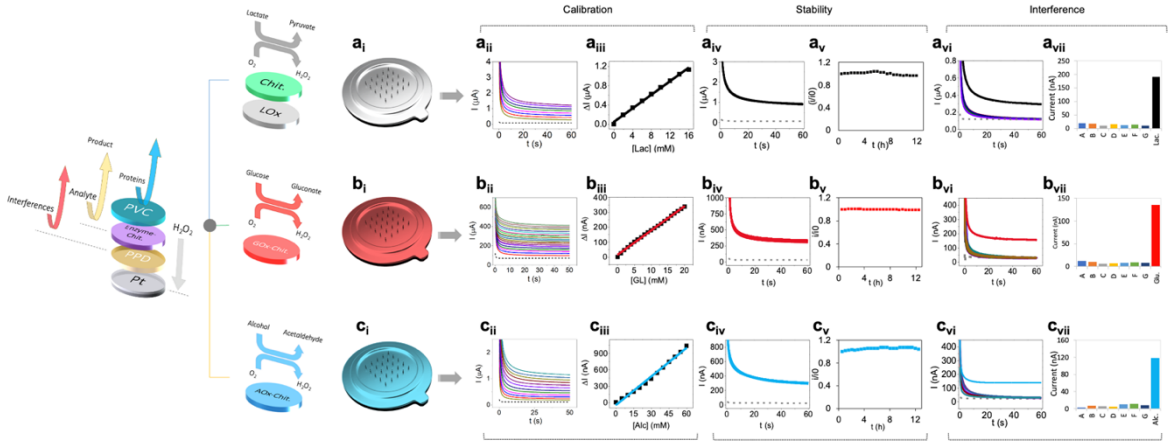

Figure 2. Extended Data 10. In-Vitro study of the sensors. a_{i-iii}. Amperometry calibration curves and the extrapolated linear response of the lactate sensor. a_{iv-v} Stability of the lactate sensor for 12 hours. a_{vi-vii}. Interference study of the lactate sensor in artificial solution upon adding (A) ascorbic acid (200 mM), uric acid (500 mM), acetaminophen (100 mM), tryptophan (500 mM), methionine (500 mM), and histidine (500 mM) from B to G, respectively. b_{i-iii}. Amperometry calibration curves and the extrapolated linear response of the glucose sensor. b_{iv-v} Stability of the lactate sensor for 12 hours. b_{vi-vii}. Interference study of the glucose sensor in artificial solution upon adding (A) ascorbic acid (200 mM), uric acid (500 mM), acetaminophen (100 mM), tryptophan (500 mM), methionine (500 mM), and histidine (500 mM) from B to G, respectively. c_{i-iii}. Amperometry calibration curves and the extrapolated linear response of the alcohol sensor. c_{iv-v} Stability of the lactate sensor for 12 hours. c_{vi-vii}. Interference study of the alcohol sensor in artificial solution upon adding (A) ascorbic acid (200 mM), uric acid (500 mM), acetaminophen (100 mM), tryptophan (500 mM), methionine (500 mM), and histidine (500 mM) from B to G, respectively.

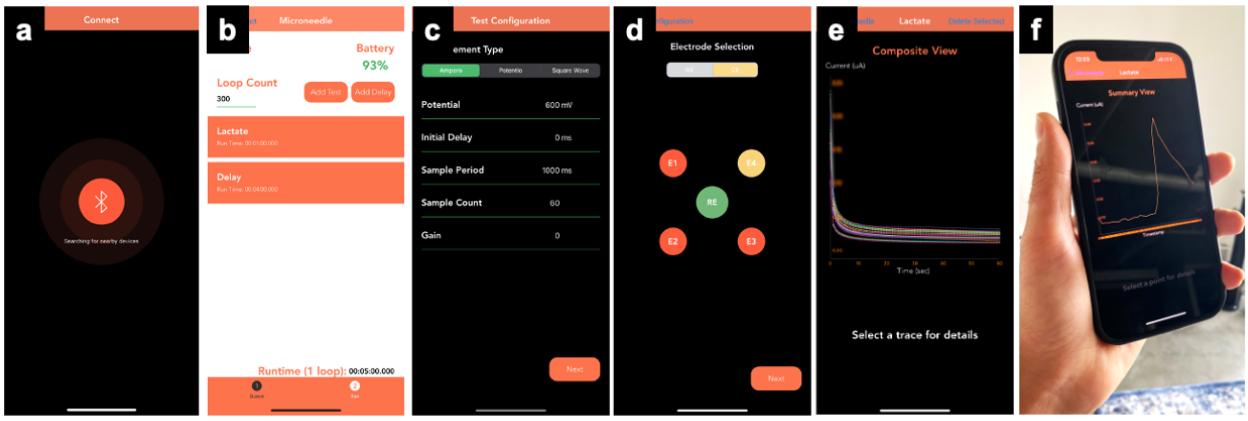

Figure 2. Extended Data 11. iOS App. a. Bluetooth connection page where the app searches for and connect to the sensor patch device. **b**. Test setup page in which the amperometry experiment, its time, delay interval between each test is defined. **c**. Individual test configuration page, where the test parameters are inserted. **d**. Electrode selection page where up to 4 sensors can be defined to operate independently. **e**. Composite view page, where all the amperometry results of a particular test is shown. **f**. Summary view page, where the sensing profile for over a particular testing duration is viewed.

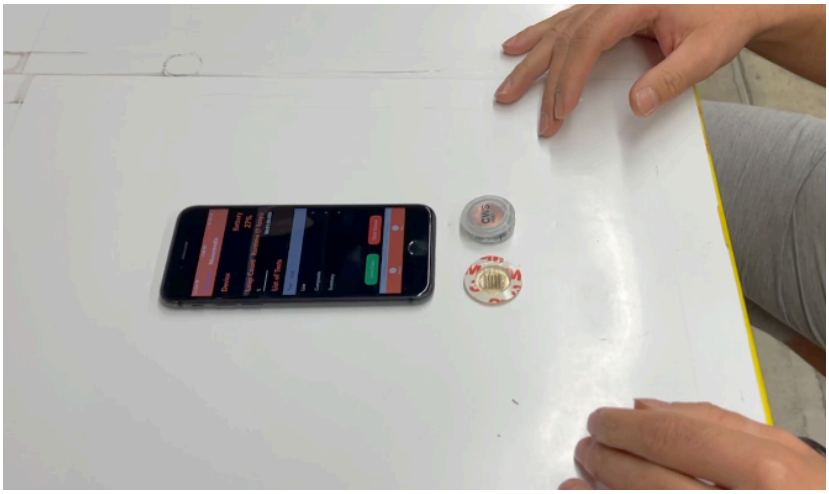

<u>Extended Data Video 2. 1.</u> Demonstration of the sensor disposable and reusable components being assembled and placed on the arm of a subject followed by a signal quality test.

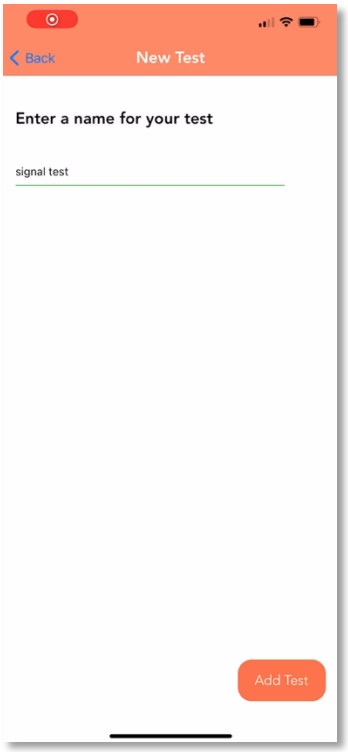

<u>Extended Data Video 2. 2</u>. Demonstration of the sensor's app. signal quality test immediately after applying the sensor to the skin of a subject.

Acknowledgement

Chapter 2, in part, and has been submitted for publication of the material, as it may appears in Nature, 2021, by Farshad Tehrani, Hazhir Teymourian, Brian Wuerstle, Jonathan Kavner, Ravi Patel, Allison Furmidge, Reza Aghavali, Christopher Brown, Fangyu Zhang, Kuldeep Mahato, Zhengxing Li, Abbas Barfidokht, Lu Yin, Paul Warren, Nickey Huang, Zina Patel, Patrick P. Mercier, Joseph Wang. The dissertation author was the primary investigator and author of this paper.

5. References

[1] J. Kim, A. S. Campbell, B. E. F. de Ávila, J. Wang, *Nat. Biotechnol.* **2019**, *37*, 389–406.

[2] J. Dunn, R. Runge, M. Snyder, *Per. Med.* **2018**, *15*, 429–448.

[3] J. Heikenfeld, A. Jajack, B. Feldman, S. W. Granger, S. Gaitonde, G. Begtrup, B. A. Katchman, *Nat. Biotechnol.* **2019**, *37*, 407–419.

[4] P. P. Samant, M. M. Niedzwiecki, N. Raviele, V. Tran, J. Mena-Lapaix, D. I. Walker, E. I. Felner, D. P. Jones, G. W. Miller, M. R. Prausnitz, *Sci. Transl. Med.* **2020**, *12*, eaaw0285.

[5] B. Q. Tran, P. R. Miller, R. M. Taylor, G. Boyd, P. M. Mach, C. N. Rosenzweig, J. T. Baca, R. Polsky, T. Glaros, *J. Proteome Res.* **2018**, *17*, 479–485.

[6] H. Teymourian, F. Tehrani, K. Mahato, J. Wang, *Adv. Healthc. Mater.* **2021**, *n/a*, 2002255.

[7] M. C. Brothers, M. Debrosse, C. C. Grigsby, R. R. Naik, S. M. Hussain, J. Heikenfeld, S. S. Kim, *Acc. Chem. Res.* **2019**, *52*, 297–306.

[8] A. Wiorek, M. Parrilla, M. Cuartero, G. A. Crespo, *Anal. Chem.* **2020**, DOI 10.1021/acs.analchem.0c02211.

[9] H. Y. Y. Nyein, M. Bariya, L. Kivimäki, S. Uusitalo, T. S. Liaw, E. Jansson, C. H. Ahn, J. A. Hangasky, J. Zhao, Y. Lin, T. Happonen, M. Chao, C. Liedert, Y. Zhao, L. C. Tai, J. Hiltunen, A. Javey, *Sci. Adv.* **2019**, DOI 10.1126/sciadv.aaw9906.

[10] A. J. Bandodkar, J. Wang, *Trends Biotechnol.* **2014**, *32*, 363–371.

[11] D. Zeevi, T. Korem, N. Zmora, D. Israeli, D. Rothschild, A. Weinberger, O. Ben-Yacov, D. Lador, T. Avnit-Sagi, M. Lotan-Pompan, J. Suez, J. A. Mahdi, E. Matot, G. Malka, N. Kosower, M. Rein, G. Zilberman-Schapira, L. Dohnalová, M. Pevsner-Fischer, R. Bikovsky, Z. Halpern, E. Elinav, E. Segal, *Cell* **2015**, *163*, 1079–1094.

[12] E. J. Topol, *Nat. Med.* **2019**, *25*, 44–56.

[13] A. K. Yetisen, J. L. Martinez-Hurtado, B. Ünal, A. Khademhosseini, H. Butt, *Adv. Mater.* **2018**, *30*, 1706910.

[14] T. Mishra, M. Wang, A. A. Metwally, G. K. Bogu, A. W. Brooks, A. Bahmani, A. Alavi, A. Celli, E. Higgs, O. Dagan-Rosenfeld, B. Fay, S. Kirkpatrick, R. Kellogg, M. Gibson, T. Wang, E. M. Hunting, P. Mamic, A. B. Ganz, B. Rolnik, X. Li, M. P. Snyder, *Nat. Biomed. Eng.* **2020**, *4*, 1208–1220.

[15] W. Gao, S. Emaminejad, H. Y. Y. Nyein, S. Challa, K. Chen, A. Peck, H. M. Fahad, H. Ota, H. Shiraki, D. Kiriya, D.-H. Lien, G. A. Brooks, R. W. Davis, A. Javey, *Nature* **2016**, *529*, 509–514.

[16] J. Heikenfeld, A. Jajack, J. Rogers, P. Gutruf, L. Tian, T. Pan, R. Li, M. Khine, J. Kim, J. Wang, J. Kim, *Lab Chip* **2018**, *18*, 217–248.

[17] J. Choi, R. Ghaffari, P. Gutruf, A. J. Bandodkar, S. Krishnan, J. A. Rogers, L. Tian, T. R. Ray, *Chem. Rev.* **2019**, *119*, 5461–5533.

[18] S. Emaminejad, W. Gao, E. Wu, Z. A. Davies, H. Yin Yin Nyein, S. Challa, S. P. Ryan, H. M. Fahad, K. Chen, Z. Shahpar, S. Talebi, C. Milla, A. Javey, R. W. Davis, *Proc. Natl. Acad. Sci.* **2017**, *114*, 4625–4630.

[19] A. J. Bandodkar, P. Gutruf, J. Choi, K. Lee, Y. Sekine, J. T. Reeder, W. J. Jeang, A. J. Aranyosi, S. P. Lee, J. B. Model, R. Ghaffari, C.-J. Su, J. P. Leshock, T. Ray, A. Verrillo, K. Thomas, V. Krishnamurthi, S. Han, J. Kim, S. Krishnan, T. Hang, J. A. Rogers, *Sci. Adv.* **2019**, *5*, eaav3294.

[20] H. Lee, T. K. Choi, Y. B. Lee, H. R. Cho, R. Ghaffari, L. Wang, H. J. Choi, T. D. Chung, N. Lu, T. Hyeon, S. H. Choi, D.-H. Kim, *Nat. Nanotechnol.* **2016**, *11*, 566–572.

[21] S. Imani, A. J. Bandodkar, A. M. V. Mohan, R. Kumar, S. Yu, J. Wang, P. P. Mercier, *Nat. Commun.* **2016**, *7*, 11650.

[22] A. J. Bandodkar, W. Jia, C. Yardımcı, X. Wang, J. Ramirez, J. Wang, *Anal. Chem.* **2015**, *87*, 394–398.

[23] L. Lipani, B. G. R. Dupont, F. Doungmene, F. Marken, R. M. Tyrrell, R. H. Guy, A. Ilie, *Nat. Nanotechnol.* **2018**, *13*, 504–511.

[24] C. E. Fairbairn, D. Kang, *Alcohol. Clin. Exp. Res.* **2019**, *43*, 2060–2069.

[25] I. Lee, D. Probst, D. Klonoff, K. Sode, *Biosens. Bioelectron.* **2021**, 113054.

[26] H. Teymourian, A. Barfidokht, J. Wang, *Chem. Soc. Rev.* **2020**, *49*, 7671–7709.

[27] World Economic Forum, *Top 10 Emerging Technologies of 2020*, **n.d.**

[28] T. M. Rawson, S. A. N. Gowers, D. M. E. Freeman, R. C. Wilson, S. Sharma, M. Gilchrist, A. MacGowan, A. Lovering, M. Bayliss, M. Kyriakides, P. Georgiou, A. E. G. Cass, D. O'Hare, A. H. Holmes, *Lancet Digit. Heal.* **2019**, *1*, e335–e343.

[29] H. Teymourian, C. Moonla, F. Tehrani, E. Vargas, R. Aghavali, A. Barfidokht, T. Tangkuaram, P. P. Mercier, E. Dassau, J. Wang, *Anal. Chem.* **2020**, *92*, 2291–2300.

[30] J. Gao, W. Huang, Z. Chen, C. Yi, L. Jiang, *Sensors Actuators, B Chem.* **2019**, *287*, 102–110.

[31] A. Wolf, K. Renehan, K. K. Y. Ho, B. D. Carr, C. V Chen, M. S. Cornell, M. Ye, A.

Rojas-Peña, H. Chen, *Biosens*. **2018**, *8*, DOI 10.3390/bios8040122.

[32] G. Yu, S. J. Yoo, S.-H. Lee, J. S. Kim, S. Jung, Y.-J. Kim, W. Y. Kim, S. M. Ryoo, *Acute Crit Care* **2019**, *34*, 126–132.

[33] K. Sakaguchi, K. Takeda, M. Maeda, W. Ogawa, T. Sato, S. Okada, Y. Ohnishi, H. Nakajima, A. Kashiwagi, *Diabetol. Int.* **2016**, *7*, 53–58.

[34] J. T. Sakai, S. K. Mikulich-Gilbertson, R. J. Long, T. J. Crowley, *Alcohol. Clin. Exp. Res.* **2006**, *30*, 26–33.

[35] L. L. J. Koppes, J. M. Dekker, H. F. J. Hendriks, L. M. Bouter, R. J. Heine, *Diabetes Care* **2005**, *28*, 719 LP – 725.

[36] K. L. Wolkowicz, E. M. Aiello, E. Vargas, H. Teymourian, F. Tehrani, J. Wang, J. E. Pinsker, F. J. Doyle III, M.-E. Patti, L. M. Laffel, E. Dassau, *Bioeng. Transl. Med.* **2021**, *6*, e10201.

[37] T. E. Jones, W. J. Pories, J. A. Houmard, C. J. Tanner, D. Zheng, K. Zou, P. M. Coen, B. H. Goodpaster, W. E. Kraus, G. L. Dohm, *Surgery* **2019**, *166*, 861–866.

Chapter 3. Sodium Monitoring for Hydration

Microneedle-based sensor for potentiometric detection of sodium: Toward measurement of interstitial fluid osmolality for real-time assessment of hydration status

1. Introduction

Maintaining optimal hydration is essential during exercise. To assess real-time hydration status, an ion-selective microneedle sensor capable of monitoring sodium in the interstitial fluid (ISF) is developed. The 3D printed hollow microneedles were packed with carbon paste and Ag/AgCl ink as solid-state transducers and integrated with a portable electrochemical analyser. The resulting microneedle system demonstrated high capability for continuous sodium measurement across normal physiological ISF concentrations of 135-145 mM with enhanced sensitivity and stability in artificial skin. The developed microneedle sensor empowers athletes to keep track of their hydration state in real-time and expands the scope of hydration monitoring by its multifunctional capabilities.

Real-time hydration monitoring is essential to assess performance and safety during strenuous physical activities. [1] When dehydration happens, replacement of key electrolytes becomes critical to maintain a normal cardiovascular function, thermoregulation, cognition, and exercise performance.[2] Meanwhile, overconsumption of fluids (especially sodium-free fluids such as water) in excess of sweat loss can lead to dilution of blood osmolality that could eventually cause electrolyte imbalances (i.e., hyponatremia, plasma [Na] < 135 mmol/L). [2]

The common measures of hydration status include body mass change, urine color, salivary markers, bioelectrical impedance, and plasma osmolality. Among these techniques, plasma

osmolality is considered as the most reliable indicator of both hypohydration (dehydration) and hyperhydration (overhydration). [2–4]

The plasma osmolality is maintained within a narrow range of 275–295 mOsm/kg. This is equivalent to the plasma sodium concentration of 135-145 mM, [5] with the estimated concentration cut-offs beyond 145 mM for dehydration, 135-145 mM for euhydration, and bellow 135 mM for overhydration.

Although plasma osmolality is a useful marker for hydration assessment, the need for blood sampling prevents its use as a non-invasive measure during exercise on the field. Additionally, the aforementioned health consequences of dehydration and overhydration during physical activity call for a need to accurately measuring acute changes in hydration status. Therefore, there is a significant demand for low-cost, wearable and non/minimally-invasive tools to replace the current expensive and bulky instruments and to accurately and continuously monitor acute changes in the hydration status during physical activities.[6,7]

Microneedle based sensor systems offer an attractive minimally invasive solution to measure ISF sodium (osmolality) as an alternative to plasma osmolality. Note that, as ISF and plasma are separated only by a capillary wall (permeable to small ions), their ionic compositions are essentially identical [8]. Therefore, sodium plays the main role to measure ISF osmolality, with other contributions from glucose and urea, Eq. 1:

(Eq. 1)

$$\text{ISF osmolality} = 2\,(\text{ISF [Na], mM}) + (\text{ISF [glucose] (mg/dl)}/18) + ([\text{ISF urea}]\ (\text{mg/dl})/2.8)$$

Electrochemical microneedle sensors, as an up-and-coming research shift in the field of wearable sensing, have significantly impacted the transdermal biosensing of analytes of clinical,

environmental and security importance, some of which includes glucose, [9–11] ketone, [12] nerve agents,[13] L-DOPA,[14] penicillin, [15] alcohol, [16] lactate, [17] and others [18,19] and can support continuous monitoring of athletes.

As for the potentiometric microneedles, the first example was reported by Miller et al., where an ion-selective microfluidic/microneedle platform for on-chip determination of potassium ions (K^+) was introduced.[20] In this study, a poly(methyl methacrylate) (PMMA) substrate consisting of a fluidic microchannel connects the microneedle system with an integrated three-electrode system on the microchannel itself. In another study, Parrilla et al. took a different strategy to target potassium and developed a wearable microneedle patch for intradermal potentiometric detection. [21] In this system, stainless-steel microneedles were fabricated and fixed in a flexible and stretchable PDMS substrate as a wearable device for ex-vivo determination of K^+. To the best of our knowledge, these are the only studies in literature that evaluated the application of microneedles for electrolyte (potassium) detection. Therefore, it's safe to assert that the field of microneedle technology possess significant potential toward development of potentiometric microneedles, especially for sodium monitoring. Existing class of electrochemical wearable devices for sodium detection includes skin-worn microfluidic chips, [22,23] a watch-format platform, [24] impedance-based conformal hydration sensors, [25,26] textile sensor, [27] and a sweat sensor belt [28]. Still, the current work is distinct from these previously reported wearable sodium sensors, by targeting the narrow sodium concentration range required to maintain plasma osmolality, as opposed to a wide concentration range with a high limit of quantification that is mainly demonstrated in these works.

In this study, we demonstrate the first example of an ISE microneedle for the detection of sodium. This study is aimed to detect ISF sodium within a certain range of ISF osmolality toward

assessment of the hydration status. In this work, 3D printed hollow microneedle sensors were employed to develop a sodium ion-selective electrode. For this purpose, the working sensor was packed with carbon paste transducers to develop an ISE, while Ag/AgCl ink was used to pack forming the sensor's reference electrode (Fig. 1A). To modify the developed microneedles, different cocktails for ISE and reference electrodes were cast on the electrode surfaces. Figures 1A and B illustrate the fabrication steps and multilayer surface modifications, along with a close-view optical image of the developed microneedle sensor. The developed fabrication system thus provides a simple way of developing ISE microneedles.

2. Experimental Section

ISE Strip Fabrication: A semi-automatic MMP-SPM printer machine (Speedline Technologies, Franklin, MA) was used to fabricate screen printed electrodes. A stainless-steel stencil developed using AutoCAD software (Autodesk, San Rafael, CA) was employed to print these electrodes on a flexible polyethylene terephthalate (PET) substrate. For this purpose, an Ag/AgCl conductive ink was used to first print the reference electrode, followed by printing the carbon working electrode (Figure 2A). To cure the printed electrodes, after each printing step, the sensor was kept at 85 °C for 30 min.

Microneedle Fabrication: Hollow microneedle patches with an inner dimension of 500 μm, the height of 1.5 mm and the patch base diameter of 1.5 cm were designed using Fusion 360 (by Autodesk). Designed 3D microneedle patches were then printed using a desktop 3D printer (Photon 3D printer by Anycubic) in bulk. Skin color Ultraviolet (UV) sensitive resin by Anycubic was used for printing the microneedles. After 3D printing was complete, the 3D printed pieces were immersed in an Isopropyl alcohol (IPA) tank and sonicated for 15 minutes to ensure complete rinsing of the uncured resin from the 3D printed pieces. Lastly, all 3D printed pieces were further

cured by exposure to UV light with 405 nm wavelength at 36W in the room temperature for 30 minutes, Figure 1A.

The next step was to integrate sensor electrodes and a microneedle patch. To do that, two stainless steel 316L wires (OD=0.3mm) were inserted to the microneedle holes and glued to the backside of the microneedle using an epoxy leaving 1mm of the wire exposed for electrical contact with carbon paste (CP) and Ag/AgCl ink, Figure 1A. Two hollow microneedles were then packed with carbon paste (60% graphite, 30% mineral oil) and Ag/AgCl ink. Lastly, the entire microneedle was cured at 85 °C for 30 minutes and then was ready for further functionalization steps, Figure 1B.

Electrode modification: Sodium selective membrane was prepared by formulating a cocktail solution that contains the following components: 1% sodium ionophore X, 0.6% Na-TFPB, 33% PVC and 66.4% o-NPOE. All components were mixed and dissolved in 660 µL tetrahydrofuran (THF). The reference cocktail was also prepared by dissolving 78.1 mg of PVB and 50 mg NaCl in 1 mL methanol. The Na^+ selective membrane on the microneedle was prepared by drop-casting 2.25 µL of the ISE cocktail on the electrode surface. For the reference electrode, also 2.25 reference cocktail was cast on the Ag/AgCl surface followed by 0.75 µL of aqueous-based polyurethane (PU). The sensors were allowed to dry overnight. Regarding the ISE strips (used for optimization studies) the same procedure was repeated. However more cocktail volume of 5 µL for ISE and 3 µL for reference electrodes were cast on each surface. Conditioning of sensors was performed in 100 mM sodium chloride solution for one hour before the OCP measurement.

OCP Measurement: A Sensit Smart potentiostat (PalmSens BV, The Netherlands), controlled by PSTrace software (version 5.7) was used for all potentiometric experiments. OCP

(open circuit potential) measurement was performed between the two microneedles of ISE and reference in 300 µL NaCl solution and a diverse volume of NaCl solution was spiked to perform the calibration studies. DI water was used to prepare all NaCl solutions.

Skin-Mimicking Phantom Gel Experiments: To prepare an agarose phantom gel as a skin-mimicking model, 60 mg of agarose gel (0.6 %) dissolved in 10 ml of DI water was heated at 200 °C while stirring for 10 min. The clear solution was then transferred into a circled-shaped mold to form a solidified gel. To perform potentiometric studies, ISE microneedle was pressed through the gel, and then a different amount of NaCl solution was spiked on the gel and allowed 10 min to completely distributed throughout the gel.

3. Results & Discussions

Development of ISE microneedle-based system

The ISF osmolality is majorly regulated by its sodium content. Thus, to measure ISF sodium, we took the first step by developing an ISE microneedle-based sensing system for Na^+ detection, which eventually can help to assess the hydration status of the individual. For this purpose, two hollows 3-printed microneedle-based system (500 μm i.d.) was developed consisting of an ISE (a packed carbon paste transducer), a reference electrode (a packed Ag/AgCl ink) and their corresponding reagent layers (Fig. 1A & B). After developing microneedles, a small portable electrochemical analyser (Fig. 1C) of dimensions (43 x 25 x 11 mm) was integrated with the developed microneedle-based system for potentiometric studies, which has all been performed in vitro conditions. Since the plasma osmolality lies in a restricted narrow range (Fig. 1D) of Na^+ concentrations *i.e.* 135-145 mM, the microneedle-based potentiometric system has been specifically designed for sensitive and reproducible operation in this range. Fig. 1E shows a

representative potentiometric response for the developed microneedle with a notable capability of detecting diverse concentration increments of 20 mM, 10 mM, and 5 mM.

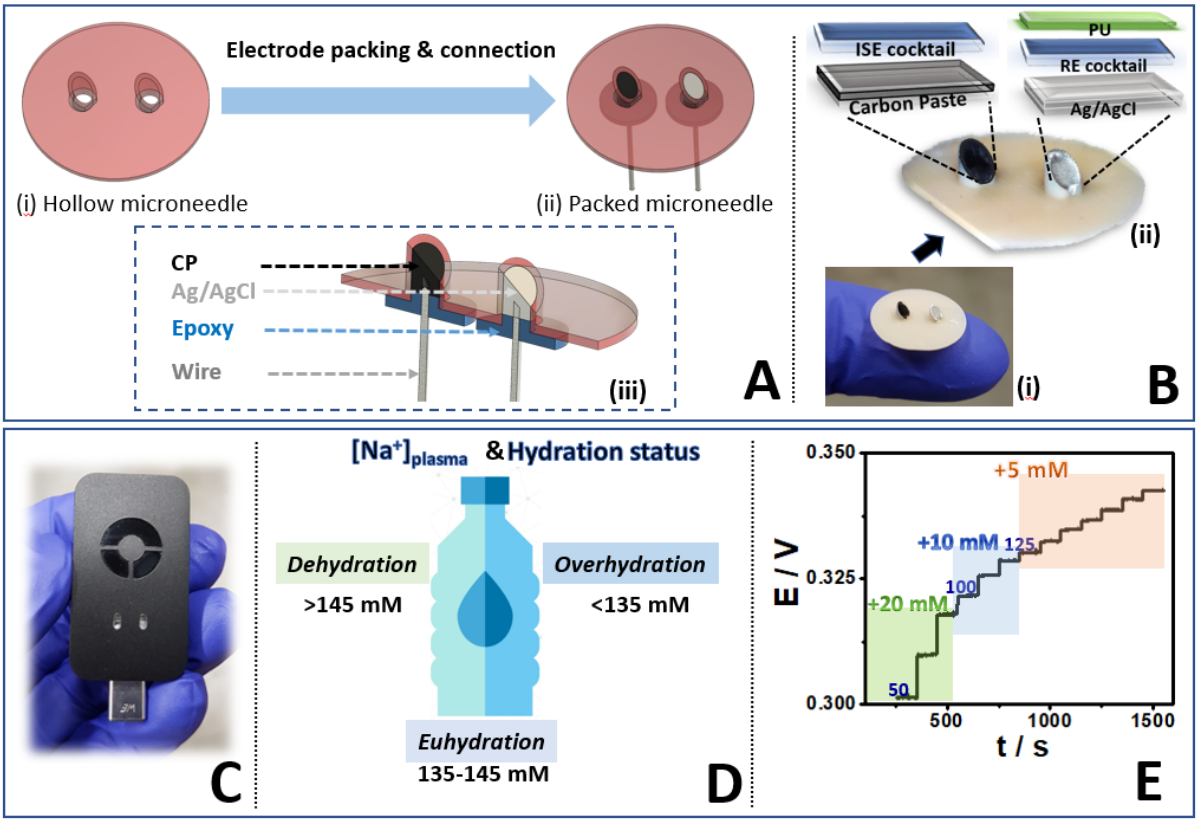

Figure 3. 1. Schematic representation of the Na^+ ISE Microneedle sensor. A, Stepwise demonstration of microneedle fabrication and microneedle cross-section. Photograph of fabricated MN assembly showing the multiple layers. **B**, Photograph of fabricated microneedle assembly showing the modified multiple layers. **C**, A portable electrochemical analyzer for the detection of Na^+ in DI water. **D**, Relationship between Na^+ concentrations and hydration status in ISF. **E**, Response of microneedle sensor in varying concentrations of Na^+ from 50 to 155 mM in DI water.

ISE optimization towards ISF sodium range

Due to the presence of multiple different electrolytes in the ISF (such as K^+ as the main interference for Na^+ sensor), it is required to tune and optimize the selectivity of the ISE microneedle toward Na^+ sensing. Our optimization studies demonstrated that the type of

plasticizers in the ISE cocktail can highly impact the ISE selectivity. Accordingly, two different plasticizers of o-NPOE and DOS were employed to prepare ISE cocktails.

To facilitate the optimization studies, ISE strips were firstly used instead of ISE microneedles. In the first step, distinct ISE strips systems were modified with different cocktails containing o-NPOE and DOS and the associated sensors were tested against Na^+ and K^+ containing salt solutions. Fig. 2A and fig. 2B show the potentiometric responses for both the systems, where o-NPOE-related membrane electrode system offers a distinct potentiometric response toward Na^+ detection with a negligible response for K^+ (Na^+ slope: 55±1.5 mV vs. K^+ slope: 1.5±0.5 mV) compared with that of DOS-membrane sensor (Na^+ slope: 58±2 mV vs. K^+ slope: 20±2 mV). Therefore, the o-NPOE plasticizer was used for further potentiometric studies. Besides, taking the narrow range of Na^+ concentration for hydration assessment into account, the sensitivity of the ISE system had also been precisely tuned. For that, different ratios of the ISE cocktail components and the loading amount on the electrode surface were also optimized. The results demonstrated that the ISE cocktail with 1% sodium ionophore X, 0.6% Na-TFPB, 33% PVC and 66.4% o-NPOE and the loading amount of 5 μL per 0.04 cm^2 are the ideal cocktail composition and cocktail loading on the surface, respectively. By tuning the sensor modification with all optimized conditions of plasticizer type, cocktail composition and cocktail loading amount, the ISE strip showed enhanced sensitivity toward a lower limit of quantifications of 10 and 5 mM. One representative calibration graph showing a 10 mM Na^+ increment addition with an average Nernstian slope of 63 mV/decade is shown in Fig. 2C.

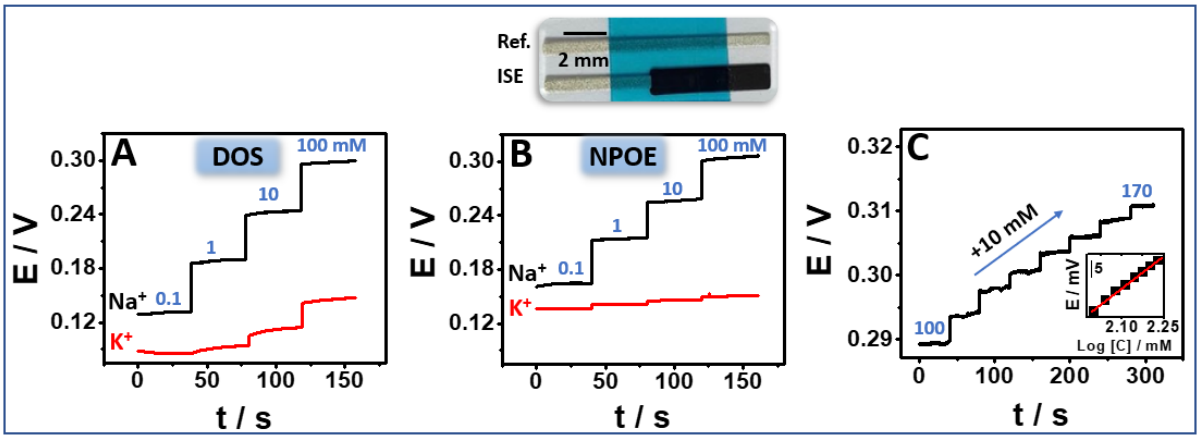

Figure 3. 2. Optimization of Na^+ Specific ISE cocktail using the strip. Comparison of plasticizers, (**A**) DOS and (**B**) NPOE for Na^+ detection using a strip-based (inset) sensing system. Blackline represents Na^+ response and the red line shows the K^+ response. (**C**) Optimization study for Na^+ specific ISE cocktail toward improving sensitivity in the concentration range 100 to 170 mM. A dose-dependent study with a 10 mM increment and showing improved mobility of the sensors for the detection of lower increments of 10 mM. The final cocktail includes Sodium Ionophore: 1 mg, PVC: 33 mg, NPOE 65.45 mg, and Na-TFPB 0.55 mg. All were dissolved in 650 μL tetrahydrofuran (THF).

ISE Microneedle Evaluation Studies

By implicating all optimized conditions and fabricating ISE microneedles, comprehensive and critical evaluation of the sensing system toward the analytical performance assessments *viz.* sensitivity, selectivity, reproducibility, and stability were performed (Fig. 3). As discussed before, the main characteristic of the Na^+ sensing device toward hydration assessment should be its capability in detecting low concentration changes of Na^+ concentrations in ISF. The developed ISE microneedle was vigorously challenged with diverse Na^+ concentration spikes. As presented in Fig. 3A, it is evident that the ISE sensor is responding sensitively to Na^+ concentrations at different additions of 10 mM, 20 mM and 30 mM with a distinct sensitivity, a fast response time (t_{95}, <10 s) and an average Nernstian slope of 61 mV/decade. Fig. 3B depicts the dynamic response of ISE microneedle for 5 mM Na^+ additions within the linear range of response (100-150 mM) and with a sensitivity of 63 mv/decade. It is worth mentioning that the obtained linear range covers almost

all concentrations of Na^+ in normal and stressed physiological hydration levels and this is well-aligned with the required sensitivity to assess the status of hydration. Obtaining such sensitivity for the ISE microneedle is considered as a significant achievement toward assessing the hydration status. Each 5 mM concentration difference in the Na^+ plasma within its normal range (135-145 mM), which interferes fluid-electrolyte balance, may result in a wide range of symptoms of no noticeable disturbance (125-135 mM), mild to more severe damages (<125 mM) and life-threatening consequences (<120 mM). [5] To evaluate the ability of the microneedle for continuous measurements, the response of the microneedle-based system was recorded in increasing concentrations of Na^+ with no pause during spikes. As shown in Fig. 3C, a wide linear range of response (from 50 to 150 mM) with a sensitivity of 60 mV/decade was obtained despite having the evident noises during the time of spiking. Following this, we have also tested the interferences of K^+ toward the developed microneedle-based system, where we spiked 20 mM of K^+ just after every spiking of the Na^+. Figure 3D displays OCP measurements of Na^+ ISE microneedle for alternating 20 mM spikes of sodium and potassium. Interestingly, no significant increase in the signal was seen upon the K^+ spike which indicates the negligible ion interference (less than 10% of the response) in a mixed solution and the quick response of Na^+ even in the presence K^+.

The reversibility of the ISE microneedle was verified by performing the potentiometric response for increasing and decreasing concentrations of sodium for three consecutive changes of 100, 125 and 150 mM in three complete cycles (Figure 3E). The ISE sensor exhibited a reversible signal with an average sensitivity of 62 mV/decade. This indicates that the developed microneedle-based system can be able to detect the sudden fluctuation of the Na^+ efficiently. After these studies, we have tested the voltage stability of the microneedle-based system and recorded OCP over 500

s at two distinct concentrations of spiked Na^+. The ISE sensor demonstrated negligible potential drift of 0.3±0.1 mV for each concentration for 500 s OCP recording (Fig. 3F) which indicates the sensor probe is stable for longer operations.

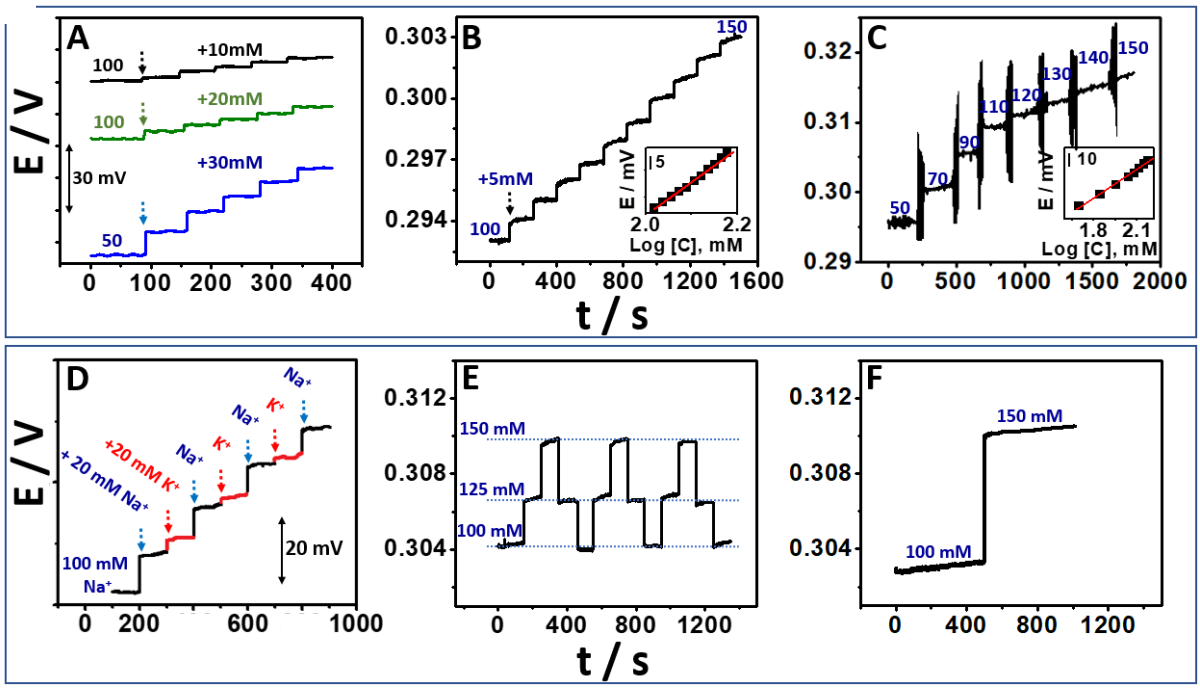

Figure 3. 3. The response of the fabricated ISE microneedle to Na^+. A, dose-dependent responses of fabricated MN sensors obtained at a different increment of Na^+ concentrations of 10, 20, and 30 mM. **B**, Dose-dependent response of fabricated MN sensor obtained on an increase of 5 mM Na^+ showing a distinct increment in potential. **C**, Responses obtained using the carbon-based fabricated MN for continuous measurement of Na^+ (0.1mM to 200 mM) with no pause (continuous OCP measurement). **D**, responses obtained using the carbon-based MN for Na^+ detection (100 mM to 180 mM) in the presence of KCl. **E**, the carryover responses of fabricated carbon-based MN toward Na^+ detection between 100 mM to 150 mM. **F**, the response obtained from stability test using carbon-based MN toward Na^+ detection showing the probe is stable over 500 seconds.

Further, the detection capability of the ISE microneedle-based system was evaluated in the skin tissue-mimicking agarose-based phantom gel model (Fig. 4A). For this purpose, the sensor system was penetrated on the synthesized phantom gel and the performance was recorded after spiking the various concentrations of Na^+. The dose-dependent Na^+ response (110, 130 and 150 mM) is shown in Fig. 4B. The clear and distinct increment in the potential of Na^+ suggests that the

sensor system is highly responsive in skin-mimicking settings. Thereafter, the stability of the sensor was tested in such settings and showed the voltage stability of the inserted microneedle over 500 s. The obtained voltage response was found with a negligible potential drift of 0.2±0.1 mV for each concentration during 500 s (Fig. 4C). Such an attractive performance in the tissue-mimicking model suggests significant promise for potential on-body monitoring.

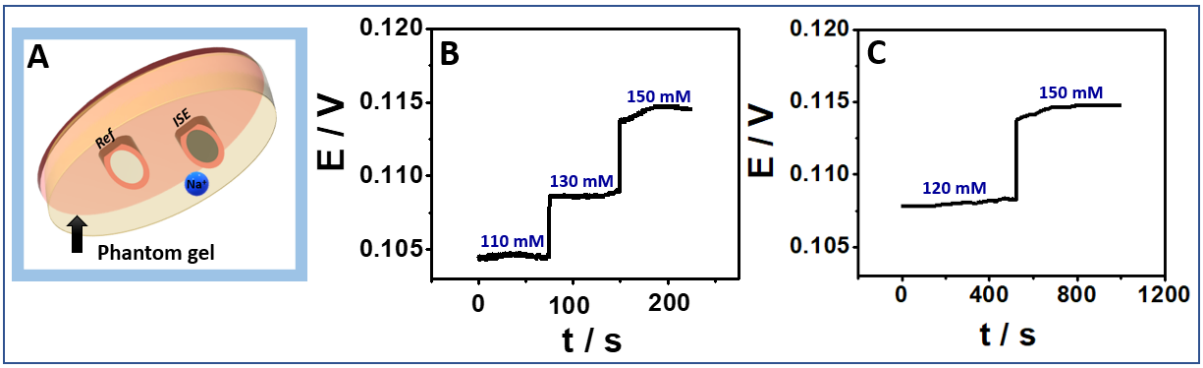

Figure 3. 4. Na^+ detection in phantom gel (0.4 %agarose). A, schematic representation of the inserted microneedle in a phantom gel. **B**, **the** response obtained from the dose-dependent Na^+ addition at the phantom gel environment. **C**, the response obtained from stability test toward Na^+ detection in phantom gel showing the developed carbon-based MN probe is stable over 500 seconds.

Concluding from all standard addition experiments performed by ISE microneedle-based system, the optimized Na^+ ISE microneedle has demonstrated the ability to detect concentration changes of 5, 10 mM, 20 mM, and 30 mM that are equivalent to 1.2 (±0.1) mV, 2.8 (±0.2) mV, 4.5 (±0.4) mV and 6.5 (±0.4) mV change in the OCP measurements. This indicates that the ISE microneedle can satisfy the need as a sensitive sensing tool to measure ISF osmolality.

4. Conclusion

A microneedle-based hydration sensor was developed for real-time monitoring of Na^+ concentrations, which can measure the physiologically relevant range in ISF. To the best of our

knowledge, this developed system is the first demonstration of low-cost Na^+ determination that consists of 3D-printed microneedle with carbon and Ag/AgCl pastes as solid transducers assembly. The results obtained in this study suggest that the developed ISE microneedle can be used to monitor ISF osmolality and thereby the hydration status. This developed sensor would be beneficial for military personnel to provide athletic performance awareness and can potentially assist the cosmetic scientists by diagnosing skin diseases.

Acknowledgements

Chapter 3 is based, in part, on the material as it may appear in Analytical chemistry, 2022, by Abbas Barfidokht, Farshad Tehrani, and Joseph Wang. The dissertation author was the primary co-investigator and co-author of this paper.

5. References

[1] L.E. Armstrong, Assessing Hydration Status: The Elusive Gold Standard, J. Am. Coll. Nutr. 26 (2007) 575S-584S. https://doi.org/10.1080/07315724.2007.10719661.

[2] S.N. Sawka MN, Burke LM, Eichner ER, Maughan RJ, Montain SJ, Exercise and Fluid Replacement, Med. Sci. Sport. Exerc. 39 (2007) 377–390. https://doi.org/10.1249/mss.0b013e31802ca597.

[3] L.B. Baker, J.A. Lang, W. Larry Kenney, Change in body mass accurately and reliably predicts change in body water after endurance exercise, Eur. J. Appl. Physiol. 105 (2009) 959–967. https://doi.org/10.1007/s00421-009-0982-0.

[4] S.M. Shirreffs, Markers of hydration status, Eur. J. Clin. Nutr. 57 (2003) S6–S9. https://doi.org/10.1038/sj.ejcn.1601895.

[5] B. Murray, J. Stofan, E.R. Eichner, Hyponatremia in athletes, Sport. Sci. 16 (2003). https://www.gssiweb.org/sports-science-exchange/article/sse-88-hyponatremia-in-athletes.

[6] T. Ray, J. Choi, J. Reeder, S.P. Lee, A.J. Aranyosi, R. Ghaffari, J.A. Rogers, Soft, skin-

interfaced wearable systems for sports science and analytics, Curr. Opin. Biomed. Eng. 9 (2019) 47–56. https://doi.org/10.1016/j.cobme.2019.01.003.

[7] J. Choi, R. Ghaffari, L.B. Baker, J.A. Rogers, Skin-interfaced systems for sweat collection and analytics, Sci. Adv. 4 (2018) eaar3921. https://doi.org/10.1126/sciadv.aar3921.

[8] R.M. Berne, M.N. Levy, B.A. Koeppen, Bruce M. Stanton, Physiology, Fourth Edi, Mosby Inc, 1998.

[9] A. Caliò, P. Dardano, V. Di Palma, M.F. Bevilacqua, A. Di Matteo, H. Iuele, L. De Stefano, Polymeric microneedles based enzymatic electrodes for electrochemical biosensing of glucose and lactic acid, Sensors Actuators B Chem. 236 (2016) 343–349. https://doi.org/10.1016/j.snb.2016.05.156.

[10] A. El-Laboudi, N.S. Oliver, A. Cass, D. Johnston, Use of Microneedle Array Devices for Continuous Glucose Monitoring: A Review, Diabetes Technol. Ther. 15 (2013) 101–115. https://doi.org/10.1089/dia.2012.0188.

[11] S. Sharma, Z. Huang, M. Rogers, M. Boutelle, A.E.G. Cass, Evaluation of a minimally invasive glucose biosensor for continuous tissue monitoring, Anal. Bioanal. Chem. 408 (2016) 8427–8435. https://doi.org/10.1007/s00216-016-9961-6.

[12] H. Teymourian, C. Moonla, F. Tehrani, E. Vargas, R. Aghavali, A. Barfidokht, T. Tangkuaram, P.P. Mercier, E. Dassau, J. Wang, Microneedle-Based Detection of Ketone Bodies along with Glucose and Lactate: Toward Real-Time Continuous Interstitial Fluid Monitoring of Diabetic Ketosis and Ketoacidosis, Anal. Chem. 92 (2020) 2291–2300. https://doi.org/10.1021/acs.analchem.9b05109.

[13] R.K. Mishra, K.Y. Goud, Z. Li, C. Moonla, M.A. Mohamed, F. Tehrani, H. Teymourian, J. Wang, Continuous Opioid Monitoring along with Nerve Agents on a Wearable Microneedle Sensor Array, J. Am. Chem. Soc. 142 (2020) 5991–5995. https://doi.org/10.1021/jacs.0c01883.

[14] K.Y. Goud, C. Moonla, R.K. Mishra, C. Yu, R. Narayan, I. Litvan, J. Wang, Wearable Electrochemical Microneedle Sensor for Continuous Monitoring of Levodopa: Toward Parkinson Management, ACS Sensors. 4 (2019) 2196–2204. https://doi.org/10.1021/acssensors.9b01127.

[15] T.M. Rawson, S.A.N. Gowers, D.M.E. Freeman, R.C. Wilson, S. Sharma, M. Gilchrist, A. MacGowan, A. Lovering, M. Bayliss, M. Kyriakides, P. Georgiou, A.E.G. Cass, D. O'Hare, A.H. Holmes, Microneedle biosensors for real-time, minimally invasive drug monitoring of phenoxymethylpenicillin: a first-in-human evaluation in healthy volunteers, Lancet Digit. Heal. 1 (2019) e335–e343. https://doi.org/10.1016/S2589-7500(19)30131-1.

[16] A.M.V. Mohan, J.R. Windmiller, R.K. Mishra, J. Wang, Continuous minimally-invasive alcohol monitoring using microneedle sensor arrays, Biosens. Bioelectron. 91 (2017) 574–579. https://doi.org/10.1016/j.bios.2017.01.016.

[17] P. Bollella, S. Sharma, A.E.G. Cass, R. Antiochia, Microneedle-based biosensor for minimally-invasive lactate detection, Biosens. Bioelectron. 123 (2019) 152–159. https://doi.org/10.1016/j.bios.2018.08.010.

[18] L. Ventrelli, L. Marsilio Strambini, G. Barillaro, Microneedles for Transdermal Biosensing: Current Picture and Future Direction, Adv. Healthc. Mater. 4 (2015) 2606–2640. https://doi.org/10.1002/adhm.201500450.

[19] S. Sharma, A. Saeed, C. Johnson, N. Gadegaard, A.E. Cass, Rapid, low cost prototyping of transdermal devices for personal healthcare monitoring, Sens. Bio-Sensing Res. 13 (2017) 104–108. https://doi.org/10.1016/j.sbsr.2016.10.004.

[20] P.R. Miller, X. Xiao, I. Brener, D.B. Burckel, R. Narayan, R. Polsky, Microneedle-based transdermal sensor for on-chip potentiometric determination of K+, Adv. Healthc. Mater. (2014). https://doi.org/10.1002/adhm.201300541.

[21] M. Parrilla, M. Cuartero, S. Padrell Sánchez, M. Rajabi, N. Roxhed, F. Niklaus, G.A. Crespo, Wearable All-Solid-State Potentiometric Microneedle Patch for Intradermal Potassium Detection, Anal. Chem. 91 (2019) 1578–1586. https://doi.org/10.1021/acs.analchem.8b04877.

[22] J.R. Sempionatto, A. Martin, L. García-Carmona, A. Barfidokht, J.F. Kurniawan, J.R. Moreto, G. Tang, A. Shin, X. Liu, A. Escarpa, J. Wang, Skin-worn Soft Microfluidic Potentiometric Detection System, Electroanalysis. 31 (2019) 239–245. https://doi.org/10.1002/elan.201800414.

[23] S. Anastasova, B. Crewther, P. Bembnowicz, V. Curto, H.M. Ip, B. Rosa, G.-Z. Yang, A

wearable multisensing patch for continuous sweat monitoring, Biosens. Bioelectron. 93 (2017) 139–145. https://doi.org/10.1016/j.bios.2016.09.038.

[24] T. Glennon, C. O'Quigley, M. McCaul, G. Matzeu, S. Beirne, G.G. Wallace, F. Stroiescu, N. O'Mahoney, P. White, D. Diamond, 'SWEATCH': A Wearable Platform for Harvesting and Analysing Sweat Sodium Content, Electroanalysis. 28 (2016) 1283–1289. https://doi.org/10.1002/elan.201600106.

[25] S. Yao, A. Myers, A. Malhotra, F. Lin, A. Bozkurt, J.F. Muth, Y. Zhu, A Wearable Hydration Sensor with Conformal Nanowire Electrodes, Adv. Healthc. Mater. 6 (2017) 1601159. https://doi.org/10.1002/adhm.201601159.

[26] X. Huang, W.-H. Yeo, Y. Liu, J.A. Rogers, Epidermal Differential Impedance Sensor for Conformal Skin Hydration Monitoring, Biointerphases. 7 (2012) 52. https://doi.org/10.1007/s13758-012-0052-8.

[27] W. He, C. Wang, H. Wang, M. Jian, W. Lu, X. Liang, X. Zhang, F. Yang, Y. Zhang, Integrated textile sensor patch for real-time and multiplex sweat analysis, Sci. Adv. 5 (2019) eaax0649. https://doi.org/10.1126/sciadv.aax0649.

[28] B. Schazmann, D. Morris, C. Slater, S. Beirne, C. Fay, R. Reuveny, N. Moyna, D. Diamond, A wearable electrochemical sensor for the real-time measurement of sweat sodium concentration, Anal. Methods. 2 (2010) 342. https://doi.org/10.1039/b9ay00184k.

Chapter 4. Hazard Chemical Monitoring

Continuous Opioid Monitoring along with Nerve Agents on a Wearable Microneedle Sensor Array

1. Introduction

There are urgent needs for sensing devices capable of distinguishing between episodes of opioid overdose and nerve agent poisoning. This work presents a wearable microneedle sensor array for minimally-invasive continuous electrochemical detection of opioid (OPi) and organophosphate (OP) nerve agents on a single patch platform. The new multi-modal microneedle sensor array relies on unmodified and organophosphorus hydrolase (OPH) enzyme- modified carbon paste (CP) microneedle electrodes for square wave voltammetric (SWV) detection of the fentanyl and nerve agent targets, respectively. Such real-time simultaneous sensing provides distinct unique information, along with attractive analytical performance, including high sensitivity, selectivity, and stability, for real-time on-body OPi-OP analysis. The patch represents the first sensing device capable of continuously monitoring fentanyl down to the nanomolar level through a nanomaterial-based multi-layered surface architecture. Applicability of the sensor array towards opioids screening is demonstrated for morphine and norfentanyl. Successful OPi-OP detection conducted in a skin-mimicking phantom gel demonstrates the suitability of the device for rapid on-body sensing. Such progress towards continuous minimally-invasive transdermal analysis of drugs of abuse and nerve agents holds promise for rapid countermeasures for protecting soldiers, civilians, and healthcare personnel.

The United States is experiencing a major drug overdose crisis which represents an extremely serious health concern. In particular, the use of fentanyl– the dominant synthetic opioid

with high potency than morphine[1–3]- can cause rapid cessation of breathing (apnea), hypoxemic/hypercarbic respiratory failure, and death.[4] There are also growing concerns regarding the potential use of opioids by terrorists and others in civilian settings[5]. For example, the use of fentanyl drug during 2002 hostage situation in Moscow resulted in 125 deaths.[6–8] These opioid threats can be absorbed through the skin and cross- dermal membranes to reach body fluids.[9,10] Likewise, dermal exposure of nerve agents will also lead to emergency situations. Often, the symptoms of opioid overdose may not easily be diagnosed and distinguished from those of nerve agents poisoning due to similar effects. As such, there are urgent demands for a rapid identification of exposure to such unknown chemical threats towards a timely lifesaving medical intervention.[11]

Wearable sensors have the potential to revolutionize the field of drug addiction by providing point-of-need rapid detection.[12] Our group has recently been involved in the development of wearable sensors for nerve agents and opioids.[13–15] While these early devices provide valuable information for on-the-spot field detection of suspicious powders, the continuous post-exposure on-body tracking of these threats has not been explored.

Herein, we demonstrate the first example of a minimally- invasive wearable microneedle sensor array for simultaneous detection of fentanyl and OP nerve agents on a single patch platform. Microneedles have recently gained tremendous attention due to their ability to monitor continuously a wide range of clinically important analytes.[16–23] The microneedle array was designed for distinguishing between episodes of opioid overdose and nerve agent poisoning. The microneedle array was constructed by using hollow microneedle working electrodes (WEs) filled with the CP transducers. As illustrated in Figure 1A, direct voltammetric detection of fentanyl was

carried out on WE1, involving an oxidative dealkylation of the piperidine tertiary amine and norfentanyl formation which displays a unique single peak at +0.7V, and additional distinct peaks upon repetitive scans. The nerve agents sensing was performed at the neighboring microneedle electrode (WE2) using methyl paraoxon (MPOx) as a model threat, relying on an OPH biocatalytic hydrolysis reaction along with the SWV detection of the enzymatically generated p-nitrophenol through its anodic oxidation. Figure 1B illustrates schematics of such simultaneous minimally-invasive OPi-OP detection along with wirelessly transmitted data to a smart device. Figures 1C-E present close-view optical and SEM images of the microneedle array. Three hollow microneedles (WE1, WE2 and CE) were packed with CP while the fourth one was embedded with Ag/AgCl wire reference electrode (RE). Such new microneedle sensor array thus offers a simple, on-body multiplexed sensing of the two major chemical threats, with continuous access to rapid distinct analytical information.

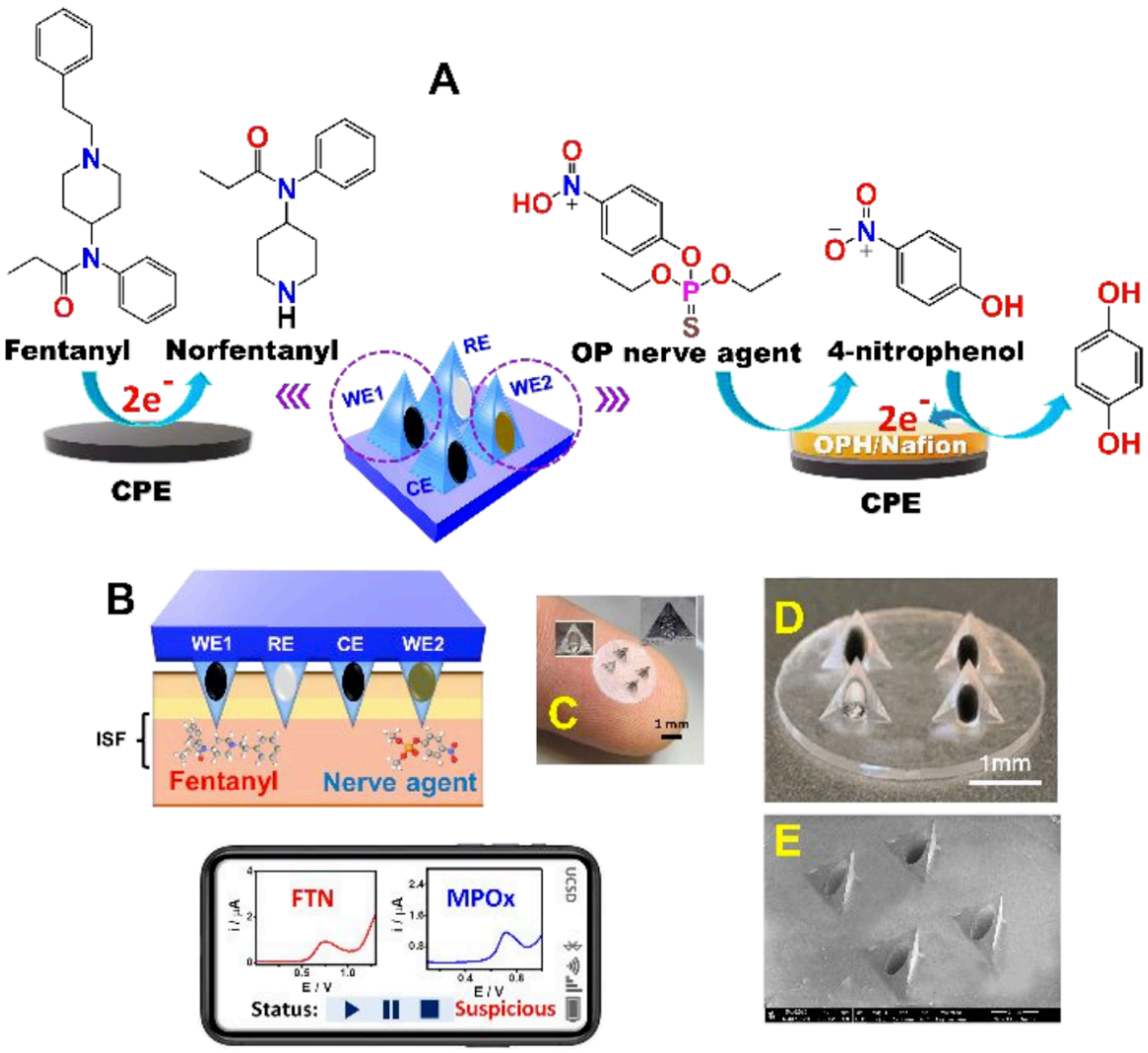

Figure 4. 1. Microneedle sensor array for detecting opioids and nerve agents. A. Schematics of fentanyl and nerve agent reactions at WE1 and WE2, respectively. B. Schematic of microneedle sensor array for simultaneous minimally invasive dual-threat detection, along with wireless data transmission to the mobile device. C, D. Optical images of the microneedle sensor array SEM image of the 4-hollow microneedle sensors array.

Figure 4. 2. Performance of the microneedle opioid sensor in artificial interstitial fluid (ISF) A. Scheme showing the microneedle fentanyl sensor. B. SWVs for fentanyl, 10-200μM in 10μM increments (a-t), inset: corresponding calibration plot. C. Stability of the PVC-coated microneedle toward 50μM fentanyl; 40 measurements recorded at 5min intervals. Inset: relative current change. D. CSWV response of 30μM fentanyl; repetitive forward and backward scans (n=5). E. Voltammograms of morphine oxidation over 20-140μM range; inset shows the linear correlation of morphine concentrations and oxidation currents at +0.2V. F. Simultaneous CSWV detection of fentanyl and morphine (fentanyl concentration: 50μM; morphine concentrations: 20, 40, 60μM). G. Forward CSWV scans for increasing concentrations of norfentanyl, 40-400μM in 40μM increments; inset: calibration plot. H. Backward-reverse voltammetric scans of norfentanyl (40-400μM) and the corresponding calibration plot (inset)

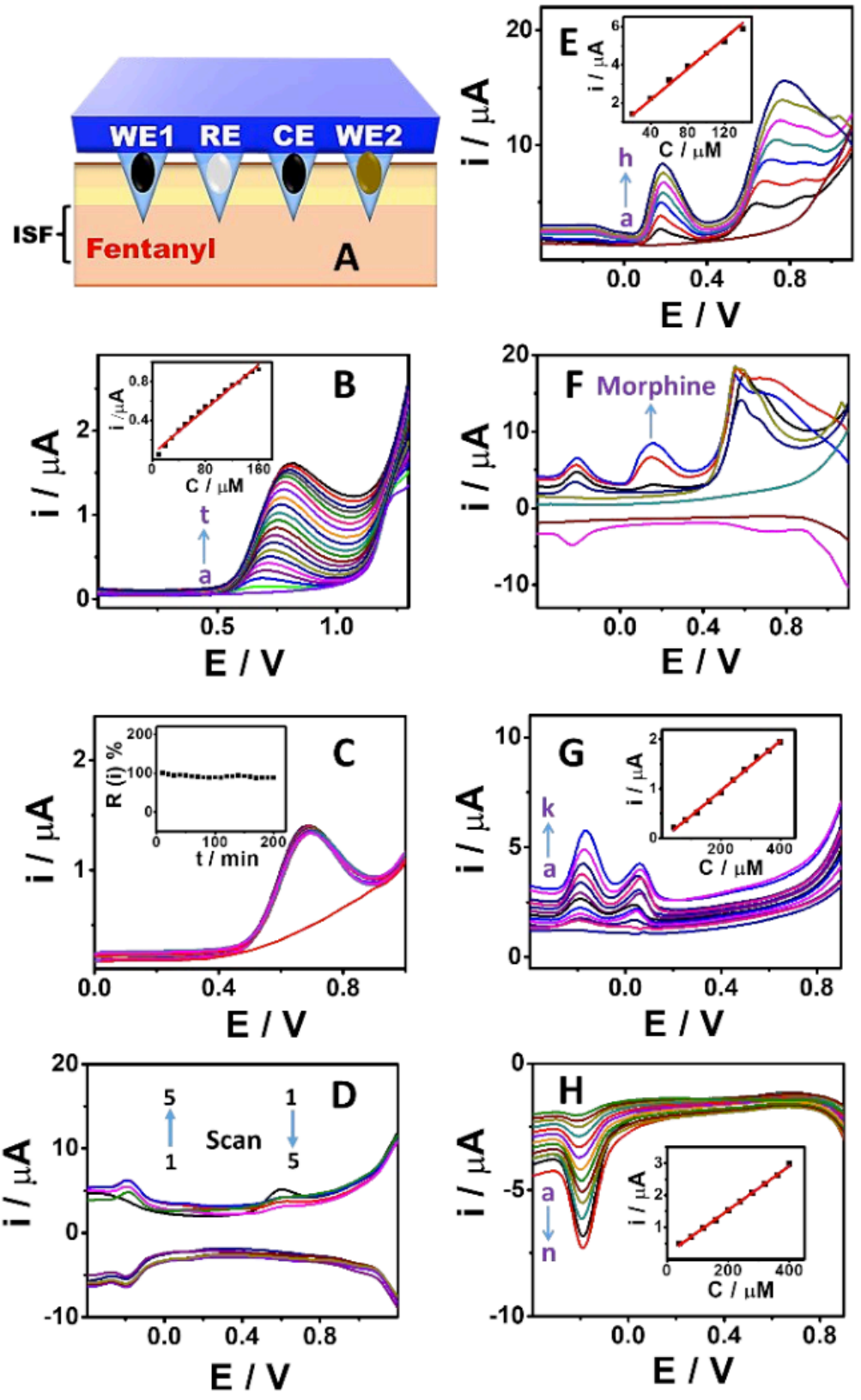
WE1
RE
CE
WE2
ISF
Fentanyl
A
B
C
D
E
F
Morphine
G
H
i / μA
E / V
C / μM
t / min
R (i) %
Scan
h
a
t
k
n

2. Results & Discussion

Figure 2A shows a schematics of microneedle sensor for voltammetric detection of fentanyl. The fentanyl sensor was initially characterized over a wide concentration range, 10-200μM (Figure 2B). A well-defined fentanyl oxidation peak is observed at +0.7V, reflecting the two-electron oxidation of the fentanyl tertiary amine groups. The corresponding calibration plot (inset) displays a linear dependence of this anodic current response with the drug concentration over the entire range. Continuous subcutaneous chemical threat monitoring applications would require a stable electrochemical response for both target analytes. While various polymeric membranes were tested as outer protective layers of our sensor, PVC and poly(*o* - phenylenediamine) (PPD) offered higher stability during prolonged sensing operations (Figure S1, Supporting information). For example, the PVC-coated microneedle sensor displayed reproducible results during continuous 3h measurements of 50μM fentanyl, retaining nearly 90% of its original response (Figure 2C). The selectivity of the system against common interfering compounds was also demonstrated, with the fentanyl response not affected by these constituents (Figure S2). Figure 2D illustrates repetitive cyclic-square wave voltametric (CSWV) measurements of 30 μM fentanyl over 5 successive scans. Such SCSWC operation provides a unique and distinct electrochemical finger print of fentanyl, while discriminating against the capacitive background current. The CSWV response sows an initial irreversible oxidation of fentanyl in the first anodic scan. In subsequent cathodic and anodic scans.[13] Such distinct redox signature offers a fast (1 min) identification of fentanyl in the presence of potential interferences.

The microneedle WE1 was used also for morphine detection independently as well as in combination with fentanyl. Figure 2E displays such electrocatalytic detection of morphine over the 20-140μM range. Two well-separated anodic morphine peaks are observed at +0.2V and

+0.7V, corresponding to the pseudo-morphine generation and oxidative dealkylation of piperidine tertiary amine, respectively.[24] As expected for amine-containing redox reactions, both morphine and fentanyl contribute to the oxidative current at +0.7V when using a mixture of these drugs; however, these drugs can be separated based on the morphine peak at +0.2V (Figure 2F). On-body microneedle fentanyl tracking should be able to etect not only fentanyl but also its metabolic products (primarily norfentanyl). Figures 2G,H show forward and reverse CSWV scans for norfentanyl over a broad 40-400μM concentration range. These volammograms display an anodic oxidation resulted in a reversible redox behavior at -0.2, along with a second oxidation peak at +0.1V. The latter was not observed in the first scan, suggesting that the +0.1V peak orresponds to the product formed during the cathodic scan. The electrochemical detection of OP compound relies on the anodic oxidation of p-nitrophenol product of the OP-OPH enzymatic reaction on the CP-filled microneedle transducer surface. The anodic peak appeared at +0.72V is proportional to the level of the hydrolyzed MPOx. Figure 3B displays the SWV response of the OP microneedle biosensor for increasing (10- 160μM) MPOx levels. The voltammograms display a well- defined nitrophenol oxidation peak which grows with the MPOx concentration (inset; Figure 3A) and facilitates the identification and quantitation of the target OP compound down to a detection limit of 10μM level. The operational stability of the OPH-based microneedle biosensor was evaluated using 100μM MPOx by 12 repetitive measurements at 10 min intervals (Figure 3B). A stable nitrophenol peak is observed throughout this operation, with the OPH-biosensor retaining over 90% of its original response to the target nerve threat detection benefits also from the distinct SWV profiles and from the OPH enzyme recognition.

The analytical performance of dual microneedle sensor array was evaluated for the fentanyl and nerve-agent targets in agarose tissue-mimicking phantom gel skin model[25]. As shown in

Figures 3E,F, such tissue-mimicking tests resulted in well- defined voltammetric response for both analytes, with peak currents increasing linearly upon raising the chemical-threat concentration. Such attractive behavior in tissue-mimicking model indicates considerable promise for future on-body monitoring towards distinguishing between exposures to opioid or nerve agent threats.

Towards practical in-vivo opioid monitoring that needs to detect lower concentrations, the sensitivity of the microneedle- based fentanyl detection was greatly enhanced through further modification of the electrode. According to the 'European Centre for Monitoring Drugs and Drugs Addiction', blood fentanyl concentrations above ~60nM can have fatal effects. Nanomolar fentanyl detection was thus achieved by a judiciously designed multi-layered surface architecture, incorporating multi-walled CNT into the CP along with a hybrid of Au nanoparticles and reduced graphene film on the electrode (Figures S3 A, 3G) Such highly sensitive fentanyl detection, down to the 50nM level, is demonstrated in Figure 3H using a background-subtracted SWV operation. Such ultrasensitive fentanyl detection is attributed to the synergistic combination of highly conductive large-surface area graphene nanosheets for preconcentrating the drug through strong π-π interactions along with the efficient electrocatalytic action of Au nanoparticles[26,27] and the facilitated electron transfer enabled by CNT-incorporated CP transducer.[28] Such synergistic signal amplification is demonstrated in Figure S3. Furthermore, such multi-layered design exhibited efficient anti-biofouling protection towards prolonged operational stability in protein-rich sample (Figure S3) along with high selectivity against potential interferences (Figure S4).

3. Conclusion

We presented the first example of a microneedle sensor array for the simultaneous minimally-invasive detection of fentanyl and OP nerve agents on a single wearable platform. The

resulting microneedle sensor array is able of distinguishing between episodes of opioid overdose and nerve agent poisoning, i.e., rapid field identification of such unknown exposure, toward immediate medical treatment. The new microneedle sensor array platform displays an attractive analytical performance for the OPi and OP targets in skin- mimicking agarose phantom gel, including high sensitivity, selectivity, and stability. Additionally, while the opioid microneedle sensor can detect fentanyl based on its distinct redox signature, and measure morphine and norfentanyl based on different potentials, it is not a universal opioid detector. Such a multi-modal wearable sensing platform holds a considerable promise for timely feedback and appropriate countermeasure on drug and nerve agent exposure in a field setting. The promising analytical results obtained in this proof- of-concept demonstration open up new possibilities towards a fast "sense and act" closed-loop wearable system and timely countermeasures (antidote release from the same microneedle patch) for protecting our civilians and soldiers. Future efforts will thus involve a detailed animal study of the new microneedle patch and its integration with such timely therapeutic action.

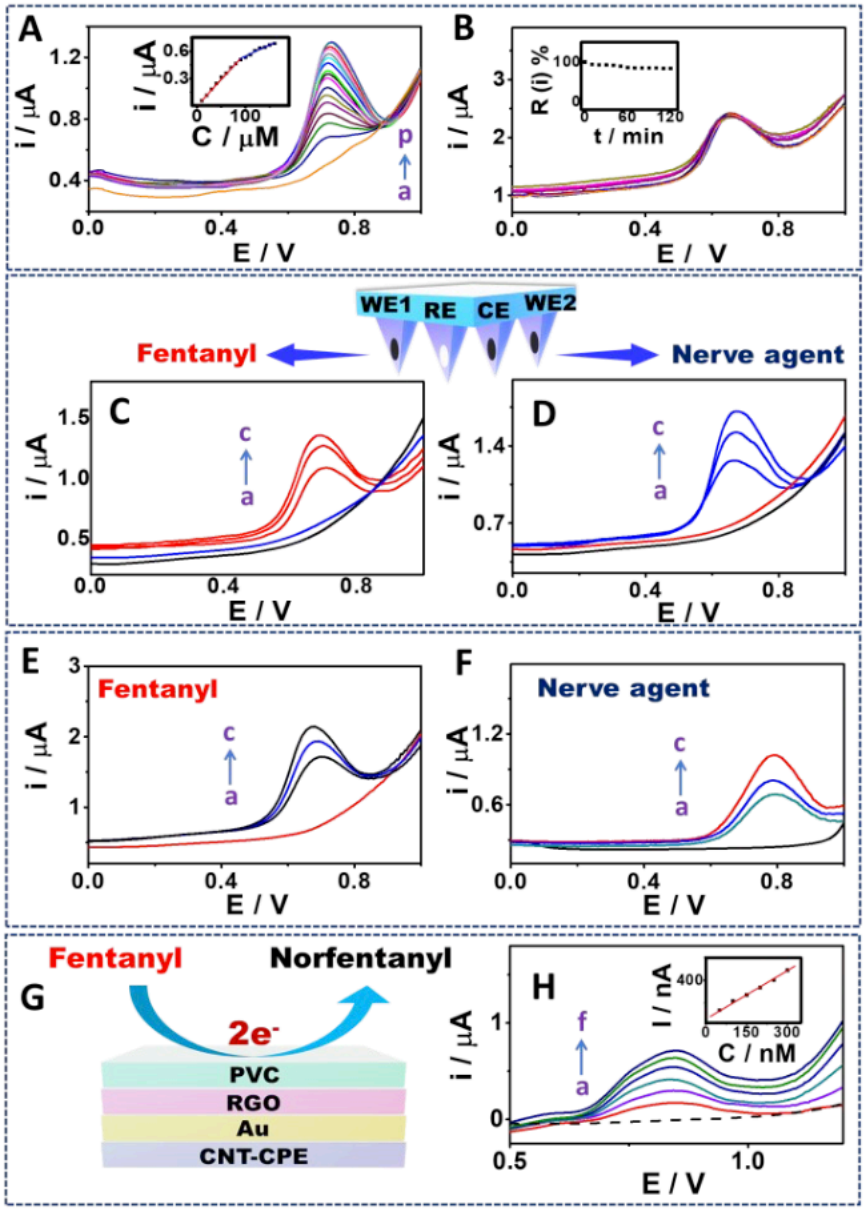

Figure 4. 3: Analytical evaluation of the microneedle sensor array. A. SWV of MPOx detection over 10-160µM concentration range in 10µM increments and the corresponding calibration plot (inset) B. Stability of the microneedle-based 100µM MPOx detection during 2h repetitive measurements at 10min intervals, along with plot of the relative current change during this period (inset). C,D. Cross-talk study on a single platform. C. Increasing fentanyl concentrations (50, 100 and 150µM; in red) in a 100µM MPOx solution (blue curve). E. MPOx detection (50, 100 and 150µM; in blue) in the presence of 100µM fentanyl (red curve). E,F. Detection of increasing levels of fentanyl and MPOx (50, 100 and 150µM) in skin-mimicking gel (1% agarose). G. Schematic illustration of the multi-layered electrode used for ultrasensitive fentanyl detection on the microneedle sensor array. I. Background-subtracted SWV fentanyl response (50-300nM; in 50nM increments) with the corresponding calibration plot (inset). See Figure S5 for the raw unsmoothed data.

agent (inset). Additionally, the OPH/Nafion microneedle electrode has previously shown high selectivity toward the target OP nerve agent.[15]

The integration of two different sensing modalities on a single microneedle platform is challenging. Enzymatic and non- enzymatic electrodes were evaluated for their selective detection of the fentanyl and OP nerve agent targets at such neighboring microneedle sensors (WE1 and WE2, respectively). Figures 3C,D display evaluation of potential cross-talk during the simultaneous detection of these target analytes in artificial ISF medium. These data clearly demonstrate the absence of such cross talk, i.e., no interference caused by the presence of the other compound.

Acknowledgement

Chapter 4 is based, in part, on the material as it appears in Journal of the American Chemical Society, 2019, by Rupesh K. Mishra, K. Yugender Goud, Zhanhong Li, Chochanon Moonla, Mona A. Mohamed, Farshad Tehrani, Hazhir Teymourian, and Joseph Wang. The dissertation author was the co-investigator and coauthor of this paper.

4. References

1. McNamara, P. Opioid Switching from Morphine to Transdermal Fentanyl for Toxicity Reduction in Palliative Care. *Palliat. Med.* **2002**, *16*, 425–434.

2. Nandakumar, R.; Gollakota, S.; Sunshine, J. E. Opioid Overdose Detection Using Smartphones. *Sci. Transl. Med.* **2019**, *11*, eaau8914.

3. Sutter, M. E.; Gerona, R. R.; Davis, M. T.; Roche, B. M.; Colby, D. K.; Chenoweth, J. A.; Adams, A. J.; Owen, K. P.; Ford, J. B.; Black, H. B.; Albertson, T.E. Fatal Fentanyl: One Pill Can Kill. *Acad. Emerg. Med.* **2017**, *24*, 106-113.

4. Florence, C. S.; Zhou, C.; Luo, F.; Xu, L. The Economic Burden of Prescription Opioid Overdose, Abuse, and Dependence in the United States, 2013. *Med. Care* **2016**, *54*, 901–906.

5. Argote, K.A.; Molloy, M.; Hart, A.; Voskanyan, A.; Sarin, R.R.; Ciottone, G. Chemical Warfare Agent Terrorist Attacks in Latin America and the Caribbean Region (CWA-LAC). *Prehosp. Disaster Med.,* **2019**, *34*, s13.

6. Riches, J. R.; Read, R. W.; Black, R. M.; Cooper, N. J.; Timperley, C. M. Analysis of Clothing and Urine from Moscow Theatre Siege Casualties Reveals Carfentanil and Remifentanil Use. *J. Anal. Toxicol.* **2012**. *36*, 647–656.

7. Thiermann, H.; Worek, F.; Kehe, K. Limitations and Challenges in Treatment of Acute Chemical Warfare Agent Poisoning. *Chem. Biol. Interact.* **2013**, *206*, 435-443.

8. Wax, P. M.; Becker, C. E.; Curry, S. C. Unexpected "Gas" Casualties in Moscow: A Medical Toxicology Perspective. *Ann. Emerg. Med.* **2003**, *41*, 700–705.

9. Jeffery, R. M.; Dickinson, L.; Ng, N. D.; DeGeorge, L. M.; Nable, J. V. Naloxone Administration for Suspected Opioid Overdose: An Expanded Scope of Practice by a Basic Life Support Collegiate-Based Emergency Medical Services Agency. *J. Am. Coll. Heal.* **2017**, *65*, 212-216.

10. Mills, P. C.; Magnusson, B. M.; Cross, S. E. Investigation of in Vitro Transdermal Absorption of Fentanyl from Patches Placed on Skin Samples Obtained from Various Anatomic Regions of Dogs. *Am. J. Vet. Res.* **2004**, *65*, 1697-1700.

11. Ciottone, G. R. Toxidrome Recognition in Chemical- Weapons Attacks. *N. Engl. J. Med.* **2018**, *378*, 1611–1620.

12. Kim, J.; Campbell, A. S.; de Ávila, B. E.-F.; Wang, J. Wearable Biosensors for Healthcare Monitoring. *Nat. Biotechnol.* **2019**, *37*, 389–406.

13. Goodchild, S. A.; Hubble, L. J.; Mishra, R. K.; Li, Z.; Goud, K. Y.; Barfidokht, A.; Shah, R.; Bagot, K. S.; McIntosh, A. J. S.; Wang, J. Ionic Liquid-Modified Disposable Electrochemical Sensor Strip for Analysis of Fentanyl. *Anal. Chem.* **2019**, *91*, 3747–3753.

14. Barfidokht, A.; Mishra, R. K.; Seenivasan, R.; Liu, S.; Hubble, L. J.; Wang, J.; Hall, D. A. Wearable Electrochemical Glove-Based Sensor for Rapid and on-Site Detection of Fentanyl. *Sensors Actuators B Chem.* **2019**, *296*, 126422.

15. Mishra, R. K.; Vinu Mohan, A. M.; Soto, F.; Chrostowski, R.; Wang, J. A Microneedle Biosensor for Minimally-Invasive Transdermal Detection of Nerve Agents. *Analyst* **2017**, *142*, 918–924.

16. Mohan, A. M. V.; Windmiller, J. R.; Mishra, R. K.; Wang, J. Continuous Minimally-Invasive Alcohol Monitoring Using Microneedle Sensor Arrays. *Biosens. Bioelectron.* **2017**, *91*, 574-579.

17. Valdés-Ramírez, G.; Li, Y.-C.; Kim, J.; Jia, W.; Bandodkar, A. J.; Nuñez-Flores, R.; Miller, P. R.; Wu, S.-Y.; Narayan, R.; Windmiller, J. R.; Polsky, R.; Wang, J. Microneedle- Based Self-Powered Glucose Sensor. *Electrochem. commun.* **2014**, *47*, 58–62.

18. Windmiller, J.R.; Zhou, N.; Chuang, M.C.; Valdés-Ramírez, G.; Santhosh, P.; MIller, P.R.; Narayan, R.; Wang, J., Microneedle array-based carbon paste amperometric sensors and biosensors, *Analyst* **2011**, *136*, 1846-1851.

19. Miller, P. R.; Xiao, X.; Brener, I.; Burckel, D. B.; Narayan, R.; Polsky, R. Microneedle-Based Transdermal Sensor for On-Chip Potentiometric Determination of K+. *Adv. Healthc. Mater.* **2014**, *3*, 876–881.

20. Bollella, P.; Sharma, S.; Cass, A. E. G.; Antiochia, R. Microneedle-Based Biosensor for Minimally-Invasive Lactate Detection. *Biosens. Bioelectron.* **2019**, *123*, 152- 159.

21. Goud, K. Y.; Moonla, C.; Mishra, R. K.; Yu, C.; Narayan, R.; Litvan, I.; Wang, J. Wearable Electrochemical Microneedle Sensor for Continuous Monitoring of Levodopa: Toward Parkinson Management. *ACS Sensors* **2019**, *4*, 2196-2204.

22. Teymourian, H., Moonla, C., Tehrani, F., Vargas, E., Aghavali, R., Barfidokht, A., Tangkuaram, T., Mercier, P. P., Dassau, E., Wang, J. Microneedle-Based Detection of Ketone Bodies along with Glucose and Lactate: Toward Real-Time Continuous ISF Monitoring of Diabetic Ketosis/Ketoacidosis. *Anal. Chem.* **2020**, *92*, 2291-2300.

23. Ciui, B.; Martin, A.; Mishra, R. K.; Brunetti, B.; Nakagawa, T.; Dawkins, T. J.; Lyu, M.; Cristea, C.; Sandulescu, R.; Wang, J. Wearable Wireless Tyrosinase Bandage and Microneedle Sensors: Toward Melanoma Screening. *Adv. Healthc. Mater.* **2018**, *7*, e1701264.

24. Navaee, A.; Salimi, A.; Teymourian, H. Graphene Nanosheets Modified Glassy Carbon Electrode for Simultaneous Detection of Heroine, Morphine and Noscapine. *Biosens. Bioelectron.* **2012**, *31*, 205–211.

25. Chang, H.; Zheng, M.; Yu, X.; Than, A.; Seeni, R. Z.; Kang, R.; Tian, J.; Khanh, D. P.; Liu, L.; Chen, P.; Xu, C. A Swellable Microneedle Patch to Rapidly Extract Skin Interstitial Fluid for Timely Metabolic Analysis. *Adv. Mater.* **2017**, *29*, 1702243.

26. Li, J.; Lin, X. Electrocatalytic oxidation of hydrazine and hydroxylamine at gold nanoparticle—polypyrrole nanowire modified glassy carbon electrode. *Sens. Actuators B.* **2007**, *126*, 527-535.

27. Agüí, L.; Paloma, J.; Yáñez-Sedeño, P.; Pingarrón, J.M. Amperometric biosensor for hypoxanthine based on immobilized xanthine oxidase on nanocrystal gold–carbon paste electrodes. *Sens. Actuators B.* **2006**, *113*, 272-280.

28. Wang, J. Carbon-nanotube based electrochemical biosensors: A review. *Electroanalysis*, **2005**, *17*, 7-14.

Chapter 5. The Future; Aptamers on Microneedles

Wearable Microneedle Aptamer-Based Sensors for Continuous, Real-Time Molecular Monitoring in the Body

1. Introduction

The development of wearable and autonomous sensing technologies enabling continuous, real-time monitoring of clinically relevant therapeutics, metabolites and biomarkers in the body could dramatically transform the way we study, understand, diagnose, and treat disease. Continuous Electrochemical Aptamer-based Microneedle Monitoring (CEAMM) can virtually unlock monitoring of most biomarkers. could be used to, for example, achieve highly precise and personalized drug therapy via real-time monitoring of patient-specific pharmacokinetics, pharmacodynamics, and toxicology. The in vivo pharmacological data produced could be coupled to drug delivery devices via feedback control, allowing therapeutic dosing to occur at the exact time and dose needed and in response to minute-to-minute fluctuations in an individual's physiology.[1, 2] In contrast, our current approach to drug therapy relies on population-based, often inaccurate physical indexes such as age, weight or body mass, or indirect parameters such as genotype, that are poor predictors of a patient's immediate physiological state and of effective therapeutic dosing.[3-5] In addition, the standard of care of using phlebotomy and laboratory-based molecular measurements is costly, slow and inconvenient, often failing to prevent patient readmission.[6,7] Given the clinical importance of developing therapeutic strategies that effectively address patient-to-patient pharmacokinetic variability[8] and overcome inaccurate pharmacokinetic

estimates,[9] there remains a critical need for in vivo sensing platforms that can achieve remote, autonomous, continuous, and individualized molecular monitoring in real-time.

Although the future of personalized medicine will almost certainly involve some form of wearable biochemical monitors, technology development must place significant consideration into identifying the most suitable body compartment for therapeutic or biomarker measurements. Current diagnostics and wearable platforms target body fluids such as blood, urine, saliva and sweat.[10-14] Ideally, a continuous monitor would require placement inside a compartment where the accessible body fluid presents medically relevant molecular levels that reflect the full physiological state of the patient, or a disease-related state. Moreover, for large-scale adoption, the technology must be body-interfaced via minimally invasive strategies. In recent years, interstitial fluid (ISF) has been underscored as the most prevalent accessible fluid in the body that is underutilized as a source of biomarkers.[15] ISF is an ideal compartment for monitoring systemic molecular levels as it presents biomolecular concentrations and temporal profiles that strongly correlate with those of blood.[15] Unfortunately, access to ISF is not straightforward and requires cumbersome sample collection (e.g., iontophoresis, microdialisis, etc.) that, if not adequately performed, may cause lasting skin damage.[16]

A much-highlighted strategy to access ISF without any perceivable pain or skin damage lies in the use of wearable microneedles [Refs?]. By virtue of their sharp microscopic structures, microneedles can pierce the stratum corneum of the skin and reach the ISF within the dermis or between the epidermis and dermis. Thanks to their shallow depth (< 1 mm), microneedles reach neither nerve endings nor vasculature within the dermis,[17] offering painless and direct tapping into the ISF. To date, this technology has been employed to achieve high volume extraction of ISF for in vitro proteomics and diagnostics,[18] controlled therapeutic delivery,[19, 20] and molecular

monitoring using microneedle-supported biosensors.[21-23] In the space of diabetes management, for example, microneedles have been praised as a strong alternative to replacing the invasive long catheters (5-11 mm)[24] historically used to achieve continuous glucose monitoring (CGM) in ISF.[25, 26] Although continuous efforts have been devoted to maximizing the potential of microneedle-supported molecular monitors, successes have been limited to a few molecules that either undergo enzymatic conversion via oxidases or reductases, such as lactate,[27] glutamate,[28] β-hydroxybutyrate,[29] levodopa,[30] and alcohol,[31] or are redox active and can be directly oxidized or reduced on microneedle surfaces. Thus, there remains a critical need to expand microneedle-supported sensing to other health-relevant ISF molecular markers that cannot undergo enzymatic or direct electrochemical conversion.

This work aims to expand the molecular space that can be sensed via microneedle-supported monitors by coupling the technology with electrochemical, aptamer-based sensors (E-ABs), an affinity-based measurement strategy that does not depend on molecular reactivity. Aptamers are short single-stranded nucleic acid sequences that can be selected through Systematic Evolution of Ligands by Exponential Enrichment (SELEX) for binding to, in principle, any arbitrary target with high affinity.[32-34] One example of integrating aptamers with microneedles was recently proposed by Yi et al.[35] Taking advantage of porous microneedle arrays and endotoxin-binding aptamers, they achieved minimally invasive extraction of ISF through the porous microneedles and detection of endotoxin based on fluorescence emission. Although these novel aptamer-decorated porous microneedles enable the extraction and detection of biomarkers in ISF, they cannot support continuous, real-time molecular monitoring in vitro, much less in vivo. Similarly, the use of immunoassays for expanding the molecular scope of microneedles is hindered by the inability to regenerate the antibody receptor. However, this challenge can be

resolved by coupling the high affinity molecular recognition afforded by aptamers with electrochemical detection. Specifically, the aptamers in E-AB sensors undergo binding-induced conformational changes,[36] which occur in scales of milliseconds, are reversible, and readily enable continuous molecular monitoring in the living body[10, 37, 38].

Our groups have independently developed wearable microneedle sensor arrays and in vivo E-ABs. Here we combine our expertise to report a first prototyping of microneedle E-AB arrays for continuous monitoring of therapeutic agents in vivo (Fig. 1). This work reports 5 key innovations: 1) we successfully designed and manufactured gold microneedle sensors that readily enable E-AB functionalization using established methods; 2) we developed a 3-D printed, gravity-driven microfluidic device that mimics in-vivo excretion kinetics to demonstrate that our microneedle E-AB arrays achieve continuous drug monitoring in real time; 3) we established a cleaning protocol to successfully regenerate the surfaces of these highly engineered microneedles to enable re-functionalization and reuse; 4) we demonstrate, for the first time, simultaneous monitoring of a prodrug and its metabolite using newly developed, highly sensitive aptamers; and 5) we demonstrate the deployment of this continuous monitor for real-time drug tracking within living animals.

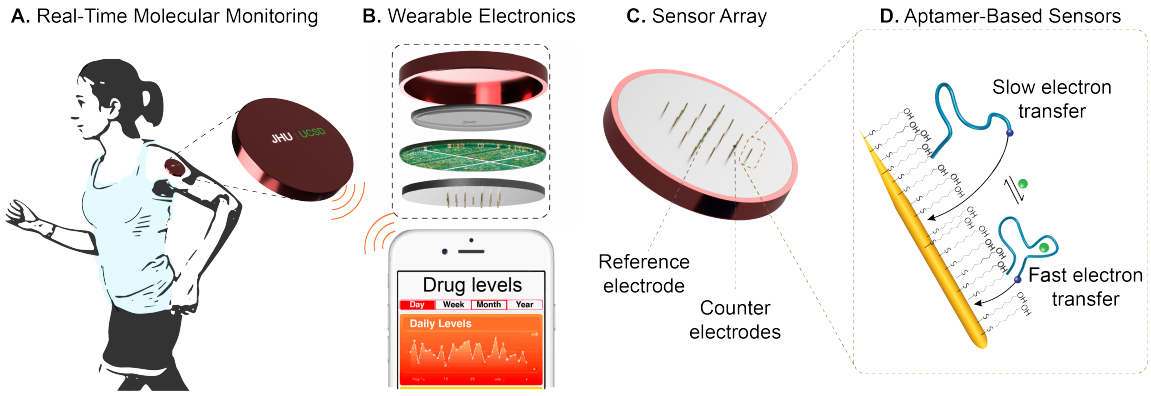

Figure. 5. 1. Wearable sensors for continuous, real-time on-body molecular monitoring. Coupling of electrochemical aptamer-based sensors (E-ABs) with microneedle electrode arrays for minimally invasive monitoring of molecular targets in interstitial fluid (ISF). (**A**) Our wearable microneedle sensor patch is designed to allow painless on-body molecular tracking during the normal daily routine. (**B**) The patch consists of a microneedle sensor array closely integrated with wearable, proprietary electronics and a battery contained within an ergonomic wearable case. The electronic board is equipped with Bluetooth technology to wirelessly transmit ISF molecular concentration data to smart devices. (**C**) To enable electrochemical sensing, the microneedle sensor array contains 16 gold working, 4 platinum counter, and one central reference microneedles with a form factor that allows painless penetration of the upper strata of the reticular dermis, avoiding the rupture of capillary vessels or damage to nerves. (**D**) At the core of our sensing technology are E-ABs, which consist of a mixed self-assembled monolayer of electrode-blocking alkanethiols with alkanethiol- and redox reporter-modified aptamers. In the presence of target, the aptamers undergo reversible binding-induced conformational changes that affect electron transfer between the reporter and the gold needles. This sensing mechanism is reversible and fast, allowing for subsecond-resolved molecular monitoring in vivo.

2. Results & Discussion

Real-Time Molecular Sensing on Microneedles Irrespective of Target Reactivity

Our first goal was to design integrated devices allowing the rapid testing of microneedle E-AB sensor array performance in vitro. Through this effort, we demonstrate that E-ABs can be easily fabricated on 3D printed, vapor-deposited gold-based microneedles. In addition, we show that the resulting microneedle E-ABs allow continuous, real-time molecular monitoring with identical performance to benchmark E-ABs made on commercial disc macroelectrodes. To create our rapid-test devices, we 3D-printed flow devices using biocompatible, methacrylate-based resins (Fig. 2A). The main inlet of these devices was connected to a peristaltic pump flowing buffered solutions from a beaker. The solutions overfilled the microneedle chamber, and slowly flowed out

into two external drains located on the sides of each device and open to an underlying waste beaker. This approach allowed us to mimic excretion kinetics as they would occur in a living rodent by the exit of blood drug levels to urine via the kidneys. Moreover, the flow rate is adjustable, allowing us to test sensor performance under different flow conditions. Two additional, secondary inlets are connected to a computer-controlled syringe pump, enabling us to perform drug injections through one, and rapid mixing of drug levels (< 10 s) through the other (by pulling liquid out and back in). This mixing rate is analogous to the natural mixing of drugs in the bloodstream of rats as determined by E-AB measurements.[39] We provide 3D models of our device as supporting information.

The microneedle electrode arrays employed during our rapid testing were fabricated via established, previously reported procedures.29 Briefly, we 3D-printed the arrays using resin UV-curing Formlabs model 3 at a 25 micron resolution and bonded them to printed circuit boards containing connections leading to a back port for the potentiostat leads. We then sealed the base of the microneedles using insulating epoxy resin. Next, we sputtered the microneedles with chromium-supported layers of gold for the working and counter microneedle electrodes. Silver and silver chloride ink was applied on the reference microneedle electrode. Each finalized device contains 16 working, 4 counter, and 1 reference microneedle electrodes. The two-dimensional design for our microneedle substrate, showing electrode connections for single and dual devices, is provided as supporting information. To produce the integrated device illustrated in Fig. 2A, we glued the resulting microneedle devices to the bottom of our flow platform using insulating epoxy resin. For rapid testing, we produced blunt microneedles (not intended for skin penetration) with a height of ~2.264 mm and a diameter of ~ 170 μm (Fig. 2B). Using these microneedles, we built E-ABs via incubation in solutions of alkanethiol and redox reporter-modified aptamers, followed

by backfilling of any remaining gold surface sites with mercaptohexanol, as is established in the field.[40]

The sensing performance of microneedle E-AB sensor arrays is identical to that of benchmark E-ABs fabricated on commercial disc electrodes. We demonstrated this by fabricating, in parallel, tobramycin-binding E-ABs on both our microneedle devices and on disc macroelectrodes (2 mm in diameter). We selected the tobramycin-binding aptamer for this comparison because it is one of the most studied in the E-AB platform.[2, 10, 41, 42] To fabricate E-ABs, we incubated both the microneedles and macroelectrodes in aqueous solutions of 200 nM tobramycin-binding aptamer for 1 h. We then rinsed the electrodes with deionized water and incubated them 3 h in a solution containing 30 mM mercaptohexanol, the benchmark blocking monolayer used in the field.[36, 43] To evaluate sensing performance, we built calibration curves in static, buffered solutions by challenging the E-ABs with increasing concentrations of tobramycin and measuring their response via square wave voltammetry, at signal-ON and signal-OFF square wave frequencies of 800 Hz and 150 Hz, respectively. The resulting traces (Fig. 2C) were identical between electrode types, achieving the same signal gain and dynamic range irrespective of electrode geometry.

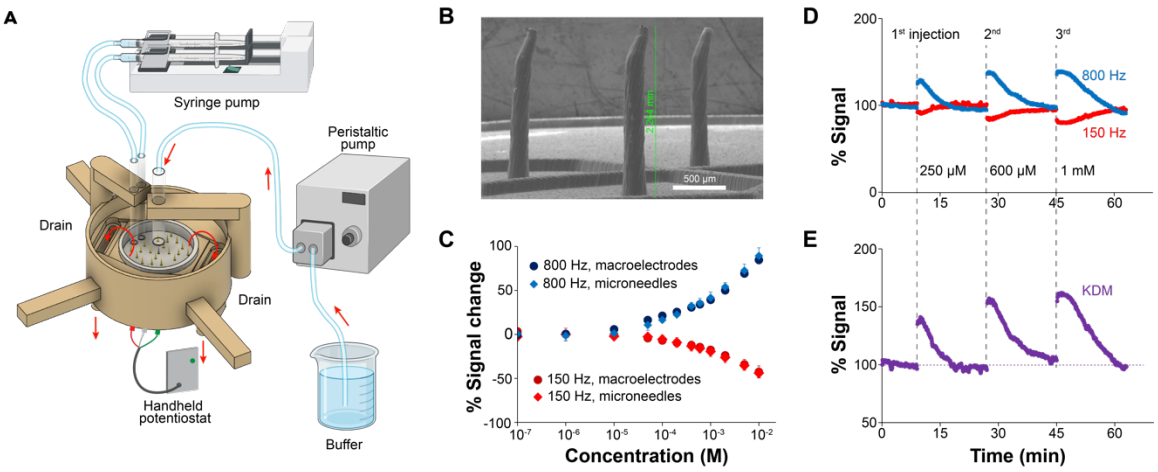

Figure. 5. 2. Microneedle E-AB sensor arrays support real-time molecular monitoring in vitro. We integrated microneedle E-AB sensor arrays into 3-D printed flow devices to demonstrate continuous, real-time monitoring of the aminoglycoside antibiotic tobramycin in vitro. **(A)** The 3-D printed support is designed to have one buffer inlet located at the center of the device for continuous buffer flow, two inlets at the left side for connecting with automatic target injection and mixing systems, and two drains for gravity-driven flow to waste. The microneedle sensor array is embedded in the 3-D device using epoxy resin and connected to a hand-held potentiostat to enable serial electrochemical measurements. **(B)** Micrograph of the blunt microneedles used for early prototyping and rapid testing. The microneedle height is ~2.264 mm and a diameter ~ 170 μm. We functionalized these using tobramycin-binding aptamers, which are modified to have covalently attached alkanethiol linkers and a redox reporter. In the presence of tobramycin, the aptamers undergo binding-induced conformational changes that alter electron transfer between the reporter and the microneedles. These changes can be easily measured in real time using square-wave voltammetry (SWV). **(C)** Microneedle E-AB sensor arrays achieve identical calibration curves relative to sensors fabricated on commercial disc macroelectrodes (2 mm in diameter). Measurements performed in 20 mM Tris, 100 mM NaCl, 5 mM MgCl2 (pH = 7.4). **(D)** Continuous, real-time monitoring of tobramycin in a flow system that mimics drug excretion kinetics. Doses were adjusted to reach tobramycin concentrations equal to 250 μM, 600 μM and 1 mM. Injections were performed at 9, 27, and 45 minutes after collecting an initial baseline. **(E)** Kinetic differential measurements (KDM) obtained after subtracting data collected at 150 Hz (signal-OFF output) from data collected at 800 Hz (signal-ON output).

Microneedle E-AB sensor arrays readily support continuous molecular monitoring in flowing buffered solutions. To demonstrate this capability, we serially interrogated microneedle E-ABs at two square wave frequencies (150 Hz and 800 Hz) every 5 s, while flowing buffer at a rate of 0.66 mL/min. To achieve real-time data processing and visualization, we used SACMES, a previously reported, open-access Python script.[44] To emulate an in-vivo titration, we injected three target tobramycin concentrations, 250 μM, 600 μM and 1 mM, after collecting an initial 9

min-long baseline (Fig. 2D). We specifically adjusted the injection (0.1 mL/min and mixing (0.5 mL/min) rates of the syringe pump to emulate a bolus followed by rapid mixing, so that each injection will display a short-lived target plateau concentration, followed by 1st order excretion kinetics. The response of each individual bolus matched the corresponding gain from the calibration curve in Fig. 2C. In addition, we implemented kinetic differential measurements (KDM),[2, 10] a strategy that leverages the strong signaling dependence of E-ABs on square-wave frequency to correct for baseline drift in real time. Using SACMES, we subtracted the data collected at 150 Hz from that measured at 800 Hz in real time to achieve the drift-corrected drug profiles reported in Fig. 2E. These results indicate that E-AB sensing is fully supported by microneedle arrays and could dramatically expand the space/scope? of molecular targets to be sensed in biomedical applications.

Multiuse Devices Achieving Highly Reproducible Measurements

One caveat of working with heavily engineered devices like microneedles for sensor prototyping is the relative high cost of producing them. Although the devices shown in Fig. 2 were fabricated via cost-effective 3D-printing and metal deposition techniques, inherent cost comes from the time it takes to produce each batch of devices. To make our technology development process more convenient and cost effective, we set out to develop a protocol allowing the re-use of each microneedle device for E-AB prototyping for over 3 times without an impact on E-AB signaling. The protocol involves a series of chemical and electrochemical cleaning steps, the cleaning efficiency of which can be monitored via voltammetric evaluation of the gold surface in dilute (0.05 M) sulfuric acid solutions. Briefly, we take freshly prepared microneedle devices (post metal deposition) and incubate them in 600 μL of 10% commercial gold cleaning solution

(containing thiourea and sulfuric acid, SIGMA #667978) for 10s. This solution oxidizes the gold surface according to the following equation[45]:

$$Au + 2\,CS(NH_2)_2 \rightleftharpoons Au(NH_2CSNH_2)_2^{+} + e^{-} \qquad \text{eq. 1}$$

Next, we follow this cleaning step by incubating the microneedles in pure ethanol for 10 min. Ethanol removes the thiourea and reduces remaining reduce gold oxides according to the relation[46]:

$$Au_2O_3 + 3\,CH_3CH_2OH \longrightarrow 2\,Au(0) + 3\,CH_3CHO + 3\,H_2O \qquad \text{eq. 2}$$

Finally, we perform standard electrochemical cleaning steps as previously reported[36, 40] and described in the methods section. To demonstrate the performance of this protocol, we functionalized the same microneedle device with tobramycin-binding aptamer 3 independent times, and performed continuous measurements of tobramycin as in Fig. 2D, E. The resulting measurements had a relative standard deviation within ~10% at any given target concentration (Fig. 3A), demonstrating that our cleaning protocol enables reproducible device reuse. In addition, the implementation of KDM to correct for drift resulted in drug profiles with relative standard deviations that were ≤ 10% at tobramycin concentrations < 1 mM. We anticipate this protocol will translate well to other electrode geometries and may become a standard for the cleaning of gold surfaces prior to E-AB functionalization.

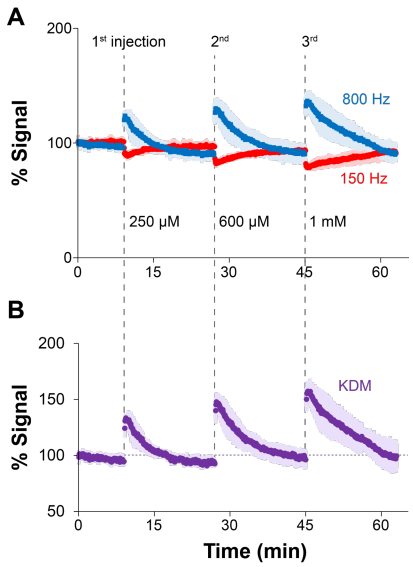

Figure. 5. 3. Microneedle arrays can be reused multiple times. We developed a chemical and electrochemical cleaning protocol allowing the reuse of these highly engineered devices multiple times during rapid prototyping and testing. **(A)** Here, for example, we show the performance of E-ABs fabricated on a single device that was reused 3 times. The colored data corresponds to the average of three identical measurements performed on the same device after cleaning. The shaded areas indicate the standard deviation between measurements. **(B)** Using state-of-the-art drift correction strategies (KDM), we show baseline corrected measurements that further emphasize the reproducibility achieved post device reuse via our cleaning protocol.

3. Methods & Materials

Chemicals and Materials: Oligonucleotide synthesis reagents, D-nucleoside phosphoramidites, 3'-PT-Amino-Modifier C6 CPG, Thiol-Modifier C6 S-S phosphoramidite, Methylene Blue NHS Ester and Glen-Pak DNA purification cartridges were purchased from Glen Research (Sterling, VA). L-nucleoside phosphoramidites were purchased from ChemGenes (Wilmington, MA). Acrylamide/ bisacrylamide solution for denaturing PAGE was purchased from BioRad Laboratories (Hercules, CA). Deprotection reagents were purchased from Sigma-Aldrich (St. Louis, MO).

6-mercapto-1-hexanol (MCH), 1-hexanethiol (HxSH), and Tris(2-carboxyethyl)phosphine hydrochloride (TCEP) were purchased from Sigma-Aldrich (St. Louis, MO). Phosphate buffered saline (PBS, 11.9mM HPO_3^{2-} ; 137mM NaCl; 2.7mM KCl; *p*H = 7.4) trace-metal grade sulfuric

acid (H_2SO_4), sodium hydroxide (NaOH), and sodium chloride (NaCl) were purchased from Fisher Scientific (Waltham, MA). Zinc chloride was purchased from Alfa Aesar (Ward Hill, MA). HEPES was purchased from J.T. Baker (Phillipsburg, NJ). Biological fluids were purchased from BioreclamationIVT (Washington, D.C.). S1 Nuclease was purchased from ThermoScientific (Lithuania). We prepared all aqueous solutions using deionized water from a Milli-Q® Direct purification system, with a resistivity of 18 MΩ. S1 buffer (pH ~ 5.4) contained 5 mM HEPES, 50mM NaCl, and 100 □M $ZnCl_2$. Gold working electrodes (PN: 002314, diameter: 1.6 mm) and coiled platinum wire counter electrodes (PN: 012961) were obtained from ALS Inc. (Tokyo, Japan). Silver / silver chloride reference electrodes (PN: CHI111) were purchased from CH Instruments (Austin, TX). For polishing electrodes, 1200/P2500 silicon carbide grinding paper (PN: 36-08-1200) was bought from Buehler (Lake Bluff, IL); cloth pads (PN: MF-1040) and alumina slurry (PN: CF-1050) were purchased from BASi (West Lafayette, IN).

Oligonucleotide synthesis and purification: Both D-DNA and L-DNA versions of the cocaine aptamer were prepared by solid-phase synthesis on an Expedite 8909 DNA/RNA synthesizer. A 3′-amine modification was installed by initiating each synthesis on 3′-PT-amino-modifier CPGs, followed by coupling of either D-nucleoside phosphoramidites or L-nucleoside phosphoramidites according to the manufacturers recommended protocols. The 5′-thiol modification was introduced as a disulfide during synthesis by coupling the thiol-modifier C6 S-S phosphoramidite to the 5'-terminus of each oligonucleotide as recommended by the manufacturer. The terminal 4,4′-dimethoxytrityl (DMT) group was retained for downstream purification. Following deprotection of the oligonucleotides by AMA (ammonium hydroxide/40% aqueous methylamine 1:1 v/v), the oligonucleotides were desalted using a Glen-Pak DNA purification cartridge and concentrated by ethanol precipitation. In order to attach the methylene

blue reporter, the crude oligonucleotide pellet was dissolved in 500 μL 0.1 M bicarbonate buffer (pH 9) to which a solution containing ~2 mg of methylene blue NHS ester in 12 μL DMSO was added. The coupling reaction was allowed to proceed overnight at room temperature and was quenched by ethanol precipitation. The modified oligonucleotides were purified by 20% denaturing polyacrylamide gel electrophoresis (PAGE; 19:1 acrylamide/bisacrylamide), and the products were excised from the gel and eluted overnight at room temperature in a buffer consisting of 200 mM NaCl, 10 mM EDTA, and 10mM Tris (pH 7.6). The solution was filtered to remove gel fragments and the oligonucleotides desalted by ethanol precipitation. The obtained pellet was resuspended in water and the concentration determined by measuring the absorbance at 260 nm using a Nanodrop 2000c spectrophotometer (Thermo Fisher Scientific, Waltham, MA). The purity and identity of all synthetic oligonucleotides was confirmed by mass spectrometric analysis (Novatia LLC, Newton, PA).

The oligonucleotide modifications employed in this work had the following structures:

Hexanethiol modification at the 5' terminus:

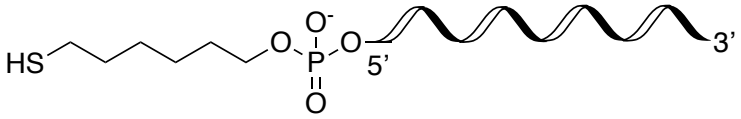

Methylene blue (MB) modification at the 3' terminus:

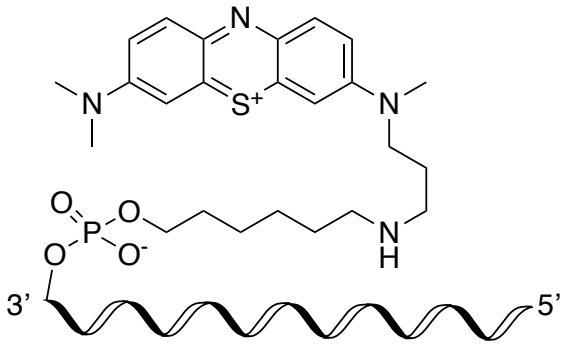

To prepare the DNA solutions, we first incubated 1 uL of 100 uM thiolated MB-modified DNA with 2 uL of 5 mM TCEP to reduce the disulfide bond. We then diluted the DNA with freshly prepared 1 mM thiol solution to a final concentration of 500 nM, as determined via molecular absorbance measurements employing an Implen Nanophotometer NP80.

Target	**Sequence**
Cocaine	5'- GGC GAC AAG GAA AAT CCT TCA ACG AAG GTG GGT GGC C -3'
N/A	5'- GGA TCG AAC TGG TAC GCC -3'

Electrode Preparation: Gold electrodes were polished for ~ 2 min on 1200/P2500 silicon carbide grinding paper, and subsequently for ~ 4 min on a cloth pad with alumina slurry. After rinsing with water to remove polishing debris, they were then electrochemically cleaned in 0.5M NaOH and 0.5M H_2SO_4 following a previously reported protocol.[20] Briefly, 1) in 0.5M NaOH, we scanned from -1 to -1.8 V vs Ag/AgCl, 400 times at a scan rate of 1V/s; 2) in 0.5M H_2SO_4, we scanned from 0.4 to -0.5 to 1.75 back to 0.4 V vs Ag/AgCl, 300 times at a scan rate of 1 V/s. Once electrodes were clean, we rinsed them with water and placed them immediately into 1 mM alkanethiol solutions with 500 nM DNA, then left them to incubate overnight. Post incubation, we rinsed electrodes with water and placed them into a custom, water jacketed electrochemical cell containing 1x PBS, S1 buffer, serum, saliva, or urine. The cell was kept at a constant temperature of either 25 ºC or 37 ºC by running temperature-controlled water through the cell jacket using a Huber Microprocessor Control MPC water recirculation bath.

Electrochemical Measurements: A CH Instruments Electrochemical Analyzer (CHI 1040C, Austin, TX) multichannel potentiostat and associated software was used for all CV and SWV measurements. We used a three-electrode cell configuration consisting of gold disk working,

coiled platinum wire counter, and Ag/AgCl (saturated KCl) reference electrodes. Cyclic voltammetry measurements were recorded at a scan rate of 100 mV/s in one of two potential windows: 1) -0.5 to 0.2 V vs. Ag/AgCl in PBS or biological fluids; 2) -0.3 to 0.2 V vs. Ag/AgCl in S1 buffer. Current was sampled every millisecond. SWV measurements were performed from 0 to -0.5 V vs Ag/AgCl with square-wave amplitude of 25mV, step size of 1 mV, and various frequencies. Temperature of the electrochemical cell was held constant by a Huber Microprocessor Control MPC water recirculation bath (Huber, Cary, NC).

Data Analysis: We employed a previously reported, open-source Python script called SACMES[21] for the batch processing of our electrochemical measurements. SACMES allows us to extract specific capacitive and faradaic currents from our electrochemical measurements, including peak currents, in real time. We determined dissociation constants for each sensor architecture using the specific signal ON frequency data producing the best fit to the Hill equation. We employed the non-linear regression function Igor Pro v8 graphing software to determine K_D values.

3. Conclusion

Here, we demonstrate the ability of E-AB sensors to track specific small molecules continuously and in real time capability that could provide an important tool for understanding physiology and pharmacology. By allowing arbitrary molecules to be monitored with high resolution in animals undergoing their normal daily routine, for example, the ability to perform such measurements could improve our knowledge of metabolism, pharmacokinetics, and toxicology. The few-second time resolution of our approach likewise suggests that it could improve our understanding of rapidly fluctuating physiological events, and the movement of drugs and metabolites across the blood–brain barrier and within the central nervous system. Finally, the ability to perform the measurement of specific molecules in the body in real time could enhance

the efficiency and accuracy with which drugs are dosed, in applications ranging from personalized, patient-specific measurements as a means of precisely tailoring dosing to long-term feedback-controlled drug delivery in which the dosage of a drug is varied in real time in response to minute-to-minute changes in a patient's physiological status. In short, the technology demonstrated here could enhance not only our understanding of health but also our ability to detect, monitor, and treat disease.

Acknowledgement

Chapter 5 is based, in part, on the material as it may appear in Proceedings of the National Academy of Sciences of the United States of America, 2022, by Yao Wu, Farshad Tehrani, Hazhir Teymourian, John Mack, Jonathan Kavner, Nickey Huang, Allison Furmidge, Joseph Wang, and Netzahualcóyotl Arroyo-Currás. The dissertation author was the primary co-investigator and coauthor of this paper.

4. References

(1). Li, J.; Liang, J. Y.; Laken, S. J.; Langer, R.; Traverso, G., Clinical opportunities for continuous biosensing and closed-loop therapies. *Trends Chem*. **2020**, *2* (4), 319-340.

(2). Ferguson, B. S.; Hoggarth, D. A.; Maliniak, D.; Ploense, K.; White, R. J.; Woodward, N.; Hsieh, K.; Bonham, A. J.; Eisenstein, M.; Kippin, T. E.; Plaxco, K. W.; Soh, H. T., Real-time, aptamer-based tracking of circulating therapeutic agents in living animals. *Sci. Transl. Med.* **2013**, *5* (213), 213ra165.

(3). Falagas, M. E.; Karageorgopoulos, D. E., Adjustment of dosing of antimicrobial agents for bodyweight in adults. *Lancet* **2010**, *375* (9710), 248-51.

(4). Shuter, B.; Aslani, A., Body surface area: Du bois and du bois revisited. *Eur. J. Appl. Physiol*. **2000**, *82* (3), 250-4.

(5). Vieira, P. A.; Shin, C. B.; Arroyo-Curras, N.; Ortega, G.; Li, W.; Keller, A. A.; Plaxco, K. W.; Kippin, T. E., Ultra-high-precision, in-vivo pharmacokinetic measurements highlight the

need for and a route toward more highly personalized medicine. *Front Mol. Biosci.* **2019**, *6*, 69.

(6). Neely, M. N.; Kato, L.; Youn, G.; Kraler, L.; Bayard, D.; van Guilder, M.; Schumitzky, A.; Yamada, W.; Jones, B.; Minejima, E., Prospective trial on the use of trough concentration versus area under the curve to determine therapeutic vancomycin dosing. *Antimicrob. Agents Chemother.* **2018**, *62* (2).

(7). Tsotsou, G. E.; Gkotzamani, P.; Petro, V.; Argyropoulou, A.; Karkalousos, P., A simple, rapid and low-cost spectrophotometric method for irinotecan quantification in human plasma and in pharmaceutical dosage forms. *Anal. Methods* **2021**, *13* (2), 258-266.

(8). Zhong, X.; Tong, X.; Ju, Y.; Du, X.; Li, Y., Interpersonal factors in the pharmacokinetics and pharmacodynamics of voriconazole: Are cyp2c19 genotypes enough for us to make a clinical decision? *Curr. Drug Metab.* **2018**, *19* (14), 1152-1158.

(9). Payne, K. D.; Hall, R. G., 2nd, Dosing of antibacterial agents in obese adults: Does one size fit all? *Expert Rev. Anti. Infect. Ther.* **2014**, *12* (7), 829-54.

(10). Arroyo-Currás, N.; Somerson, J.; Vieira, P. A.; Ploense, K. L.; Kippin, T. E.; Plaxco, K. W., Real-time measurement of small molecules directly in awake, ambulatory animals. *Proc. Natl. Acad. Sci. U. S. A.* **2017**, *114* (4), 645-650.

(11). Dauphin-Ducharme, P.; Yang, K.; Arroyo-Curras, N.; Ploense, K. L.; Zhang, Y.; Gerson, J.; Kurnik, M.; Kippin, T. E.; Stojanovic, M. N.; Plaxco, K. W., Electrochemical aptamer-based sensors for improved therapeutic drug monitoring and high-precision, feedback-controlled drug delivery. *ACS Sens.* **2019**, *4* (10), 2832-2837.

(12). Idili, A.; Gerson, J.; Kippin, T.; Plaxco, K. W., Seconds-resolved, in situ measurements of plasma phenylalanine disposition kinetics in living rats. *Anal. Chem.* **2021**, *93* (8), 4023-4032.

(13). Arakawa, T.; Tomoto, K.; Nitta, H.; Toma, K.; Takeuchi, S.; Sekita, T.; Minakuchi, S.; Mitsubayashi, K., A wearable cellulose acetate-coated mouthguard biosensor for in vivo salivary glucose measurement. *Anal. Chem.* **2020**, *92* (18), 12201-12207.

(14). Yang, Y.; Song, Y.; Bo, X.; Min, J.; Pak, O. S.; Zhu, L.; Wang, M.; Tu, J.; Kogan, A.; Zhang, H.; Hsiai, T. K.; Li, Z.; Gao, W., A laser-engraved wearable sensor for sensitive detection of uric acid and tyrosine in sweat. *Nat. Biotechnol.* **2020**, *38* (2), 217-224.

(15). Tran, B. Q.; Miller, P. R.; Taylor, R. M.; Boyd, G.; Mach, P. M.; Rosenzweig, C. N.; Baca, J. T.; Polsky, R.; Glaros, T., Proteomic characterization of dermal interstitial fluid

extracted using a novel microneedle-assisted technique. *J. Proteome Res.* **2018**, *17* (1), 479-485.

(16). Samant, P. P.; Niedzwiecki, M. M.; Raviele, N.; Tran, V.; Mena-Lapaix, J.; Walker, D. I.; Felner, E. I.; Jones, D. P.; Miller, G. W.; Prausnitz, M. R., Sampling interstitial fluid from human skin using a microneedle patch. *Sci. Transl. Med.* **2020**, *12* (571), eaaw0285.

(17). Teymourian, H.; Tehrani, F.; Mahato, K.; Wang, J., Lab under the skin: Microneedle based wearable devices. *Adv. Healthc. Mater.* **2021**, e2002255.

(18). Miller, P. R.; Taylor, R. M.; Tran, B. Q.; Boyd, G.; Glaros, T.; Chavez, V. H.; Krishnakumar, R.; Sinha, A.; Poorey, K.; Williams, K. P.; Branda, S. S.; Baca, J. T.; Polsky, R., Extraction and biomolecular analysis of dermal interstitial fluid collected with hollow microneedles. *Commun Biol* **2018**, *1* (1), 173.

(19). van der Maaden, K.; Jiskoot, W.; Bouwstra, J., Microneedle technologies for (trans)dermal drug and vaccine delivery. *J Control Release* **2012**, *161* (2), 645-55.

(20). Singh, P.; Carrier, A.; Chen, Y.; Lin, S.; Wang, J.; Cui, S.; Zhang, X., Polymeric microneedles for controlled transdermal drug delivery. *J Control Release* **2019**, *315*, 97-113.

(21). Goud, K. Y.; Moonla, C.; Mishra, R. K.; Yu, C.; Narayan, R.; Litvan, I.; Wang, J., Wearable electrochemical microneedle sensor for continuous monitoring of levodopa: Toward parkinson management. *ACS Sensors* **2019**, *4* (8), 2196-2204.

(22). Mohan, A. M. V.; Windmiller, J. R.; Mishra, R. K.; Wang, J., Continuous minimally-invasive alcohol monitoring using microneedle sensor arrays. *Biosens. Bioelectron.* **2017**, *91*, 574-579.

(23). Mishra, R. K.; Vinu Mohan, A. M.; Soto, F.; Chrostowski, R.; Wang, J., A microneedle biosensor for minimally-invasive transdermal detection of nerve agents. *The Analyst* **2017**, *142* (6), 918-924.

(24). Waltz, E., Sweet sensation. *Nat. Biotechnol.* **2019**, *37* (4), 340-344.

(25). Lee, I.; Probst, D.; Klonoff, D.; Sode, K., Continuous glucose monitoring systems - current status and future perspectives of the flagship technologies in biosensor research. *Biosens. Bioelectron.* **2021**, *181*, 113054.

(26). Teymourian, H.; Barfidokht, A.; Wang, J., Electrochemical glucose sensors in diabetes management: An updated review (2010-2020). *Chem. Soc. Rev.* **2020**, *49* (21), 7671-7709.

(27). Windmiller, J. R.; Zhou, N.; Chuang, M. C.; Valdes-Ramirez, G.; Santhosh, P.; Miller, P. R.; Narayan, R.; Wang, J., Microneedle array-based carbon paste amperometric sensors and biosensors. *Analyst* **2011**, *136* (9), 1846-51.

(28). Windmiller, J. R.; Valdes-Ramirez, G.; Zhou, N.; Zhou, M.; Miller, P. R.; Jin, C. M.; Brozik, S. M.; Polsky, R.; Katz, E.; Narayan, R.; Wang, J., Bicomponent microneedle array biosensor for minimally-invasive glutamate monitoring. *Electroanalysis* **2011**, *23* (10), 2302-2309.

(29). Teymourian, H.; Moonla, C.; Tehrani, F.; Vargas, E.; Aghavali, R.; Barfidokht, A.; Tangkuaram, T.; Mercier, P. P.; Dassau, E.; Wang, J., Microneedle-based detection of ketone bodies along with glucose and lactate: Toward real-time continuous interstitial fluid monitoring of diabetic ketosis and ketoacidosis. *Anal. Chem.* **2020**, *92* (2), 2291-2300.

(30). Goud, K. Y.; Moonla, C.; Mishra, R. K.; Yu, C.; Narayan, R.; Litvan, I.; Wang, J., Wearable electrochemical microneedle sensor for continuous monitoring of levodopa: Toward parkinson management. *ACS Sens.* **2019**, *4* (8), 2196-2204.

(31). Mohan, A. M. V.; Windmiller, J. R.; Mishra, R. K.; Wang, J., Continuous minimally-invasive alcohol monitoring using microneedle sensor arrays. *Biosens Bioelectron* **2017**, *91*, 574-579.

(32). Tuerk, C.; Gold, L., Systematic evolution of ligands by exponential enrichment: Rna ligands to bacteriophage t4 DNA polymerase. *Science* **1990**, *249* (4968), 505-10.

(33). Ellington, A. D.; Szostak, J. W., In vitro selection of rna molecules that bind specific ligands. *Nature* **1990**, *346* (6287), 818-22.

(34). Wu, Y.; Belmonte, I.; Sykes, K. S.; Xiao, Y.; White, R. J., Perspective on the future role of aptamers in analytical chemistry. *Anal. Chem.* **2019**, *91* (24), 15335-15344.

(35). Yi, K.; Wang, Y.; Shi, K.; Chi, J.; Lv, J.; Zhao, Y., Aptamer-decorated porous microneedles arrays for extraction and detection of skin interstitial fluid biomarkers. *Biosens. Bioelectron.* **2021**.

(36). Shaver, A.; Curtis, S. D.; Arroyo-Currás, N., Alkanethiol monolayer end groups affect the long-term operational stability and signaling of electrochemical, aptamer-based sensors in

biological fluids. *ACS Appl. Mater. Interfaces* **2020**, *12* (9), 11214-11223.

(37). Idili, A.; Arroyo-Curras, N.; Ploense, K. L.; Csordas, A. T.; Kuwahara, M.; Kippin, T. E.; Plaxco, K. W., Seconds-resolved pharmacokinetic measurements of the chemotherapeutic irinotecan in situ in the living body. *Chem. Sci.* **2019**, *10* (35), 8164-8170.

(38). Arroyo-Curras, N.; Ortega, G.; Copp, D. A.; Ploense, K. L.; Plaxco, Z. A.; Kippin, T. E.; Hespanha, J. P.; Plaxco, K. W., High-precision control of plasma drug levels using feedback-controlled dosing. *ACS Pharmacol.Transl. Sci.* **2018**, *1* (2), 110-118.

(39). Arroyo-Curras, N.; Dauphin-Ducharme, P.; Ortega, G.; Ploense, K. L.; Kippin, T. E.; Plaxco, K. W., Subsecond-resolved molecular measurements in the living body using chronoamperometrically interrogated aptamer-based sensors. *ACS Sens.* **2018**, *3* (2), 360-366.

(40). Xiao, Y.; Lai, R. Y.; Plaxco, K. W., Preparation of electrode-immobilized, redox-modified oligonucleotides for electrochemical DNA and aptamer-based sensing. *Nat Protoc* **2007**, *2* (11), 2875-80.

(41). Arroyo-Currás, N.; Ortega, G.; Copp, D. A.; Ploense, K. L.; Plaxco, Z. A.; Kippin, T. E.; Hespanha, J. P.; Plaxco, K. W., High-precision control of plasma drug levels using feedback-controlled dosing. *ACS Pharmacology & Translational Science* **2018**, *1* (2), 110-118.

(42). Pellitero, M. A.; Curtis, S. D.; Arroyo-Currás, N., Interrogation of electrochemical aptamer-based sensors via peak-to-peak separation in cyclic voltammetry improves the temporal stability and batch-to-batch variability in biological fluids. *ACS Sensors* **2021**, *6* (3), 1199-1207.

(43). Li, S.; Wang, Y.; Zhang, Z.; Wang, Y.; Li, H.; Xia, F., Exploring end-group effect of alkanethiol self-assembled monolayers on electrochemical aptamer-based sensors in biological fluids. *Anal Chem* **2021**, *93* (14), 5849-5855.

(44). Curtis, S. D.; Ploense, K. L.; Kurnik, M.; Ortega, G.; Parolo, C.; Kippin, T. E.; Plaxco, K. W.; Arroyo-Currás, N., Open source software for the real-time control, processing, and visualization of high-volume electrochemical data. *Analytical Chemistry* **2019**, *91* (19), 12321-12328.

(45). Groenewald, T., The dissolution of gold in acidic solutions of thiourea. *Hydrometallurgy* **1976**, *1* (3), 277-290.

(26). Carvalhal, R. F.; Sanches Freire, R.; Kubota, L. T., Polycrystalline gold electrodes: A comparative study of pretreatment procedures used for cleaning and thiol self-assembly monolayer formation. *Electroanalysis* **2005**, *17* (14), 1251-1259.